Decoding a master regulator of calcium homeostasis

by

Lingjie Sang

A dissertation submitted to Johns Hopkins University in conformity with
the requirements for the degree of Doctor of Philosophy

Baltimore, Maryland
May, 2016

Abstract

The interaction between the IQ and ICDI domains in L-type Ca^{2+} channels is both functionally important and mechanistically intriguing. By preventing calmodulin from binding to the IQ domain, the ICDI domain diminishes channel open probability and Ca^{2+}/CaM dependent inactivation (CDI). In this work, we performed alanine scanning of the entire IQ and ICDI domains. Hotspot mutations which reduce IQ/ICDI binding affinity also commensurately diminish ICDI function (i.e., permit restoration of CDI). The ensemble of effects can be well fit with a Langmuir equation. The collection of hotspots also allowed us to identify the segment downstream of the IQ contributing to the interaction. Further, we discovered a novel PKA phosphorylation site on the ICDI domain of Cav1.4, so PKA activation diminishes the IQ and ICDI interaction and thus increases channel open probability and CDI. As Cav1.4 is the major Ca^{2+} channels in the retina, this modulation might contribute to the circadian rhythms of visual sensitivity.

On the other hand, FRET two-hybrid is an important tool for this work, which allows us to measure the binding affinities of protein interactions. Here we also extended the FRET assays to novel platforms, including flow cytometer and plate reader, in order to study protein interactions and identify small molecules interfering protein interactions in high throughput. We also developed a lysate-based FRET binding assay to calibrate the optical system and accurately measure binding affinities. Further, by applying weak helpers, we now can measure the binding affinities of weak protein interactions.

Advisor: David T. Yue, M.D., Ph.D.

Readers: Gordon F. Tomaselli, M.D., Frank Bosmans, Ph.D., Ivy E. Dick, Ph.D.

Acknowledgement

It's a long journey from a new college graduate to the end of my Ph.D. study, and I owe a lot to many that helped me along the way.

I am very grateful to my advisor Professor David Yue. Dr. Yue was a very dedicated mentor and enthusiastic teacher. He spent lots of time to provide hands-on coaching on anything I needed, no matter if it was a piece of broken equipment, or a mispronounced word in a lab presentation. He gave me greatest freedom to explore any experiment that could help with my project, even nobody in the lab had done that before; while he also deeply understood the risk of failure. There were many difficult moments when things did not work and I felt defeated. He showed deep a sympathy and tried to encourage me and carried me along. He was very excited when I eventually got good data. I remembered that day, he sat down with me and a few others, and started to talk about his own student life. He was very happy. I know it is not just for the data, but also for me. That was December 12, 2014. It is still hard to believe he already left us for more than a year now. There are many things he rooted into me, the craftsmanship, the perseverance, always striving for perfection, thinking logically and expressing linearly, which I will carry with me for the future journey of my life.

I also appreciate Dr. Gordon Tomaselli very much for all his selfless help in the last one and half year. Despite his tight schedule, he came to our journal clubs every week, stayed with us for every single important moment to every member in the lab, and provided help with everything we needed. He took the responsibility of an advisor to us without any credits. He also agreed to be the chair of my committee, provided keen advice to my research and helped to proofread the manuscript for submission, including the methods section. He is one of the most generous people in the world.

I also very appreciate Dr. Leslie Tung and Dr. Frank Bosmans for serving on my committee despite their busy schedule, providing very valuable feedback to my research and great support to my career. Their encouragement and support helped me through the hardest time. Also many thanks to Dr. King Way Yau, for coaching me with a presentation at the Biophysics meeting, and for great advice to my research and career.

I want to thank all members in Calcium Signals Lab for their friendship, support and all the moments shared together. Especially, I want to thank Ivy for being a great mentor, friend and big sister to me, for helping me with the writings, for spending lots of time to work on our paper, for trying all possible experiments for a rebuttal, for fighting hard together and encouraging me along the way. Also I want to thank Manu for many great suggestions and help with my work, for deriving the equations with me to simplify my thoughts and helping me with making figures in the early days, and for repairing equipment and that he let us use. Thank you Hojjat for coaching me with the core lab techniques and spending time to help me with experiments. Thank you Shin Rong for being a great partner, teaching me cool techniques, helping me with experiments and inspiring me. Thank you Wanjun for very dedicated lab support. I also want to give special thanks to St. Nancy, for her care and sacrifice to the lab and her strength to carry us through the hardest moment. You are always part of our lab as a big family and a role model to me.

There are also many other researchers that helped along the road. I would like to thank Dr. Rachel Karchin for supporting me with my first rotation, thank Drs. Min Li, Meng Wu and Owen McManus with the initial phase of the drug screening project and Carl Apcar at Perkin Elmer for coming to Hopkins and the help with optimizing the plate reader. I also want to thank Dr. Bob Cole and Bob O'Meally for help with mass spectroscopy experiments, thank Bradley Hardern and Scott Nichols for teaching me protein purification, thank Dr. Wendy Yue for teaching me retina isolation and thank Debbie DiSilvestre for helping me with western blots.

Finally, I would like to thank my family for their long lasting support and love. To my husband Rui, I felt lucky to meet you at Hopkins. Thank you for always being together with me, for encouraging me when I felt defeated, and for supporting me to pursue my career, even sometimes I am uncertain about where to go. To my parents, who are my best teachers and friends and give me unconditional love and everything, without whom I would never have enjoyed so many opportunities and happiness.

Table of Contents

List of Figures

Introduction

Voltage-gated Ca^{2+} channels (Cav channels) constitute prominent Ca^{2+} entry portals that affect a multitude of cell functions including muscle/neuron excitability, gene transcription, and downstream signaling pathways[1-3]. The Cav channel family is further divided into three major groups, Cav1, Cav2, and Cav3, based on sequence similarity (see the figure below). Cav1, the so called L-type calcium channel, has four members. Cav1.1 mainly exists in skeletal muscle, and primarily acts as a voltage senor rather than an ion pore. Because Cav1.1 channels conduct very small currents and are hard to study in heterologous systems, my thesis will focus on the other three L-type channels. Cav1.2 and 1.3 are widely expressed, and coexist in many excitable cells. Cav1.2 is best known for initiating excitation-contraction (EC) coupling in ventricular myocytes, while Cav1.3 is more important for neuron function and sensory systems such as inner ear cells. Finally, Cav1.4 mainly exists in retina cells.

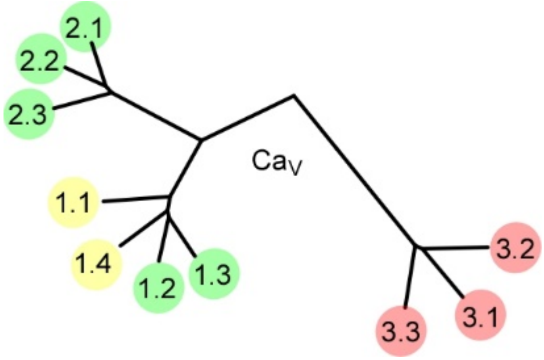

Family tree of Ca$_V$ channels, adopted and modified from Ben-Johny *et al*[4]

Given the importance of these channels, they undergo several forms of regulation in order to tune the entry of calcium within each cell type. Calmodulin (CaM), a master regulator of ion channels, plays a central role in regulating Cav channels. In a prototypical Cav channel, a single CaM is constitutively associated with the IQ domain of the channel carboxy terminus[5], and enhances channel opening[6]. Moreover, Ca^{2+} binding to CaM triggers conformational changes that can decrease channel opening[7], a process known as Ca^{2+}/CaM dependent inactivation (CDI). However, long splice variants of Cav1.3 and Cav1.4 lack CDI due to a CDI inhibiting module (ICDI) that competes with CaM for binding to the IQ domain[8]. This lack of CDI is critical to maintaining light sensitivity in photoreceptors[9,10] (Cav1.4) and sound sensitivity in inner hair cells[11,12] (Cav1.3), both in response to prolonged stimuli. Indeed, mutations in the ICDI domain of these channels increase CDI, and lead to congenital stationary night blindness in patients[13]. Beyond pathophysiology, the fact that ICDI can retune CDI-[apoCaM] relations points out the possibility that natural variations of Ca^{2+} free CaM (apoCaM) concentrations can modify CDI and Ca^{2+} entry, ultimately customizing cell function and Ca^{2+} homeostasis. In this sense, ICDI may be considered as a *master regulator* of Ca^{2+} homeostasis, and as such, I will focus my thesis work on this very interesting module.

This thesis is composed of three parts. In the first part, extensive mutagenesis studies were performed to decode the interaction hotspots on the interface between IQ and ICDI. A unified mechanism was established for Cav1 channels, where by changing the ICDI binding affinity to the IQ domain, we can modulate the strength of this domain and regulate channel calmodulation accordingly. Interestingly, a peptide containing the

ICDI domain from Cav1.2 can regulate a special splice variant of Cav1.3, which might be a good example of trans-channel feedback regulation.

As FRET two-hybrid is an established tool for probing protein interactions, the second part of this thesis is dedicated to designing novel platforms to improve and expand the capabilities of this assay. A lysate-based FRET assay allows accurate measurement of absolute binding affinities in a quasi-native context without purifying the proteins. Divalent binding with weak helpers can be used to measure binding affinities of weak protein interactions. Further, platforms such as plate readers and flow cytometers were deployed for FRET binding assays, allowing for the study of protein interactions in a higher throughput fashion. These assays were applied to study the IQ/ICDI interaction and potential modulators of this interaction.

The third part of this thesis aims to identify specific regulators of the interaction between IQ and ICDI, which led to the discovery of a novel PKA phosphorylation site on the ICDI domain of Cav1.4. Phosphorylation of this site largely reduces the binding affinity between IQ and ICDI, and thus increases CDI and channel open probability. Overall, this thesis work provides significant insight into the molecular underpinnings of L-type channel regulation.

Chapter 1

Resolving the grip of the distal carboxy tail on the proximal calmodulatory region of Ca_V channels

Introduction

Voltage-gated Ca^{2+} channels (Cav channels) constitute prominent Ca^{2+} entry portals that affect a multitude of cell functions including muscle/neuron excitability, gene transcription, and downstream signaling pathways[1-3]. As such, these channels are subject to rich and powerful modes of feedback regulation. For example, the ubiquitous Ca^{2+}-sensing molecule calmodulin (CaM) in the Ca^{2+}-free form (apoCaM) is prebound to these channels at a carboxy-terminal IQ domain (**Figure 1A**)[7,8,14]. Upon elevation of intracellular Ca^{2+} concentration, this 'resident' CaM binds Ca^{2+} ions to drive conformational changes that ultimately inhibit channel opening. Displayed in **Figure 1A**, are recombinant Cav1.3 currents in HEK293 cells, evoked by a step depolarization to +10 mV. With Ca^{2+} as the charge carrier, current decays quickly after activation, furnishing evidence of strong Ca^{2+}-dependent inactivation (CDI). With Ba^{2+} as the charge carrier, however, there is little decline of current during the voltage pulse, as Ba^{2+} (which binds poorly to CaM) cannot initiate CDI. This CDI process is a crucial negative feedback mechanism that orchestrates Ca^{2+} homeostasis, protects against Ca^{2+} overload, and critically controls muscle/neuron excitabilit[1,15-17]. Thus far, what has been said about CDI pertains to nearly all Cav1-2 channels. This basic scheme of autoregulation is conserved across all high voltage-activated Ca^{2+} channels. Curiously, certain L-type Ca^{2+} channels (Cav1.3 and Cav1.4) also feature an alternatively spliced distal carboxy tail (DCT) that abolishes CDI. Mechanistically, a CDI-inhibiting module (ICDI, **Figure 1B**) on the DCT is thought to competitively inhibit apoCaM binding to the channel IQ domain and thereby preclude any Ca^{2+}/CaM dependent regulation[11,12]. Indeed, with Ca^{2+} as the charge carrier, these channels show only a small decrease in current, which is indicative of weak CDI. Importantly, recent studies also show that loss of apoCaM preassociation, as induced by the ICDI module, also sharply reduces the channel open probability[6], adding to the richness of modulatory functions by the ICDI module.

Despite these critical advances that outline the overall function of the ICDI module, the key structural elements that mediate the IQ/ICDI interaction remain largely undefined, with the exception of a single residue that mysteriously blunts ICDI effects[8]. Of note, the distal carboxy-terminus represents a large segment of the channel cytosolic domain thought to serve as a hub for numerous cellular signaling molecules. As such, in depth residue-level analysis will not only reveal potent interfaces to alter channel function, but may also facilitate the search for novel regulators of the family of IQ motif proteins.

To characterize the landscape of the IQ/ICDI interaction of Cav1.3/1.4 channels, we undertook systematic alanine scanning mutagenesis of both IQ and ICDI domains. Through application of live-cell FRET two-hybrid binding assays, we identified several novel hotspots on both IQ and ICDI segments that mediate a high affinity interaction. Remarkably, functional analyses of these mutant channels demonstrated a weakened ICDI effect, resulting in restoration of CDI. A systematic analysis of such mutations revealed a strong inverse correlation (**Figure 1C**) between the strength of CDI and the binding affinity of the ICDI domain for the IQ segment as expected for a competitive inhibitor. Based on such extensive analysis, we built an *ab initio* computational structure model of IQ/ICDI interaction using Robetta[18] and Patchdock[19] to illustrate the competitive nature of ICDI and CaM interaction with the IQ domain. Finally, extending our analysis to Cav1.2 channels, we found that while the $ICDI_{1.2}$ module binds poorly to the IQ domain of Cav1.2, it is, however, capable of regulating specific splice variants of Cav1.3 channels, revealing a novel trans-channel feedback regulation.

Methods

Molecular biology. The Cav1.3 channel (in pcDNA6) was derived from the rat brain variant (AF307009.1)[20], and incorporated to the mammalian expression plasmid pCDNA6 (Invitrogen), which features a unique *Bgl*II restriction site at a locus corresponding to ~450 amino acids upstream of the IQ domain, and a unique *Xba*I site after the stop codon. The Cav1.2 (in pGW) is identical to rabbit NM001136522[21], and Cav1.4 (in pCDNA3) is the human clone corresponding to NM00718[6]. $Cav1.3_{S/1.4DCT}$ was made by fusing with the DCT of Cav1.4 to the Cav1.3 channel (truncated after the IQ domain), as previously described[8]. $Cav1.3_{43S}$ was made by PCR amplification of the channel segment between the *Bgl*II site and IQ domain with the appendage of amino acids unique to this splice variant (**Figure 6B**). The PCR product was then inserted into the channel via the *Bgl*II/*Xba*I sites.

FRET constructs were fluorescent-tagged (either Venus or Cerulean) using similar strategies as previously described[14]. Briefly, Venus and Cerulean fluorophores (a kind gift from Dr. Steven Vogel at NIH) were subcloned into the pcDNA3 vector via unique *Kpn*I and *Not*I sites. The PCR-amplified channel peptides, as described in Liu *et. al.*[8], were then cloned in via unique *Not*I and *Xba*I sites.

Mutations were introduced into the channel or FRET construct via PCR amplification or overlap extension PCR.

Transfection of HEK293 cells. For electrophysiology experiments, HEK293 cells were cultured on 10-cm plates, and channels were transiently transfected by a calcium phosphate protocol[22]. We applied 8 μg of plasmid DNA encoding the desired α_1 subunit, as well as 8 μg of β and 8 μg of rat $\alpha_2\delta$ (NM012919.2)[23] subunits along with 3 μg of SV40 T antigen.

For microscope-based FRET assays, HEK293 cells cultured on 3.5-cm culture dishes with integral No. 0 glass coverslip bottoms (In Vitro Scientific) were transiently transfected using polyethylenimine (PEI) reagent (Polysciences).

Whole-cell electrophysiology recording. Whole-cell recordings were obtained using an Axopatch 200A amplifier (Axon Instruments). Electrodes were pulled from borosilicate glass capillaries (Word Precision Instruments), with 1-3 MΩ resistances, which were in turn compensated for series resistance by >60%. Currents were low-pass filtered at 2 kHz before digital acquisition at five times the frequency. A P/8 leak-subtraction protocol was used. The internal solution contained (in mM): $CsMeSO_3$, 114; CsCl, 5; MgATP, 4; HEPES (pH 7.4), 10; and BAPTA (1,2-bis(*o*-aminophenoxy)ethane-*N*,*N*,*N'*,*N'*-tetraacetic acid), 10; at 295 mOsm adjusted with $CsMeSO_3$. The bath solution was (in mM): TEA-$MeSO_3$, 102; HEPES (pH 7.4), 10; $CaCl_2$ or $BaCl_2$, 40; at 305 mOsm adjusted with TEA-$MeSO_3$.

Microscope-based FRET optical imaging. FRET two-hybrid experiments were performed on an inverted microscope as described[7,14]. The bath solution was a Tyrode's solution composed of (in mM): NaCl, 138; KCl, 4; $MgCl_2$, 1; HEPES (pH 7.4), 10; $CaCl_2$, 2; at 305mOsm adjusted with glucose. Background fluorescent signals were measured from cells without expression of the fluorophores, and subtracted from cells expressing the fluorophores. Concentration-dependent spurious FRET was subtracted from the raw data prior to binding-curve analysis[7,14]. Cerulean[24] and Venus[25] were used as the donor and acceptor fluorescent proteins instead of ECFP and EYFP, as their optical properties are better for this application. Acceptor-centric measurements of FRET were obtained with the 3^3-FRET algorithm[7,14], which expresses the effective FRET efficiency (E_{EFF}) and FRET ratio (FR) as:

$$E_{\text{EFF}} = E \times A_{\text{b}} = (FR - 1)[\varepsilon_{\text{ven}}(440nm)/\varepsilon_{\text{cer}}(440nm)]$$

where $E = k_{\text{T}}/(k_{\text{T}} + k_{\text{D}})$ is the FRET efficiency of a donor-acceptor pair, A_{b} is the fraction of acceptor molecules bound by a donor. $\varepsilon_{\text{ven}}(440nm)/\varepsilon_{\text{cer}}\,(440nm)$ is the approximate molar extinction coefficients of Cerulean and Venus, which was measured as 0.08 on our setup.

Molecular modelling. *Ab initio* structural prediction was performed using the Robetta online server[26] (http://robetta.bakerlab.org), and web-based molecular docking programs Patchdock[19] (http://bioinfo3d.cs.tau.ac.il/PatchDock/) was used to obtain models for molecular docking.

Results

Alanine Scanning Mutagenesis reveals high affinity anchors for ICDI segment

To identify key residues that support a high-affinity IQ/ICDI interaction, we undertook systematic alanine substitution of the IQ domain and evaluated both the relative binding affinity and the strength of ICDI mediated inhibition of CaM regulation. Importantly, the ICDI domains of both Cav1.3 and Cav1.4 are highly homologous, and have been shown to interact with IQ domains in like manner evoking similar functional effects[8]. Even so, the $ICDI_{1.4}$ has a very high binding affinity for IQ domains of both Cav1.3 and Cav1.4, with FRET binding assays yielding more robust measurements with better signal to noise ratio. Moreover, robust expression of the holo-Cav1.4 channel in recombinant systems is notoriously challenging. Accordingly, for simplicity, our structure-function analysis interrogates the interaction of $ICDI_{1.4}$ with the Cav1.3 IQ domain, and further characterizes the functional consequences of this interaction using a chimeric Cav1.3 channel containing the distal carboxy-tail of Cav1.4.

FRET binding pairs were constructed by tagging cerulean fluorescent protein to the ICDI domain from Cav1.4 and venus fluorescent protein to $PreIQ_3$-IQ-$A_{1.3}$, a peptide that includes ~ 50 residues both upstream ($PreIQ_3$) and downstream (A-region) of Cav1.3 IQ domain (**Figure 1D**). Both $PreIQ_3$ and A regions were included initially for the purpose of facilitating peptide folding and expression. While strong binding was detected between the Venus-$PreIQ_3$-IQ-$A_{1.3}$ and Cerulean-$ICDI_{1.4}$ ((**Figure 1D**), middle, green circles and green curve), there is little FRET interaction between a peptide containing the venus-tagged A region alone and Cerulean-$ICDI_{1.4}$ (**Figure 1D**, open black circles).

We began with systematic alanine scanning mutagenesis of the IQ domain of chimeric $\mathrm{Ca_V1.3_{S/1.4DCT}}$, where each residue in this region was mutated into an alanine or, at loci where the wild-type channel featured an alanine residue, a threonine. The FRET 2-hybrid binding assay revealed that three residues, Y[-5]A, F[-2]A and F[+4]A, most severely perturbed the IQ/ICDI interaction (**Figure 2A**). Functional analysis of the F[-2]A mutation revealed a partial rescue of CDI, suggesting weakened ICDI binding (**Figure 2D**). That said, other IQ domain substitutions Y[-5]A and F[+4]A resulted in minimal CDI rescue (**Figure 2B**). Importantly, these residues also serve as key anchors for apoCaM binding to the Cav1.3 IQ domain, resulting in weak baseline CDI even in the absence of the ICDI domain (**Figure 2C**)[27]. To account for this ambiguity, we consider a quantitative competitive inhibition model of CDI for $\mathrm{Ca_V1.3_{S/1.4DCT}}$ channels incorporating both the IQ domain's intrinsic affinity for apoCaM ($K_{\mathrm{d\text{-}Ch}}$) and that for the ICDI segment ($K_{\mathrm{d\text{-}ICDI}}$), the competitive inhibitor. Accordingly, CDI correlates inversely with binding affinity between IQ and ICDI ($1 / K_{\mathrm{d\text{-}ICDI}}$), according to the relationship expressed in Equation 1.

$$\frac{CDI}{CDI_{\max}} = \frac{[\mathrm{apoCaM}]}{[\mathrm{apoCaM}] + K_{\mathrm{d-Ch}}\left(1 + \frac{[\mathrm{ICDI}]}{K_{\mathrm{d-ICDI}}}\right)} \qquad (1)$$

Here, CDI is the strength of CDI under endogenous levels of CaM; $CDI_{\max}$ is the CDI in saturating concentrations of CaM; $K_{\mathrm{d\text{-}Ch}}$ is dissociation constant for apoCaM binding to holochannel in absence of ICDI; [apoCaM] is the free apoCaM concentration in cell; and [ICDI] is the effective local concentration of ICDI to IQ. Details about the derivation of this equation can be found in Liu *et al* [8]. Equation 1 predicts an inverse correlation between $1 / K_{d\text{-}ICDI}$ and CDI. For channels contain intact IQ and ICDI domains, there is strong binding between the two (i.e. large $1 / K_{d\text{-}ICDI}$) and minimal CDI, as shown by the green dot on **Figure 1C** and **Figure 2E**. By contrast, for channels without the ICDI domain, $1 / K_{d\text{-}ICDI} = 0$ by definition, and thus CDI approaches CDI_{max}, as shown by the light gray dot on **Figure 1C** and **Figure 2E**. As the IQ domain is critical for binding to both apoCaM and the ICDI segment, mutations in the IQ domain may then impact either $K_{d\text{-}Ch}$ or $K_{d\text{-}ICDI}$. By contrast, mutations in the ICDI segment would simply impact $K_{d\text{-}ICDI}$. **Figure 2E** plots the ratio CDI / CDI_{max} as a function of $1 / K_{d\text{-}ICDI}$. For mutations like Y[-5]A or F[4]A, where $K_{d\text{-}Ch}$ is altered, we compensate by multiplying $K_{d\text{-}ICDI}$ measured for these mutations (**Figure 1A**) by the ratio of $K_{d\text{-}Ch}$ of mutated channels to $K_{d\text{-}Ch}$ of the wild-type channel. This compensation works as long as the local concentration of ICDI is much greater than $K_{d\text{-}ICDI}$ ($[ICDI] >> K_{d\text{-}ICDI}$). Values for $K_{d\text{-}Ch}$ were obtained from a previous study[27] (**Figure 2C**). Once compensated, all relevant mutations follow the relation shown in Equation 1 well (**Figure 2E**). The parameters used in fitting Equation 1 are: $[apoCaM] = 10\mu M$, $K_{d\text{-}Ch} = 0.05\ \mu M$, $[ICDI] = 90\ \mu M$.

Alanine scanning of ICDI region reveals complementary hotspots

As binding can be perturbed by mutations in either binding partner, we continued to undertake alanine mutagenesis of the ICDI domain. Every three contiguous residues in the ICDI domain were substituted with alanines. The FRET two-hybrid binding assay revealed multiple novel hotspots on the ICDI segment with a wide range of affinities for the IQ domain. Of note, the effects of the hotspots on the ICDI segment were significantly larger than those observed within the IQ domain (notice that the scale of y-axis in **Figure 3A** is much bigger than **Figure 2A**). Functional analysis of these mutants revealed restoration of CDI corresponding to the weakened IQ/ICDI interaction (**Figure 3B**). For example, IAD[1914]AAA moderately reduced IQ/ICDI binding and thus partially restored CDI (**Figure 3C**); SLV[1886]AAA disrupted IQ/ICDI binding to a large extent, and correspondingly restored functional CDI (**Figure 3D**) to the level of Cav1.3$_S$ channels which lack ICDI (**Figure 1C**). All the newly identified hotspots fit well with Equation 1, using the same set of parameters as the IQ mutations (**Figure 3E**). The small amount of variability observed may be attributed to cell-to-cell variation in endogenous apoCaM concentrations. Overall, the strong correlation of the IQ and ICDI data furnishes strong evidence for a competitive mechanism of ICDI action.

The role of the A region in the IQ/ICDI interaction

Curiously, even though our analysis identified several IQ domain hotspots, the impact of such mutations were far milder than that of ICDI hotspots (**Figure 2** versus **Figure 3**). This suggested that regions upstream or downstream of IQ may also contribute to ICDI binding. To test this hypothesis, we constructed various truncations of Venus-PreIQ$_3$-IQ-A$_{1.3}$, and paired them with Cerulean-ICDI$_{1.4}$ in the FRET two-hybrid binding assays (**Figure 4A**). Truncations of the PreIQ$_3$ region did not significantly alter ICDI binding (**Figure 4B**). However, truncation of the A region resulted in a sharply diminished ICDI interaction (**Figure 4B**), suggesting that this segment is critical despite the fact that the A-region alone did no support detectable ICDI binding (**Figure 2A**, open black circle). Serial truncations within the A region show that truncating up to the 35th residue within the A region does not affect binding (IQ-AΔ34$_{1.3}$, **Figure 4B**), but additional truncations into the A region results in sharply reduced binding (**Figure 4B, C**). Thus, the 34 residues immediately downstream of the IQ domain critically augment ICDI binding. Accordingly, we conducted systematic alanine scanning mutagenesis of this critical segment of the A region, and found several novel hotspots for a high affinity IQ/ICDI interaction (**Figure 4D**).

Ab initio structure modeling by Rosetta.

With functionally relevant hotspots for the IQ/ICDI interaction firmly identified, we constructed an *ab initio* molecular model to further scrutinize its role in competing with CaM. While the atomic structure of the IQ domain of Cav channels is known (**Figure 5A**), no homologous structure of the ICDI domain can currently be found in the Protein Data Bank (PDB). Thus, we performed *ab initio* protein structure prediction on the ICDI segment using the Rosetta[18]. Next, we docked the structural model of the ICDI domain onto the IQ domain using Patchdock[19], an online server for fast protein-protein docking based on shape complementarity. Among the ten highest-scoring output models from Patchdock, two corresponded well with our alanine scanning data as shown in **Figure 5C** and **D**. Notably, residue F[4] on the IQ domain (**Figure 5D**) forms a likely hydrophobic anchor with close proximity to residues V[1888] (in SLV) and I[1893] (in LIS) and V[1907] (in V) and M[1925] (in DEM), all hotspots identified in our alanine scanning mutagenesis experiments (**Figure 3A, B**). Importantly, F[4] is also a key the apoCaM contact on IQ region (**Figure 3C** and **Figure 5A**).

Comparing models of apoCaM/IQ and IQ/ICDI interactions, we can see that apoCaM wraps around the IQ domain to form a tight interaction with residues (including

F[4]) on one face of the IQ helix (**Figure 5B**), while ICDI wraps around the IQ domain from a slightly different angle compared to apoCaM. However, the bulky ICDI residing on the IQ can sterically repel apoCaM binding (**Figure 5C**), resulting in competitive inhibition at the molecular level.

Exploring similar interactions within Ca$_V$1.2

Similar to Cav1.3 and Cav1.4 channels, Cav1.2 channels also feature a homologous ICDI segment, argued to function as a channel inhibitor[28,29] or as a transcriptional factor[30,31]. That said whether such putative roles relate to interaction of ICDI$_{1.2}$ with the channel IQ domain is largely unknown. As such, we measured the binding affinity between Venus-PreIQ$_3$-IQ-A$_{1.2}$ and Cerulean-ICDI$_{1.2}$ by FRET two-hybrid assays and found that this interaction is ~10-fold weaker (**Figure 7A**) than the prototypic Venus-PreIQ$_3$-IQ-A$_{1.3}$ and Cerulean-ICDI$_{1.4}$ interaction (**Figure 1D**). Importantly, we recently found a phosphorylation site on ICDI$_{1.4}$, which reduces its binding affinity to the IQ region of Cav1.3/1.4 by about 10-fold and largely increases the CDI in chimeric Cav1.3$_{S/1.4DCT}$ and Cav1.4 channels (orange point in **Figure** 3C, see more in Chapter 3). This result indicates that the strength of ICDI$_{1.2}$ in regulating calmodulation of the channel is substantially lower than that of the Cav1.3 and 1.4 counterparts. Indeed, no obvious difference in CDI was observed between Cav1.2 with[8] or without the DCT[32] by whole-cell electrophysiology. As such, we conclude that the interaction between the IQ and ICDI regions of Cav1.2 channels has a relatively low affinity and may only cause mild changes in CDI and channel open probability.

Interestingly, we found that $\mathrm{ICDI}_{1.2}$ has a higher affinity for IQ-$\mathrm{A}_{1.3}$ than IQ-$\mathrm{A}_{1.2}$ (**Figure 7A**). Several recent studies have shown that the $\mathrm{ICDI}_{1.2}$ segment exist in neurons and cardiomyocytes as a peptide due to proteolysis[28,33], or as a result of alternative transcriptional initiation sites[30]. We thus wondered if these peptides could interact with and regulate CaV1.3 channels. The canonical CaV1.3 channels exist in two forms, a long splice variant with the ICDI domain intact and thus exhibiting diminutive CDI and P_O, and a short splice variant truncated shortly after the IQ domain and thus possessing large CDI and P_O[6,8]. The long splice variant contains its own ICDI segment and is therefore unlikely to be further affected by the $\mathrm{ICDI}_{1.2}$ peptide. The canonical short splice variant ($\mathrm{Ca_V1.3_{42}}$) contains only 10 residues in the A region, and is therefore not affected by the potent $\mathrm{ICDI}_{1.4}$ peptides (data not shown). A recently discovered splice variant $\mathrm{Ca_V1.3_{43S}}$, on the other hand, has a premature stop codon after the first one third of the A region[34]. It thus contains the minimal IQ-A domain necessary for ICDI binding. While these channels exhibit strong CDI when expressed alone, they display minimal CDI when coexpressed with the potent $\mathrm{ICDI}_{1.4}$ peptides (**Figure 7B, C**). Interestingly, they also exhibit largely diminished CDI when coexpressed with the $\mathrm{ICDI}_{1.2}$ peptide (**Figure 7B, C**). The CDI and FRET binding data measured for $\mathrm{Ca_V1.3_{43S}}$ coexpressed with $\mathrm{ICDI}_{1.2}$ reside on a Langmuir curve (**Figure 7D**) which is slightly right-shifted from the previous one described in **Figure 2** and **Figure 3**, reflecting the reduced effective local concentration of ICDI near the IQ domain, as the ICDI segment is no longer fused to the channel in this experiment[5]. In all, our studies show that in addition to its previously described regulatory functions[29,30,30], the ICDI$_{1.2}$ peptide may also regulate the closely related Cav1.3 channels, establishing a novel mode of trans-channel regulation.

Discussion

Calmodulation of Cav channels is a central prototype for high-order Ca^{2+} decoding. Beyond its role as a master regulator of ion channels, CaM is a key signaling molecule capable of binding a wide range of molecules. In addition to Cav channels, a number of proteins, such as neuromodulin and neurogranin, contain IQ-motifs that interact with CaM. The family of IQ-motif containing proteins have little sequence similarity outside of the IQ-domain, allowing for diverse functionality. Mechanistically, ICDI plays a unique role as a regulator of the Cav IQ domain. Are there other proteins that utilize a similar strategy to regulate CaM signaling? Understanding the structural details of IQ/ICDI interaction and decoding key motifs within the ICDI would facilitate the search for regulators of varied IQ-motif proteins.

More broadly, the distal carboxy tail (DCT) could be a key module for understanding the functional diversity of Cav channels, especially those with similar biophysical and pharmacological properties, as determined by highly conserved pore and proximal carboxy-tail regions. Compared to these regions, the DCT (which resides beyond these aforementioned regions of conservation) promises greater channel subtype selectivity due to greater sequence variability. Higher-order regulation of the DCT, such as phosphorylation (Chapter 3) and interaction with other proteins (**Figure 6**), also exists in a customized format according to the channel subtype in question, adding to the diversity of channel functions. Thus, understanding the functional diversity of the DCT provides novel opportunities for identifying small-molecule and synthetic peptide regulators targeted to specific channel subtypes.

While X-ray crystallography offers high resolution atomic structures, the size of the channel makes protein crystallography prohibitive. Moreover, crystallization of even short channel segments have been challenging and the relevance of such structures to holochannel function is often controversial[35,36]. Here, we adopt an alternative approach, applying systematic alanine scanning of the IQ and ICDI domains to identify hotspots of the IQ and ICDI interaction. Moreover, we have utilized the resulting information to aid in building a structural model through *ab initio* computational protein structure prediction and docking. The detailed map of the IQ/ICDI interaction also helps us to understand the role played by another important region, the A region. Unlike the IQ domain, the A region is not directly involved in calmodulation, but it is likely that the A region forms an interface with ICDI and contributes to its binding to the IQ domain, and regulation of calmodulation of these channels.

The quantitative FRET two-hybrid live cell binding and patch clamping assays allow us to fit data of all mutations studied to a Langmuir equation, furnishing strong evidence of a competitive inhibitor model[8]. While we postulate a unified mechanism of ICDI modulation across Cav1 channel families, the DCT of Cav2 channels are much less homologous to Cav1 channels and do not bind to IQ regions (data not show). Early studies show that the DCT of these channels, particularly Cav2.1, can modulate calmodulation[37], but the mechanism for this function has yet to be determined.

Several studies have explored the role of the DCT in Cav1.2. Hulme *et al.* found that Cav1.2 channels in cardiac muscle and brain and Cav1.1 channels in skeletal muscle undergo proteolytic cleavage[28,33]. They then applied mass spectroscopy to identify the proteolytic cleavage site in Cav1.1 and argued for a similar proteolytic site in Cav1.2 (Ala1800, red arrow, **Figure 6**). They further showed that the cleaved DCTs of Cav1.2 channels can re-associate with the truncated channel backbone and inhibit channel activity[28,29]. The underlying molecular mechanism of channel inhibition is the interaction between the proximal C-terminal regulator domain (PCRD) on the truncated channel and the distal C-terminal regulator domain (DCRD) on the cleaved DCT[28,29]. The inhibitory function of the DCT from Cav1.2 seems to be consistent with observations by Adams *et al* in Cav1.3/1.4. Furthermore, PCRD is homologous to the beginning of the A region in Cav1.3/1.4 which contributes to the IQ/ICDI interaction, and DCRD is homologous to part of the ICDI region in Cav1.3/1.4 (**Figure 6**). Thus, it is likely that the PCRD/DCRD interaction is part of the interaction between the IQ-A and ICDI regions. Our study argues that this interaction is likely relatively weak in Cav1.2 channels. However, it is interesting to see that the trans-channel interaction between IQ and ICDI is much stronger, implying that ICDI$_{1.2}$ peptides may regulate some Cav1.3 splice variants. Given the evidence that DCT peptides of Cav1.2 exist due to proteolysis[28,33] or alternative promoters[30], they may regulate Cav1.3 channels, resulting in significant biological effects in neurons and cardiomyocytes, where the two channels coexist[38].

Figures

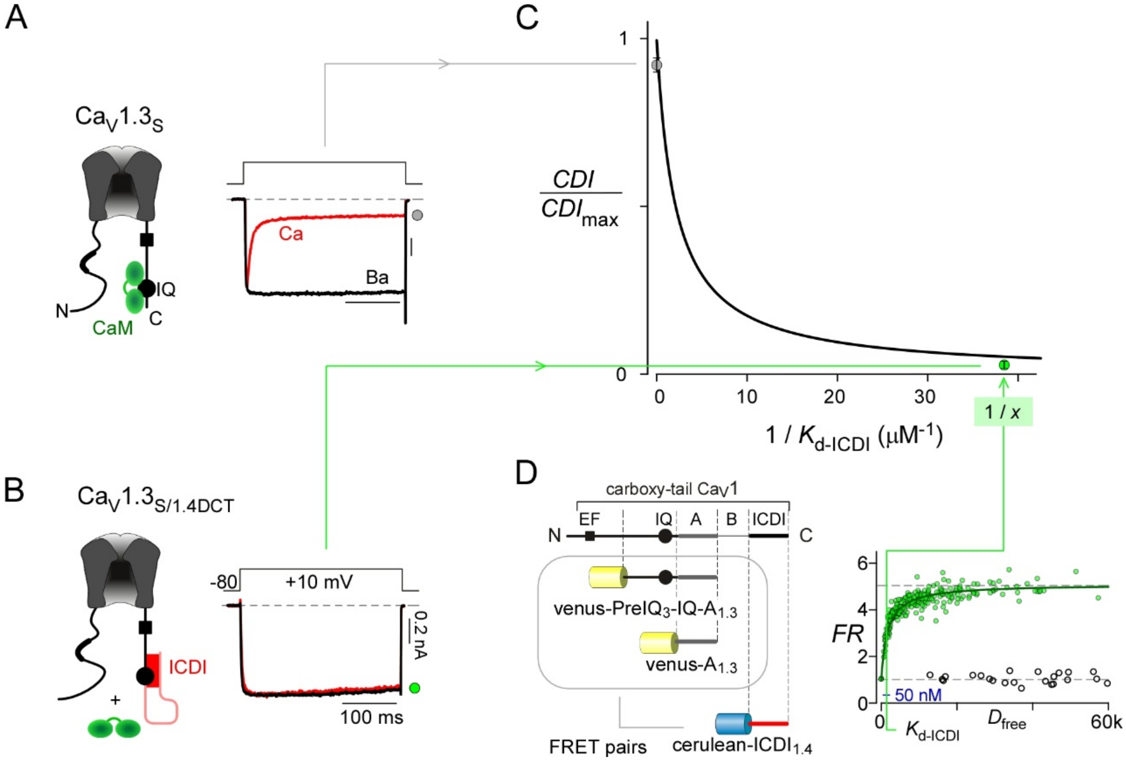
A
$Ca_V1.3_S$
IQ
N
C
CaM
Ca
Ba
B
$Ca_V1.3_{S/1.4DCT}$
ICDI
+
-80
+10 mV
0.2 nA
100 ms
C
1
0
$\frac{CDI}{CDI_{max}}$
0
10
20
30
$1 / K_{d\text{-}ICDI}$ (μM^{-1})
1 / x
D
carboxy-tail Ca_V1
EF
IQ
A
B
ICDI
N
C
venus-PreIQ$_3$-IQ-A$_{1.3}$
venus-A$_{1.3}$
FRET pairs
cerulean-ICDI$_{1.4}$
6
4
2
0
FR
50 nM
0
$K_{d\text{-}ICDI}$
D_{free}
60k

Figure 1. ICDI element weakens Ca^{2+} regulation of the channels by a competitive mechanism.

(**A**) Short splice variant of $Ca_V1.3$ channels ($Ca_V1.3_S$) exhibit strong CDI. (left) IQ element (circle, on intracellular carboxy terminus) prebinds apoCaM (green dumbbell). (right) Ba^{2+} (black trace) and Ca^{2+} (red trace) currents evoked by depolarization to +10 mV. Strong Ca^{2+} current decay in comparison to Ba^{2+} current during depolarization indicates strong CDI. The vertical scale bar applies to Ca^{2+} here and throughout. Ba^{2+} currents scaled 2-3× downward to facilitate visual comparison of decay kinetics. (**B**) Chimeric $Ca_V1.3_{S/1.4DCT}$ channels with an ICDI element (red rectangle) exhibit little CDI. (**C**) An inverse correlation between measured CDI and the binding affinity of the IQ/ICDI interaction ($1 / K_{d\text{-ICDI}}$). (**D**) FRET two-hybrid assay of IQ/ICDI interaction. FRET partners are Venus-PreIQ$_3$-IQ-A$_{1.3}$ and Cerulean-ICDI$_{1.4}$ peptides (left cartoon). Strong binding-curve (left, green curve) of wild-type FRET partners detected by live-cell FRET (green circles, each from single HEK293 cell expressing FRET partners). No FRET interaction between the A region alone and the ICDI segment (open black circle).

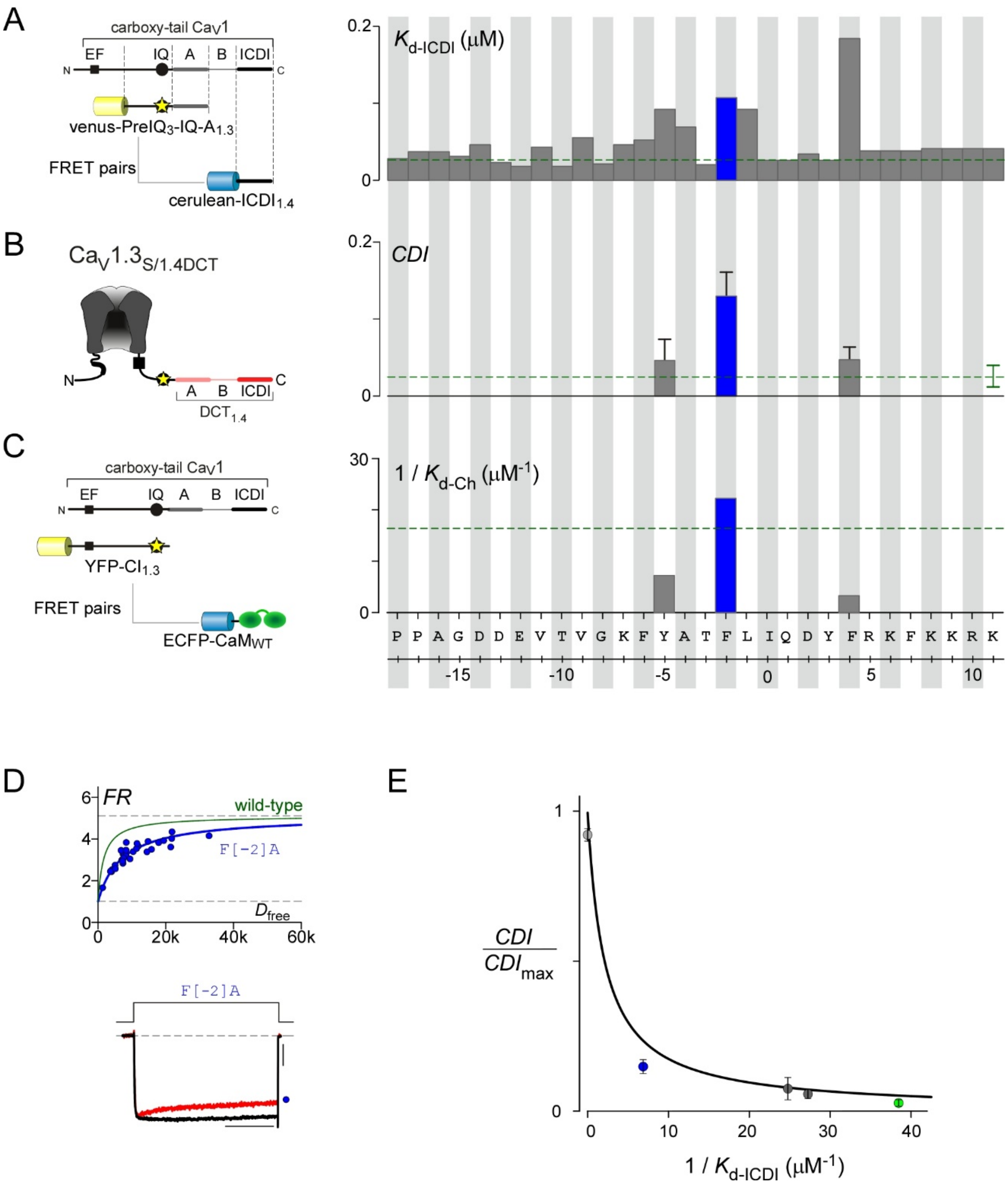
A
carboxy-tail CaV1
EF
IQ
A
B
ICDI
N
C
venus-PreIQ3-IQ-A1.3
FRET pairs
cerulean-ICDI1.4
0.2
0
Kd-ICDI (μM)
B
CaV1.3S/1.4DCT
N
A
B
ICDI
C
DCT1.4
0.2
0
CDI
C
carboxy-tail CaV1
EF
IQ
A
B
ICDI
N
C
YFP-CI1.3
FRET pairs
ECFP-CaMWT
30
0
1 / Kd-Ch (μM-1)
P P A G D D E V T V G K F Y A T F L I Q D Y F R K F K K R K
-15
-10
-5
0
5
10
D
6
4
2
0
FR
wild-type
F[-2]A
Dfree
0
20k
40k
60k
F[-2]A
E
1
0
CDI / CDImax
0
10
20
30
40
1 / Kd-ICDI (μM-1)

Figure 2. **Systematic alanine scanning of the IQ region.**

(**A**) FRET two-hybrid assay of IQ/ICDI interaction. FRET partners are Venus-PreIQ$_3$-IQ-A$_{1.3}$ and Cerulean-ICDI$_{1.4}$ peptides (left cartoon). Alanine was systematically substituted into the IQ region of Venus-PreIQ$_3$-IQ-A$_{1.3}$ (left cartoon, star), and repeated FRET two-hybrid assays were performed with Cerulean-ICDI$_{1.4}$ peptides. $K_{\text{d-ICDI}}$ measured for all constructs (right) unveiled several hotspots for IQ/ICDI binding. The green dotted line indicates the $K_{\text{d-ICDI}}$ measured for the wild-type binding partners. (**B**) CDI analysis of hotspots with the most severe impact on $K_{\text{d-ICDI}}$, using channels as diagrammed on the left. The green dotted line indicates CDI measured for the channel in **Figure 1B**. (**C**) $1 / K_{\text{d-Ch}}$, binding affinity of apoCaM to holochannel in the absence of ICDI, measured directly by FRET two-hybrid assay or derived from CDI measurements using whole-cell patch clamp described in a previous study[27]. The green dotted line indicates the $K_{\text{d-Ch}}$ measured for the wild-type binding partners. (**D**) F[-2]A illustrates decreased binding affinity (upper, blue curve), and exhibits increased CDI over wild-type chimeric channels (**Figure 1B**). (**E**) After adjustment for the alterations in $1 / K_{\text{d-Ch}}$ produced by alanine substitutions at these hotspots (**C**), CDI and binding data for these hotspot mutations (blue circles) fit well to the competitive-binding relation (black curve; Equation 1). The green circle is from CDI of the wild-type chimeric channels (**Figure 1B**) and corresponding FRET results (**Figure 1D**). The light gray circle corresponds to CDI of the Cav1.3$_\text{S}$ channel (**Figure 1A**); by definition, $1 / K_{\text{d-ICDI}} = 0$.

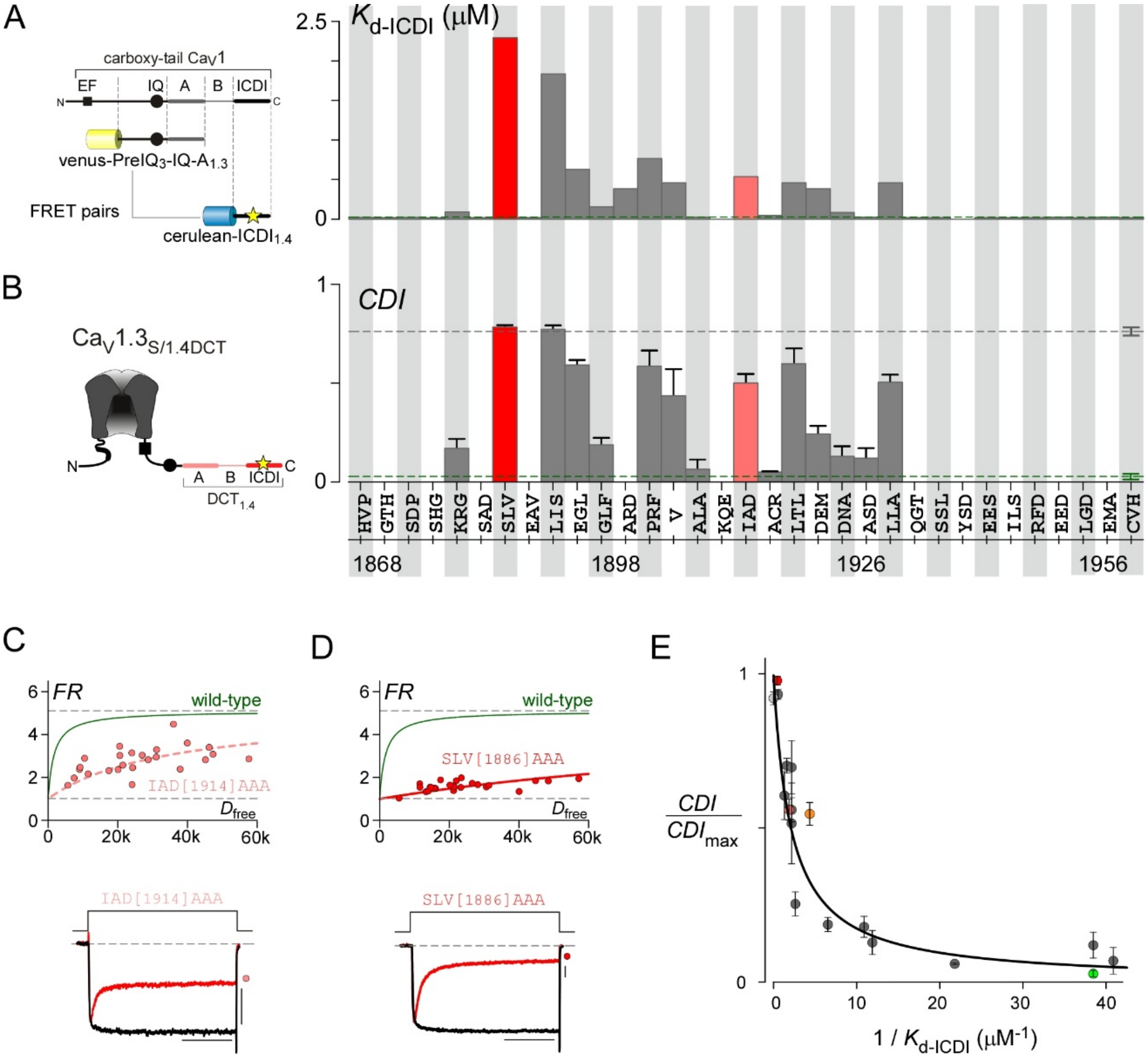
A
B
C
D
E
carboxy-tail CaV1
EF
IQ
A
B
ICDI
N
C
venus-PreIQ3-IQ-A1.3
FRET pairs
cerulean-ICDI1.4
CaV1.3S/1.4DCT
DCT1.4
Kd-ICDI (μM)
2.5
0
CDI
1
0
HVP
GTH
SDP
SHG
KRG
SAD
SLV
EAV
LIS
EGL
GLF
ARD
PRF
V
ALA
KQE
IAD
ACR
LTL
DEM
DNA
ASD
LLA
QGT
SSL
YSD
EES
ILS
RFD
EED
LGD
EMA
CVH
1868
1898
1926
1956
FR
wild-type
IAD[1914]AAA
SLV[1886]AAA
Dfree
0
2
4
6
0
20k
40k
60k
CDI / CDImax
1 / Kd-ICDI (μM-1)
0
10
20
30
40

Figure 3. Systematic alanine scanning of ICDI region.

(**A**) FRET two-hybrid binding effects of systematic substitutions of alanine into the ICDI region of Cerulean-$\text{ICDI}_{1.4}$ peptides (left, star), with Venus-PreIQ_{3}-IQ-$\text{A}_{1.3}$ as the FRET partner. $K_{\text{d-ICDI}}$ landscape of the ICDI region unveiled multiple hotspots for IQ/ICDI interaction (left and right). The green dotted line indicates the $K_{\text{d-ICDI}}$ measured for the wild-type binding partners. (**B**) CDI measured for the chimeric $\text{Ca}_{\text{V}}1.3_{\text{S/1.4DCT}}$ channels with mutations in ICDI hotspots. The light gray and green dotted line indicates CDI measured for the channels in **Figure 1A** and **B** respectively. (**C**) IAD[1914]AAA moderately reduced IQ/ICDI binding (upper) and thus partially restored CDI (lower). (**D**) SLV[1886]AAA disrupted IQ/ICDI binding to a large extent (upper) and correspondingly restored functional CDI (lower) to the level of $\text{Ca}_{\text{V}}1.3_{\text{S}}$ that lacks ICDI (**Figure 1C**). (**E**) Robust fit of CDI (**B**) and FRET binding data (**A**) (red symbols) to a competitive-binding relation (black curve, copied from **Figure 2E** as well as the light gray and green symbols). PKA phosphorylation at Ser1883 reduces the IQ/ICDI interaction and CDI (Chapter 3), which is plotted as the orange dot.

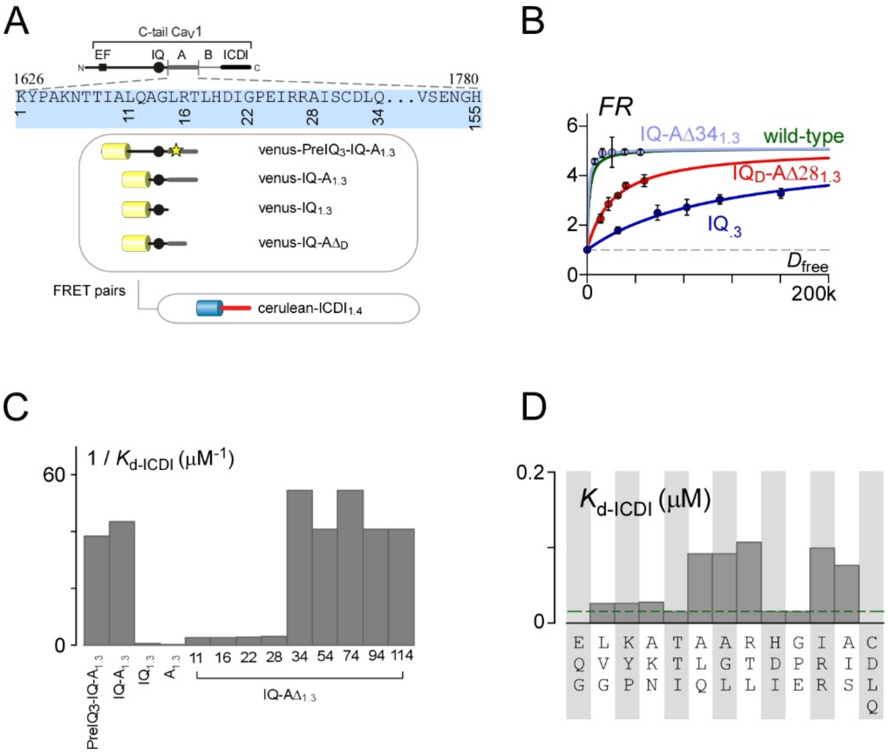

Figure 4. Exploring the role of the A region in the IQ/ICDI interaction.

(**A**) FRET interaction between Cerulean-ICDI$_{1.4}$ and various truncations of Venus-PreIQ$_3$-IQ-A$_{1.3}$. Blue box shows the sequence of the A region, with positions of residues in the A region marked underneath (boundary of A region in the channel is marked above the sequence, corresponding to **Figure 6**). (**B**, **C**) Truncating the PreIQ$_3$ region barely affected 1 / $K_{\text{d-ICDI}}$ (**B**, light blue; **C**), whereas the IQ region alone supported far weaker binding (**B**, dark blue; **C**). A series of truncations within the A region (IQ-AΔ$_{1.3}$, the number below the bar indicates the length of the remaining A region after truncation) suggest that the first 34 residues of the A region are critical for binding (**B**, **C**). (**D**) FRET two-hybrid binding effects of systematic substitutions of alanine into the critical A region of Venus-PreIQ$_3$-IQ-A$_{1.3}$ peptides (**A**, star), with Cerulean-ICDI$_{1.4}$ as FRET partner. $K_{\text{d-ICDI}}$ landscape of the critical A region unveiled multiple hotspots for the IQ/ICDI interaction.

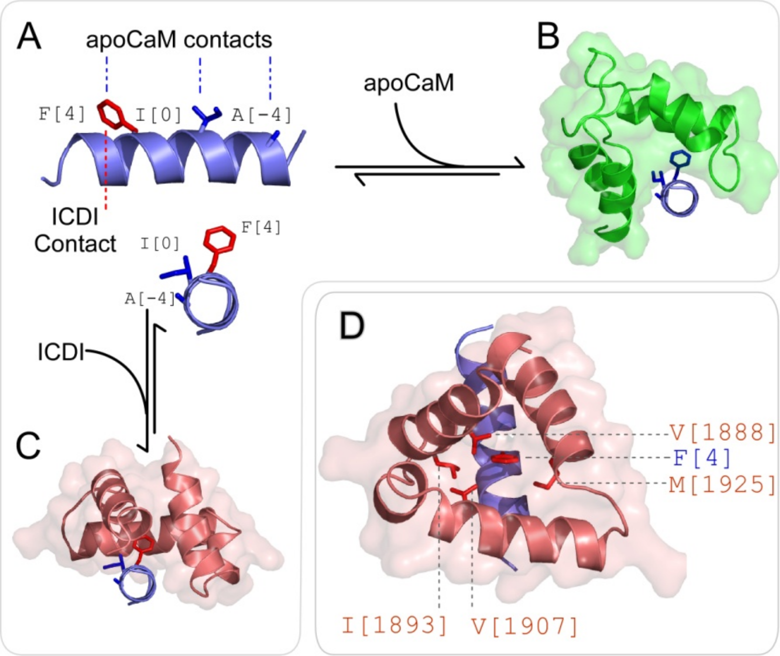

Figure 5. ***Ab initio*** **modeling of IQ/ICDI interaction, compared with IQ/apoCaM interaction.**

(**A**) F[4] (red sticks), the most significant hotspot of the IQ region (blue ribbon) for ICDI binding (**Figure 2A**), is also a hotspot for apoCaM binding (F[4] as well as I[0] and A[-4] in blue sticks). (**B**) Homology model of IQ domain complexed with the C-lobe of apoCaM (green ribbon and surface, based on NMR structure of analogous Nav1.5 complex[39]. (**C**) *Ab initio* (Rosetta) structural model of ICDI (red ribbon and surface) complexed with IQ. (**D**) Alternate view of model displayed in **C**, showing close approximation of ICDI and IQ hotspots.

Figure 6. Detailed sequence information of the DCTs from L-type Ca^{2+} channels.

Amino-acid alignments of the A, B**,** and ICDI regions from Cav1.2 (rabbit NM001136522.1), Cav1.3 (rat AF370009.1) and Cav1.4 (human NP005174). Dashed lines indicate gaps of alignment; dotted lines are omitted sequences. Coordinates of boundaries are annotated on the left of each sequence. Consensus symbols under the sequences indicate fully conserved residues (*), strongly similar residues (:) or weakly similar residues in each position. The light-red-shaded regions in the A region and ICDI region are PCRD and DCRD[28] regions respectively. The previously identified proteolytic cleavage site in Cav1.2[33] is indicated by a red arrow.. The light-blue-shaded regions are segments we identified as important to IQ/ICDI interaction in Cav1.3/1.4.

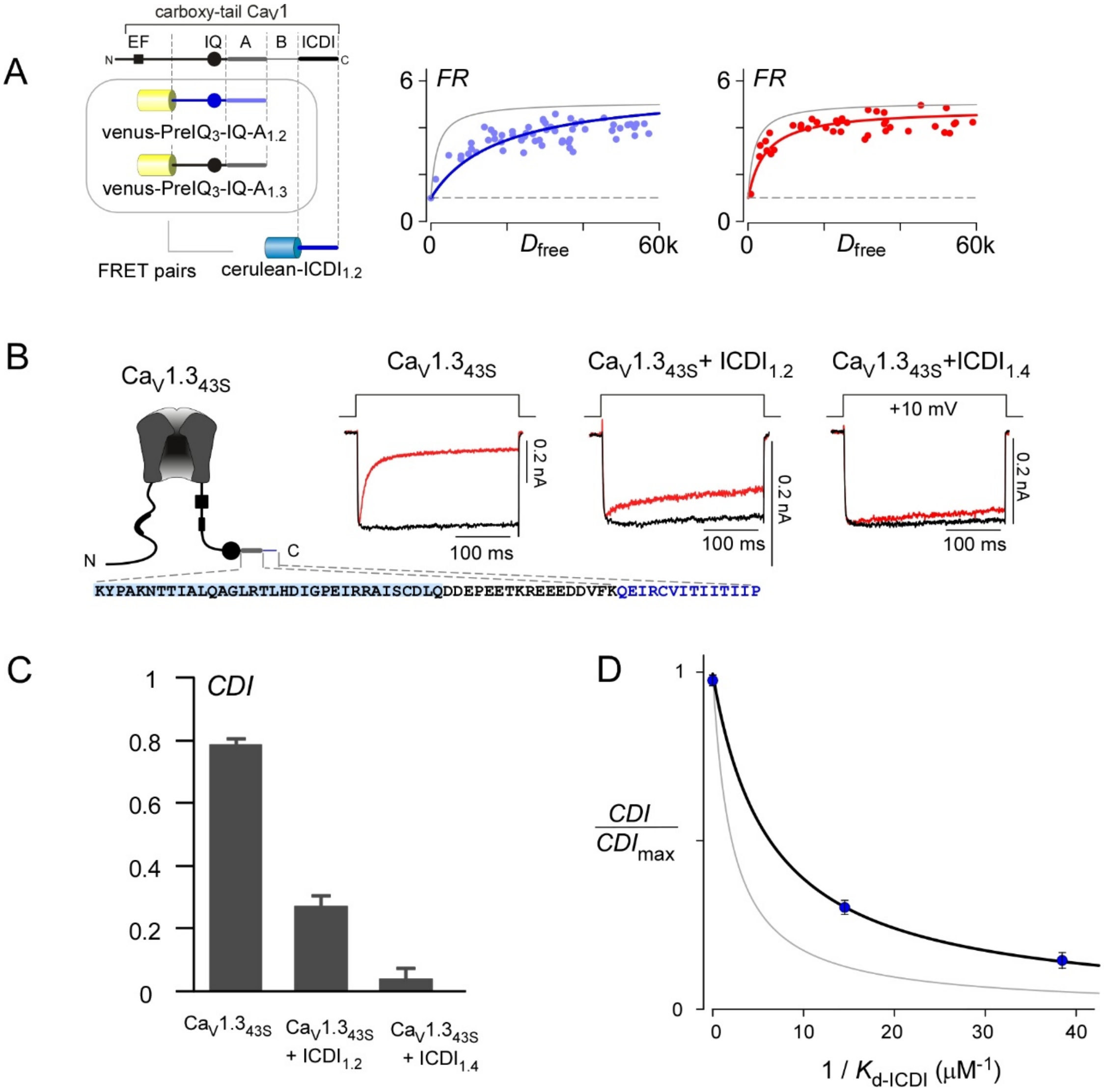
A
carboxy-tail CaV1
N
EF
IQ
A
B
ICDI
C
venus-PreIQ3-IQ-A1.2
venus-PreIQ3-IQ-A1.3
FRET pairs
cerulean-ICDI1.2
FR
6
0
Dfree
60k
FR
6
0
Dfree
60k
B
CaV1.343S
N
C
KYPAKNTTIALQAGLRTLHDIGPEIRRAISCDLQDDEPEETKREEEDDVFKQEIRCVITIITIIP
CaV1.343S
0.2 nA
100 ms
CaV1.343S+ ICDI1.2
0.2 nA
100 ms
CaV1.343S+ICDI1.4
+10 mV
0.2 nA
100 ms
C
CDI
1
0.8
0.6
0.4
0.2
0
CaV1.343S
CaV1.343S + ICDI1.2
CaV1.343S + ICDI1.4
D
CDI / CDImax
1
0
0
10
20
30
40
1 / Kd-ICDI (μM-1)

Figure 7. The ICDI$_{1.2}$ peptide binds and regulates Ca$_V$1.3$_{43S}$.

(**A**) FRET two-hybrid assay of IQ/ICDI interaction. FRET partners are Venus-PreIQ$_3$-IQ-A$_{1.3}$ or Venus-PreIQ$_3$-IQ-A$_{1.2}$ peptide and Cerulean-ICDI$_{1.2}$ peptide (left cartoon). Venus-PreIQ$_3$-IQ-A$_{1.3}$ has higher affinity to Cerulean-ICDI$_{1.2}$ (right) than Venus-PreIQ$_3$-IQ-A$_{1.2}$ (middle). The gray curves are from a binding assay between Venus-PreIQ$_3$-IQ-A$_{1.2}$ and ceruealn-ICDI$_{1.4}$. (**B**) (left) Cartoon of Cav1.3$_{43S}$, underneath the cartoon is its sequence after IQ, which is different from Cav1.3$_{42}$, another short splice variant truncated right after IQ. (right) Current exemplars show that Cav1.3$_{43S}$ by itself has full born CDI, and coexpressing ICDI$_{1.2}$ or ICDI$_{1.4}$ can reduce its CDI. (**C**) Bar graphs of CDI show the same result as **B**. (**D**) CDI and FRET binding data measured for Cav1.3$_{43S}$ coexpressed with ICDI$_{1.2}$ peptide resides on a Langmuir curve (black) right-shifted from the one used in **Figure 2** and **Figure 3**. The black curve was fitted using [ICDI] = 30 μM instead of 90 μM in the original curve, and all other parameters are the same.

Chapter 2

Novel platform for FRET binding assays

Introduction

The live-cell FRET two-hybrid binding assay is a well-established and robust method for probing protein interactions. Unlike *in-vitro* methods, binding partners of interest are expressed and measured in their native environment. Thus, FRET two-hybrid suffers from a much lower false positive rate[7] and is more likely to identify or confirm interactions with functional significance. Further, it is a quantitative method, allowing for measurement of relative binding affinities quantitatively correlated with function[8,27,40]. As such, this method has been used for a number of mechanistic discoveries[7,8,14,27,40-42]. Moreover, as there is no need to deal with solubility and other purification issues required of *in-vitro* methods, FRET two-hybrid is not only much easier to perform, but also provides a unique opportunity to study large membrane proteins such as voltage-gated calcium channels[7]. Recently, Ben-Johny *et al*. also demonstrated that FRET two-hybrid can be used to understand the stoichiometry of protein interactions[43].

However, this method also has its own limitations. First of all, because of the complexity of the optical pathways involved, FRET two-hybrid cannot not be used to obtain the absolute value of binding affinities in molar units. While calibration methods exist to convert the relative binding affinities to absolute values, it is hard to estimate the accuracy of these calibrations. On the other hand, while this method has a very low false positive rate, it suffers from a substantial false negative rate for two reasons: (1) in large protein complexes, fluorophores might exceed the Förster distance or may not reside in the ideal orientation, resulting in no FRET signal despite protein binding. This issue might be partially relieved by techniques such as optimization of the protein boundaries or fluorophore linkers[44], changing the fluorophore tagging locations, and employing circularly permutated fluorophores[45]; however, these methods are usually very time consuming and are not guaranteed to work. (2) FRET two-hybrid binding assays only work well when the dissociation constant is in the range of tens of nanomolars to a few micromolars. Low affinity binding interactions, which might have a functional significance when proteins colocalize in a native environment, may not be detected by FRET two-hybrid assays which usually use peptide segments homogeneously distributed in the cytosol. Lastly, the current platform for FRET two-hybrid assays are widefield and confocal microscope setups[7,14,46], which do not scale well for high-throughput applications such as screening for small molecules capable of disrupting protein interactions or screening for binding partners of a protein of interest.

To solve these issues, we designed novel platforms with which to perform FRET binding assays. First, we developed a lysate-based FRET assay to accurately measure binding affinities (in molar units) in a quasi-native context without protein purification. Second, we applied divalent binding with weak helpers to measure the binding affinity of weak protein interactions. Lastly, we extended the platform for FRET binding assays to plate reader and flow cytometer systems in order to study protein interactions in high throughput.

Methods

Molecular biology. The four plasmids used for making lentivirus (LV) were generous gifts from Dr. Rajesh Sekar and Professor Leslie Tung at Johns Hopkins

Universtiy, Baltimore, MD[47], including: (1) pRRLsin18.cPPT.CMV.eGFP.Wpre (named as pPPT-eGFP) , (2) pMDLg/pRRE, (3) pRSV-Rev, (4) pMD2.VSV.G. The cDNAs of Venus-PreIQ$_3$-IQ-A$_{1.3}$ and Cerulean-ICDI$_{1.4}$ were cloned into pPPT-eGFP following the removal of eGFP. The resulting plasmids pPPT-Venus-PreIQ$_3$-IQ-A$_{1.3}$ and pPPT-Cerulean-ICDI$_{1.4}$ were combined with plasmids (2)-(4) respectively for transfection to generate LV-Venus-PreIQ$_3$-IQ-A and LV-Cerulean-ICDI.

Production of lentivirus. Lentivirus was produced by PEI transfection of the four lentivirus plasmids into HEK 293T cells. The supernatant from 293T cells was collected 48 and 72 hours after transfection, filtered by 150ml Stericup (Millipore, SCHVU01RE) and concentrated using sterilized Centricon Plus-70 (Millipore, UFC710008) filters. The concentrated virus was stored at –80ºC after calculating the titer by a serial dilution assay [47,48].

Making stable cell lines using lentivirus. 5-10ul of each concentrated virus (LV-Venus-PreIQ$_3$-IQ-A$_{1.3}$ and LV-Cerulean-ICDI$_{1.4}$) were thawed quickly at room temperature and added directly to HEK293 cells. 99% of cells were infected by the virus transduction. Several rounds of infection were used to achieve the desired expression level of virus, i.e., the plateau phase of the binding curve (**Figure 13A**). Then the cells were well separated and plated on 100mm cell culture dishes (BD, 353003) at the density of approximately 1000 cells/ml, allowing the formation of single colonies. After 7-10 days in culture, single colonies were selected for proliferation and the colonies with the most homogeneous expression of the fluorophores were selected and expanded as stable cell lines. For calibration purposes (i.e. measuring FRET-convention parameters R_A and

R_D), stable cell lines expressing only Venus-PreIQ$_3$-IQ-A$_{1.3}$ or Cerulean-ICDI$_{1.4}$ were also made.

Making stable cell lines using resistance selection. HEK293 cells were transfected with Cerulean-Venus dimer in C1 plasmid [49] and grown in complete DMEM media containing 400 μg/ml G418 for 10 days. Cells that survived the G418 selection were then split and plated on 100mm cell culture dishes (BD, 353003) at a density of approximately 1000 cells/ml in order to form single colonies. After 7-10 days in culture, single colonies were selected for proliferation and the colonies with the most homogeneous expression of the fluorophores were selected and expanded as stable cell lines.

Cell culture. For microscope-based FRET optical imaging**,** HEK293 cells were plated at low density into 3.5 cm culture dishes with integral No. 0 glass cover slip bottoms (MatTek, P35G-0-14-C) and cultured for 1-3 days in complete DMEM media, i.e. DMEM media (Mediatech, 10-013-CV) supplemented with 10% Fetal Bovine Serum (Hyclone, SH30071.03), 2 mM L-Glutamine (Gibco, 25030), 50 IU/ml Penicillin, 50 μg/ml Streptomycin (Mediatech, 20-001-CI), 10 μg/ml Gentamicin (Quality Biology, 120-098-66IEA).

For plate-reader-based FRET optical imaging, cells were resuspended in complete DMEM at the density of 400,000 cells/ml and loaded into BD Biocoat 384-well plates (BD, 354663) at 50 μl per well and incubated for 24 hours at 37 °C and 5% CO_2. As shown in **Figure 14A**, columns 1-2 of the 384-well plate were plated with control cells (rows A-D), Venus-only (rows E-H), and Cerulean-only (rows I-L) cells for calibration;

rows M-P of columns 1-2 were plated with the stable cell line used for screening, without the addition of drug, as negative control. Columns 3-22 were plated with the stable cell line used for screening the Library of Pharmacologically Active Compounds (LOPAC, Sigma-Aldrich). Columns 23-24 were plated with the stable cell line used for screening (rows A-H) and another stable cell line with less CaM expression (rows I-P); ionomycin was added to cells cultured in these two columns as a positive control.

Transient transfection. cDNAs of Venus-PreIQ$_3$-IQ-A and Cerulean-ICDI (wild type or mutant) were cloned into pcDNA3 plasmids and transiently transfected by PEI (Polysciences, 23966-2) into HEK293 cells, which then were incubated at 37 °C in 5% CO_2 for 1-2 days.

Microscope-based FRET optical imaging. Cells were washed, bathed in HEPES-buffered Tyrode's solution (pH 7.35) containing 10mM Ca^{2+}, and assayed with a Nikon TE300 Eclipse microscope (40× 1.3 n.a. oil objective) and custom fluorometer system (University of Pennsylvania Biomedical Instrumentation Group). Each individual cell was picked by an image-plane pinhole, and epifluorescence emission from the entire cell was measured by the three-cube FRET method[14]; 30-50 individual cells were measured and analyzed as described previously[14], to generate a binding curve.

Plate-reader-based FRET optical imaging. Cells were washed, bathed in Tyrode's solution containing 10 mM Ca^{2+}. As shown in **Figure 14A**, compounds from the LOPAC or Molecular Libraries Small Molecule Repository (MLSMR, Evotec Inc.) libraries were added to columns 3-22 at 25 μM, and ionomycin was added to columns 23-24 using a serial dilutions factor of 1 : 3 (from A to H, and from I to P), starting at 13.3

μM. Cells were incubated at room temperature for 10 min after adding the library compounds and then mounted on a Safire[2] plate reader (Tecan) or Perkin Elmer 2102 Envision, measured and analyzed by a three-cube FRET method as described previously with modifications[14].

Flow-cytometer-based FRET optical imaging. FRET two-hybrid experiments were performed on an Attune Acoustic Focusing Cytometer (Life Technologies) as described[49]. Cells were trypsinized and resuspended in Tyrode's solution before loading onto the flow cytometer. The previously described algorithm [7,14] was used to calculate acceptor-centric measures. In total, signals from 1,000-10,000 cells were recorded and analyzed by home-made software written in MATLAB.

Cell lysate preparation. Cells were trypsinized and washed twice in HEPES-buffered Tyrode's solution (pH 7.35) containing 2mM Ca^{2+}, and precipitated by centrifugation and weighed. Physiological lysis solution (100μl lysis solution per 100mg wet weight of the cell pellet) was added and cells were lysed by one cycle of freezing and thawing. The insoluble fraction was removed by centrifugation.

The physiological lysis solution contained (in mM): KCl: 20; K-gluconate: 120; $MgCl_2$: 2; EGTA: 0.2; HEPES: 10 (pH 7.4); Na_2-ATP: 2; DTT: 10; EDTA-free protease inhibitor cocktail (Roche): following instruction; at 305 mOsm adjusted by K-gluconate.

Absorption and excitation spectrum measured for cell lysate. Absorption spectra were measured by UV-Vis spectrophotometer (Beckman) with an ultra micro quartz cuvette (0.05mL, z = 8.5mm). Excitation spectra were measured by fluorolog FL3C-21 (Georgia Tech)

Lysate-based FRET optical imaging. 10-20ul of cell lysates were loaded on No. 0 glass cover slip bottom (MatTek, P35G-0-14-C) and quickly measured (before evaporation) on a Nikon TE300 Eclipse microscope (40× 1.3 n.a. oil objective) and custom fluorometer system (University of Pennsylvania Biomedical Instrumentation Group). The lysate droplet was large enough to cover the whole field picked by an image-plane pinhole. However, the droplet had depth and a number of focal planes. To be consistent, the readings were obtained at the maximal output of the PMT. Epifluorescence emission was measured and analyzed by the three-cube FRET method[14]. To obtain lysates with lower concentrations of the fluorescent protein, lysates from cells with fluorescent protein expressed were diluted 1:1 using lysates from cell without fluorescent protein expression. Even though we carefully adjusted the amount of lysis solution when preparing cell lysate, there was still variability in the cell and lysate concentration from trial-to-trial. Thus, lysis solution was added to each lysate such that the absorbance was adjusted to 0.3 AU at 670nm before any measurements and dilutions.

Ionomycin effect. Ionomycin (Sigma-Aldrich, I0634) was dissolved in 99.5% DMSO (Sigma-Aldrich, D5879) to form a 10mM stock, and diluted by a Tyrode's solution containing 10mM Ca^{2+} to a final concentration of 10μM. Cells were incubated in this solution for 10min before measurements were made.

Results

Lysate-based FRET assay to measure binding affinity

The basic idea of the lysate-based FRET assay is to use the absorption spectrum to accurately measure the concentration of fluorescent proteins, and calibrate the relative binding affinities measured by FRET binding assays to absolute values in molar units. First, we obtained absorption spectra of lysates from cells without expression of any fluorescent proteins (background lysate). As illustrated in **Figure 8A and B**, background lysates could have high absorption, especially at short wavelengths (**Figure 8A, B**, gray traces), which is caused by endogenous proteins, nucleotides and autofluorescent materials such as NADPH and flavins. Even though the absolute value of the absorption spectrum at a certain wavelength varies from one experiment to another due to variability in preparing lysates (see **cell lysate preparation** in **Methods**), the overall shape of the spectra are always the same, and can overlap well if scale by a constant value. Next, we measured the absorbance of lysates from cells expressing the Venus-PreIQ$_3$-IQ-A$_{1.3}$ peptide (Venus lysate). Its absorption spectrum shows a peak around 515nm (**Figure 8A**, light green trace), a feature of the absorption spectrum of the Venus fluorescent protein. Importantly, the spectrum between 530nm to 670 nm of background lysate and Venus lysate overlay well if scaled by a constant value. After background subtraction (after scaling, see **Methods**), the absorption spectrum of the Venus lysate is close to zero beyond 530nm (**Figure 8A**), and overlays well with excitation spectrum of the Venus fluorescent protein beyond 470 nm (**Figure 8C**). While the absorption spectrum is easily affected by various endogenous materials in the lysate, the excitation spectrum of a fluorophore is virtually unaffected by other materials. Indeed, the excitation spectra of purified Venus fluorescent proteins and Venus lysate are very similar (data not show). Thus, the nice overlay of excitation spectrum of the Venus fluorescent protein and the background-subtracted absorption spectrum of the Venus lysate indicates that after background-subtraction, the absorption of the Venus lysate is mainly due to Venus protein. Accordingly, we can measure the concentration of the Venus-PreIQ$_3$-IQ-A$_{1.3}$ peptide in the lysate from the absorption peak, which is 4.68 μM. Similarly, absorption and excitation spectra were measured for lysates from cells expressing both expressing Venus-PreIQ$_3$-IQ-A$_{1.3}$ and Cerulean-ICDI$_{1.4}$ peptides (dual-fluorophore lysate). We can see that after background subtraction, the absorption spectrum of the dual-fluorophore lysate also overlays well with the sum of the excitation spectrum of the two fluorophores (both excitation spectra were scaled to match the peak of the background subtracted absorption spectra) (**Figure 8B**, **D**). Accordingly, the concentration of Venus-PreIQ$_3$-IQ-A$_{1.3}$ in the dual-fluorophore lysate was 1.63 μM, and the Cerulean-ICDI$_{1.4}$ peptide in the dual-fluorophore lysate was 4.73 μM.

Next, we tested whether or not the peptides in lysates bind in a similar manner as when expressed in cells. We know that apoCaM binds to the IQ domain of Ca$_V$ channels, and thus serves as a competitive inhibitor of the IQ/ICDI interaction. In addition, Ca^{2+}/CaM binds to the IQ region with higher affinity, and thus can server as a more potent competitive inhibitor of the IQ/ICDI interaction. Our hypothesis is that if the peptides interact similarly in lysates as in cells, they will have similar FRET ratios (*FR*) and a similar response to competitive inhibitors. We can see that the *FR* of the dual-fluorophore lysate (**Figure 9A**, left bar) is the same as the *FR* of the dual-fluorophore in cells (cells from which dual-fluorophore lysate were generated) (**Figure 9B**, left bar). In addition, when Ca^{2+} is elevated by adding calcium chloride to the lysate, or by applying ionomycin to the cells, the *FR* values of the two decrease to the same level (**Figure 9A**, middle bar vs **B**, right bar). We suspected that the endogenous expression of CaM is not high enough to fully inhibit the IQ/ICDI interaction, even with elevated Ca^{2+}. Thus, we used another stable cell line in which CaM is also overexpressed (dual-fluorophore-CaM cells). These cells and their lysates have slightly reduced baseline FR values (left bars in **Figure 9C**, **D**) compared to cells and lysates without CaM overexpression (left bars in **Figure 9A, B**), as expected given that apoCaM is not a very potent competitive inhibitor of IQ/ICDI interaction[50]. However, when Ca^{2+} is elevated in either the lysate or the cells, the *FR* values are largely reduced to a very similar level (**Figure 9C**, middle bar vs **D**, right bar). Moreover, adding additional purified CaM to the dual-fluorophore-CaM lysate did not further reduce its *FR* value. In contrast, adding additional purified Ca^{2+}/CaM to the dual-fluorophore lysate (**Figure 9A**, right bar) further reduces the *FR* value to the same level as the dual-fluorophore-CaM lysate with addition of Ca^{2+} (**Figure 9C**, middle bar). The consistency of *FR* values measured for the IQ/ICDI interaction in both the lysate and live-cell context, as well as their similar response to competitive inhibitors, confirms that both peptides maintain their natural conformation in the lysates, and the context for the binding reaction is very similar.

With evidence that the IQ/ICDI interaction is quite similar in lysates and in intact cells, we were well prepared to perform the lysate-based three-cube FRET binding assay.

We first obtained the binding curve for the dual-fluorophore lysate. To obtain lysate with a lower concentration of the fluorescent-protein-tagged peptides, we diluted the dual-fluorophore lysate with background lysate (see **Lysate-based FRET optical imaging** in **Methods**). A binding curved was generated for the dual-fluorophore lysate (**Figure 9E**). From this binding curve and the protein concentrations measured by absorption spectra, the dissociation constant of the IQ/ICDI interaction was measured to be 0.12 μM, which is about four fold higher than our previous estimation based on guesstimation of optical component parameters (**Figure 3**). From the results from **Figure 9A-D**, we expect that the binding affinities of this interaction should be very similar in cells or in lysates. The close agreement of the two values also verifies this point. On the other hand, the same interaction measured using the lysate from cells with CaM overexpressed showed a much lower binding affinity (**Figure 9F**, the dissociation constant was measured as 770 μM), indicating that this method can take the cellular context of a protein interaction into account. Another piece of evidence supporting this idea can be seen in **Figure 9G**. If we diluted the dual-fluorophore lysate with lysis buffer, rather than with background lysate, we obtain a different binding curve. This is likely due to some unknown proteins in the cellular context affecting this interaction, which most likely serve as mild inhibitors. Thus, if we diluted the lysate by lysis buffer, these mild inhibitors were also diluted, resulting in an artificially higher measured binding affinity.

There is a linear relationship between the effective binding dissociation constant ($K_{\mathrm{d,EFF}}$) measured by a live-cell FRET binding assay, and the absolute dissociation constant (K_{d}) in molar units, which can be represented as:

$$K_{d,EFF} = c \cdot K_d \quad (2)$$

where c is a constant incorporating optical component parameters and cell volume. This equation was derived in the supplementary material of Erickson *et al*[14]. The basic idea is D_{free}, which refers to relative concentration of unbound Cerulean-tagged peptide (relative free donor concentration), is derived based on the integral of the fluorescence emitted from a whole cell assuming a constant cell volume. Thus, the larger the cell volume, the higher the measured D_{free} corresponding to a certain level of the actual free donor concentration. Accordingly, $K_{d,EFF}$, which is in the D_{free} unit, is also linearly related to cell volume. Here we measured $K_{d,EFF}$ = 1,700 D_{free} units, and K_d = 0.12 μM, which allows us to estimate the value of c as 14,166 D_{free}/μM. As Equation 2 is always true for all binding interactions, this calibration allows us to estimate the absolute binding affinities for all relative binding affinities measured by the live-cell FRET binding assay in the same cell type (HEK293 in our case). To determine c for FRET two-hybrid assays in other cell types, the ratio of the cell volume of that cell type and HEK293 cells has to be multiplied to multiplied to 14,166 D_{free}/μM.

Weak helpers facilitate detection of weak interactions

FRET two-hybrid assays sometimes fail to detect protein interactions. One example is the interaction between the A region and the ICDI region. From our alanine scanning study (Chapter 1), it is clear that the A region forms an interface with the ICDI region (**Figure 4**); however, no FRET is detected between the two domains (**Figure 1A**, open black circles). As mentioned before, the lack of FRET might be caused by a long distance or less favored orientation of the fluorophores (**Figure 10A**), or a weak binding affinity. How can we resolve these issues? We were inspired by a recent study that utilized weak helpers to improve the dynamic range of FRET sensors[51]. In their design, the fluorophores are sandwiched by binding partners of interest and weak helpers (**Figure 10B**). These weak helpers are small peptides that bind with low binding affinities (dissociation constants between 30μM to above 1000μM) and are irrelevant to the binding partners of interest. Without weak helpers, the binding partners interact and bring the two fluorophores close to each other, however the fluorophores can still freely tumble and move around[52], which leads to a larger average distance between the two and thus a low FRET efficiency. The weak helpers, whose affinity is too low to cause artificial background FRET by themselves, can interact when the binding partners bind and bring them close (**Figure 10B**). The divalent interaction locks the fluorophores close to each other in a more constrained configuration, and increases the FRET efficiency. In addition, the divalent binding results in a higher binding affinity than either interaction alone, and thus can be used to detect weak interactions. A simplified model shows that the affinity of divalent binding is proportional to the binding affinity of the weak helpers, from which we can estimate the binding affinity of the partners of interest.

We first applied this technique to the interaction between $IQ_{1.3}$ (without A region) and $ICDI_{1.4}$ peptides. From **Figure 4B**, we know $IQ_{1.3}$ and $ICDI_{1.4}$ peptides can bind with low affinity but still generate FRET signals. Previously we determined that the effective dissociation constant of interaction between $IQ_{1.3}$ and $ICDI_{1.4}$ is 60,000 D_{free} units (**Figure 4B**), from which we can estimate the dissociation constant of $IQ_{1.3}$ and $ICDI_{1.4}$ peptides to be 4.27μM (see also in **Lysate-based FRET assay to measure binding affinity**). With that, we performed the divalent FRET two-hybrid binding assays between $IQ_{1.3}$ and $ICDI_{1.4}$ peptides with the flow cytometer (see more in **Live-cell FRET binding assay by flow cytometry**). We first made FRET constructs as shown in **Figure 10B**, where the red shape is the $IQ_{1.3}$ peptide and the green shape is the $ICDI_{1.4}$ peptide. Four pairs of weak helpers were employed: SH3 domain and its binding peptides Sp1 or Sp2, and the WW domain and its binding peptides Wp1 or Wp2. With the weak helper, we achieved more robust FRET signals and higher binding affinities (**Figure 11A**). As expected, there is a linear correlation between binding affinities of the weak helpers and the binding affinities measured by the FRET assay (**Figure 11B**). The slope of the linear fit, which is 0.019 in this case, is equal to the ratio of the dissociation constant of the IQ/ICDI interaction and the effective local concentration of the weak helpers when IQ and ICDI are bound. Accordingly, we can estimate the effective local concentration to be 400μM, which is higher than the dissociation constant of the weak helper. The fact that the weak helpers have dissociation constants between 30-170μM has two main advantages: they are not too high to cause background FRET, and they are high enough to form divalent binding when the peptide of interest binds.

Next we performed the divalent FRET two-hybrid binding assay between $A_{1.3}$ and $ICDI_{1.4}$ peptides. We know that we cannot detect any binding without a weak helper (see Chapter 1). Now, with the weak helper, we were able to obtain binding curves (**Figure 12A**). Similar to **Figure 11B**, there is a linear correlation between the binding affinities of weak helpers and the binding affinities measured by FRET assays (**Figure 12B**).

Assuming the local concentration of weak helpers is around 400μM, we estimate that the dissociation constant between A and ICDI peptides is about 10μM, similar in strength to the IQ/ICDI interaction. Thus, the A region indeed binds to the IQ region; however two factors appear to inhibit our ability to detect this binding via standard FRET two-hybrid assays: (1) the binding affinity is at the limit of detection using the FRET binding assay, and (2) the A region is much bulkier than the IQ region and likely creates significant steric hindrance preventing the fluorophores from remaining in close proximity. Nonetheless, with the aid of a weak helper, we now can estimate the binding affinity of this interaction.

FRET-based HTS for molecules interfering with protein interactions

The IQ/ICDI interaction serves as a prototypic target for high-throughput screening, for two reasons. First, we have extensively characterized this interaction. The binding affinity of this interaction is at a desired range where overexpression in heterologous systems can easily saturate the binding, providing an optimal FRET readout, and perturbation is readily observable. In addition, the systematic alanine scanning done in Chapter 1 suggests that individually disrupting distinct and distributed segments of the IQ/ICDI interface suffices to disrupt the global interaction and its function (**Figure 5D**, V[1888] and I[1893] on ICDI, F[4] on IQ). Thus, it is very likely that a small molecule could substantially impact this interaction without requiring simultaneous disruption of the majority of the contact interface. More importantly, while pharmaceutical compounds modulating the gating of L-type Ca^{2+} channels (Cav1 class) have long been available[53], none exhibit sufficient selectivity among the various subtypes of Cav1 channels, despite growing awareness of subtype-specific roles in physiology and pathophysiology as well as significant effort devoted to searching for such molecules. This impasse results in part from the high degree of homology among Cav1 subtypes. A recent report by Kang *et al.* reported the discovery of a Cav1.3 specific antagonist[54], however the specificity of the compound has been disputed by later studies[55,56]. Thus, subtype specific ICDI modulation of CDI looms as an attractive target for the discovery of selective small-molecule modulation of Cav1.3 channels. Such a compound promises great pharmaceutical potential, as Cav1.3 is proposed to be a major source of Ca^{2+} toxicity in Parkinson's disease[57].

As a first step towards translating our microscope-based assay of IQ/ICDI interactions into a high-throughput plate-reader format, we created stable HEK293 cell lines expressing relevant FRET pairs and fluorophore controls. The reason we used separate fluorescent tagged IQ and ICDI peptides instead of a unimolecular sensor composed of both peptides is to maximize the FRET signal change caused by potential IQ/ICDI disrupting compounds. As a single dosage would be used in the primary screen of a large number of candidate molecules, it is possible that some molecules may only partially disrupt the binding at the test dosage. If the fluorophores are covalently linked in a unimolecular configuration, they might still be close enough to each other when the binding is partially or even largely disrupted, producing a small change in the FRET signal and potentially giving in a false negative result. With the peptides expressed separately, we expect to get larger FRET signal changes in response to interaction disrupting compounds. The challenge of using separate binding partners instead of a unimolecular sensor is to express the peptides at a level where binding is just saturated, which allows the largest FRET change due to binding interference by a small molecule. To make stable cell lines with the optimal expression level, we used lentivirus to integrate the genes of interest into the host genome. The advantage of using lentivirus, rather than traditional resistance selection, is that cells with various level of expression can be generated by titrating the amount of virus used for infection[58]. Then, by single colony selection, we can identify cell lines with desired expression level of fluorescent proteins.

Microscope-based FRET characterization of these stable lines is displayed in **Figure 13A**. Cells expressing Cerulean and Venus as separate molecules yielded negligible binding, as viewed on the same binding-curve display format (**Figure 13A**, green symbols). By contrast, cells expressing a Cerulean-Venus dimer exhibited uniformly high FRET (red symbols). For cells stably expressing the Venus-PreIQ$_3$-IQ-A$_{1.3}$ and Cerulean-ICDI$_{1.4}$, data points were reassuringly situated on the plateau phase of the binding curve (**Figure 13A**, black symbols), with a binding-curve fit from data from the same wild-type FRET pairs transiently expressed in HEK293 cells (green curve, **Figure 2A**) reproduced for reference. Also gratifying was the sharp drop in FRET in these cells (**Figure 13A**, blue symbols), upon coexpressing CaM and elevating Ca^{2+} with ionomycin to disrupt the IQ/ICDI interaction via competition[8]. The difference between the black and blue data thereby gauges the dynamic range of our assay. Because of the position of the IQ/ICDI interaction data on the plateau of binding curves, all of these outcomes could be converted into an aggregate bar-graph format (**Figure 13B**), more amenable to later comparison with plate-reader outcomes. The color code here follows that in **Figure 13A**, and *z* scores and *S/N* ratio computed for the observed dynamic range are remarkably good. We next assayed these same stable cells on a *tecan safire* multi-well plate reader, with the help of Meng Wu at the Johns Hopkins Ion Channel Center (JHICC). Characterization of cells expressing Cerulean or Venus alone yielded FRET-conversion parameters (R_A and R_D, used to calculate FR[7,14,59]) that were highly similar to those obtained on our microscope platform (**Figure 13C**). Importantly, controls and IQ/ICDI interactions yielded results in the plate-reader format (**Figure 13D**) that were similar to those obtained on the microscope-based platform (**Figure 13B**). Dose-dependent augmentation of intracellular Ca^{2+} with ionomycin yielded a smoothly-graded decrease in IQ/ICDI FRET (**Figure 13E**), engendering confidence in the robust *z* scores and *S/N* ratio calculated for the plate-reader format (**Figure 13D**, **F**).

Thus encouraged, we undertook a preliminary 1280-compound screen (LOPAC library) for candidate IQ/ICDI disrupters, again with the help of Meng Wu at the Johns Hopkins Ion Channel Center (JHICC) (**Figure 14**). Panel A shows the layout for a single-multi-well plate and panel B shows the results of the LOPAC screen in a heat-map format. The IQ/ICDI FRET interaction in the presence of various compounds appears in columns 3-22. Fluorescence controls are in columns 1-2, and ionomycin gradients confirming the dynamic range of the assay are in columns 23-24 (see legend and Methods for details). Most of the IQ/ICDI wells showed FRET *FR* values ~10, demonstrating the consistency of IQ/ICDI FRET in the absence of hits. Panel B displays the results from multiple plates in a linear graphical format, where the *x*-axis plots compound number, and the *y*-axis plots the FRET *FR* metric. Three compounds appeared to be potential candidate hits (**Figure 14C**, red symbols), yielding substantial decrements in the FRET metric *FR*. Their chemical compositions are reproduced below the corresponding symbols. Two of the potential hits are also visualized in **Figure 14B** as cyan-colored wells in columns 3 and 5. By contrast, some compounds increased apparent FRET (gray symbols), likely due to spurious fluorescence of the added compound. We favor this interpretation because FRET-channel signals increased without a concomitant Cerulean-channel decrease, as would be expected of a bona fide increase in FRET. Overall, the results of this provisional LOPAC library screen bolster confidence in the feasibility of a large-scale screen.

With the above preliminary studies, we were supported by a RO3 grant to screen small molecules that disrupt the IQ/ICDI interaction of Cav1.3/1.4 channels, using the MLSMR library of 350,000-500,000 compounds. We collaborated with the Broad Institute Probe Development Center (BIPDeC) for the primary screen. As BIPDeC did not have a *tecan safire* plate reader, we performed the assay on a *Perkin Elmer 2102 Envision* Instrument. We first tested the ionomycin response of our stable cell lines (the same experiment as **Figure 13D**). With the help of Carl Apgar at Perkin Elmer, we were able to optimize the instrument to reduce the integration time of signal detection to 1 second, crucial for screening the large compound library in a reasonable amount of time. Moreover, we achieved better performance in terms of signal to noise ratio as compared to the *tecan safire* plate reader.

As small molecules affecting fluorescent proteins Venus or Cerulean, or perturbing intracellular Ca^{2+} concentrations could change the FRET signal without genuinely disrupting the IQ/ICDI interaction, counter-screens were designed for eliminating such molecules. To counter-screen small molecules affecting the fluorescent proteins, a stable cell line expressing a Cerulean-Venus dimer was created by a traditional resistance selection method. Lentivirus cannot be used to generate cell lines expressing two covalently linked fluorophores, due to the recombination of the closely related fluorescent protein sequences in the viral DNA[60]. To counter-screen small molecules perturbing intracellular Ca^{2+} concentrations, use of a Ca^{2+} dye is proposed. Although stable cell lines maintain the desired expression level for at least 20 to 30 passages, the expression level eventually would diminish after many passages or multiple rounds of freeze and thaw. Unfortunately, cell lines sent to BIPDeC were subjected to excessive freeze/thaw cycles, resulting in a degraded signal to noise ratio in their ionomycin response before starting the MLSMR library screen. In addition, time constraints meant that the planned counter screens could also not be performed. Nonetheless, the scree produced several potential hits, and we tested four compounds in their top hit list (http://pubchem.ncbi.nlm.nih.gov/assay/assay.cgi?q=&aid=743397), which did not show obvious perturbation of the fluorescent proteins. Those compounds all reduced the FRET signal of the stable cell lines, but did not pass the counter screens: two compounds affected the fluorescent proteins and two compounds elevated intracellular calcium concentration.

Live-cell FRET binding assay by flow cytometry

While three-cube FRET binding assays on wide-field and confocal microscope setups[7,14,46] have been successfully applied to detecting protein interactions and measuring their relative binding affinities in multiple studies [27,40], it is labor intensive and time consuming. A high throughput three-cube FRET binding assay is highly desirable for identification of protein interactions on a large scale. In collaboration with Shin Rong Lee (Calcium Signals Lab, Johns Hopkins), we adapted the 3-cube FRET binding assay to a flow cytometry platform. Flow cytometers can quickly screen multiple cells, and with that, we can build a binding curve in one-hundredth of the experimental time compared to a microscope setup, generating many more data points.

Calibration of the flow cytometer to obtain the necessary parameters were performed by Shin Rong Lee[49]. To prove that comparable results can be obtained with a flow cytometer as compared to a microscope-based method, we repeated FRET binding assays for several mutants used in the alanine mutagenesis studies (Chapter 1). It is clear that we can obtain similar binding curves with many more data points with the new flow cytometer setup (**Figure 15A-C**). Moreover, the relative binding affinities measured by both setups are very similar (**Figure 15D**).

Discussion

There are two major approaches for measuring the binding affinities of protein interactions: chemical assays or optical assays[61]. Chemical assays usually require protein purification, which is not feasible for many proteins, especially large membrane proteins. In fact, we found it was even challenging to purify the small segments from the intracellular domain of Cav channels. In order to obtain a sufficient amount of starting material, we tried to express these constructs in bacterial expression system, but found severe protein degradation at an early stage of the purification (data not shown). Further, the bacterial expression system and *in vitro* testing environment are very different from the cellular context, so the binding affinities measured for protein interactions by chemical assays might not be the same as that in native context, especially for mammalian protein targets. On the other hand, as the target proteins are purified, it is easy to measure their concentration, and thus measure the absolute binding affinity in molar units. Moreover, as it is easier to manipulate the concentration of proteins in *in vitro*, people can accurately measure binding affinities spanning from picomolar to millimolar range. The optical assays, on other hand, have major benefits over *in vitro* assay as they can quantitatively measure protein binding affinities in live cells. Thus, tedious protein purification issues can be totally avoided. More importantly, these assays can be applied in different cell types, allowing observation of the regulation of binding affinity in specific cell types (Chapter 3).

However, one major constraint of optical assays comes from the complicated optical system, which is hard to calibrate and obtain absolute binding affinities. In this study, we developed a lysate-based FRET two-hybrid binding assay, which can measure the absolute binding affinities without protein purification. We used absorption spectra to measure the concentration of fluorescent proteins. Even though the endogenous cellular context can contribute to the absorption spectrum, they tend to have low absorption at high wavelengths, where the fluorescent protein, especially Venus, has its feature peak. With careful background subtraction, we confirmed that the remaining absorption is caused solely by the fluorescent protein, as the corrected absorption spectra overlap well with excitation spectra. One assumption is that the concentration of the fluorescent protein is the same as the peptide to which it is tagged, i.e. no degradation and proteolysis happens. This was confirmed by a western blot (data not shown).

Now the major concern is the similarity of the live cell environment and the cell lysate. Inevitably, lysing the cell destroys many cellular organelles and exposes the intracellular proteins to the air. Here, by carefully selecting a lysis solution which is very close to the intracellular solution, and using a minimal amount of lysis solution, we attempted to keep the environmental changes and dilution effects on the cellular content as little as possible. One underlying assumption of the live-cell FRET two-hybrid assay is that the fluorescent protein tagged binding partners are homogeneously distributed in the cytosol. Thus, disruption of cellular organelle is less likely to affect the interaction; however, disruption of the cytoskeleton and changes in solubility of some endogenous proteins due to lysis might be more problematic. Luckily, our binding partners were not significantly affected by these issues (**Figure 9A-D**). One thing to be noticed is that the protein binding partners have to be expressed at a high level, allowing us to use dilution in order to obtain the entire binding curve. As the expression level required is relative to the binding affinity, this method is not suitable for weak interactions. Here, we used stable cell lines since all cells have similar and sufficient expression, but high expression can also be achieved by efficient transfection[62] and lentiviral induction. As there are several constraints, not all binding partners will be suitable for the lysate FRET assay. However, paired with a live-cell binding assay of the same protein interaction, it allows us to calibrate the optical platform (Equation 2), and measure the absolute value of the binding affinity using a live-cell binding assay.

Another constraint of live-cell FRET binding is that it can only measure binding affinities within a narrow range (between tens of nanomolars and a few micromolars). Higher binding affinities cannot be accurately measured due to instrumental limitations. More specifically, in order to resolve the initial phase of a binding curve, we need to measure cells expressing FRET constructs at the level of the binding affinity or lower. The averages radius of HEK293 cells was measured as 7.7 μm[49], from which we can estimate that the average cell volume is about 2 picoliter. Thus, to reach 1 nM expression level of a construct, we need cells expressing only ~1000 fluorescent proteins, and in our FRET experiment, the excitation power is low enough that only a small percentage of fluorophores are excited at a time (see supplementary materials of Erikson *et al.*, 2001[14]). In other words, we need to accurately measure signals from tens of fluorescent proteins, which is very difficult. However, in such case, we can at least tell the protein interaction occurs with a very high binding affinity by FRET two-hybrid, even though we cannot give very accurate measurement of the binding affinity. So this limitation is not a big problem. On the other hand, lower binding affinities cannot be detected as the cellular machinery usually can only produce exogenous proteins up to a few micromolars. Also, very high expression levels make cells sick or cause aggregation of fluorescent proteins, rendering FRET assays inapplicable. As described previously, these low affinity binding interactions can be of significant functional importance. Of note, yeast two hybrid[63], another popular live-cell binding assay, allows for the detection of weak protein interactions between transcription factors, as its readout tends to be amplified through cascade reactions. To make FRET two-hybrid also feasible to detect weak interactions, we can use weak helpers to create divalent binding, which results in higher binding affinities suitable for measurement by FRET two-hybrid assays. The strategy of using divalent binding to generate high affinity interactions is employed by the nature, for example in the function of antibodies[64]. Models of divalent binding have been extensively studied[65,66]. Here, by choosing weak helpers with binding affinities within a favorable range, we can use a simplified model to estimate the binding affinity of the target protein interaction from the measured divalent binding affinity. One caveat here is that the effective local concentration of weak helper in the protein complex is needed for estimating the binding affinity. In this case, we assume the concentration is about 500μM as we expect the protein complex is relatively small. However, this method could be further improved by developing a good way to measure this value for various protein interactions of interest.

It has been a field-wide challenge to find small molecule compounds that disrupt specific protein interactions[67,68]. While *in vitro* high-throughput screening (HTS) for inhibitors is more straightforward[69], it tends to produce false-positive results because of lack of cell context[70]. Hits might only inhibit the protein interaction in the highly artificial *in vitro* environment or may not pass through the membrane so they cannot affect intracellular protein interactions. That said, our proposed live-cell FRET-based assay represents a novel approach, one that concurrently screens for membrane permeability and disruption of binding. It has several advantages over the previously developed cell-based protein fragment complementary assays such as yeast/mammalian two-hybrid[71] or biomolecular-fluorescence-complementation (BiFC)[72] based assays. First, unlike many fragment complementary reaction assays, FRET is reversible and thus more suitable for detecting inhibitors of protein interactions. Second, FRET is ratiometric, and the values obtained do not rely on absolute readings and thus have lower inter-well variation. However, it is often thought that cell-based FRET two-hybrid assays are not suitable for HTS due to a small signal to noise ratio[73]. On one hand, the FRET signal is weak and can be mixed with crosstalk due to direct fluorescence, and thus requires careful calibration. On the other hand, it could be challenging and time consuming to design optimal FRET constructs. While unimolecular FRET sensors seems to be attractive, they are hard to design and optimize. Moreover, it is hard to predict how much FRET reduction can be caused by inhibitors, especially if partially disrupted by weak inhibitors. Bimolecular FRET, on the other hand, might enjoy better signal to noise ratio as disruption of binding leads to no FRET. The challenge of bimolecular FRET is to have the two binding partners expressed at the desired level in all cells. It turns out that by using lentivirus, we can reach the desired expression level much more precisely than by using the traditional resistant selection. The stable cell lines produced by lentivirus can maintain fairly homogenous expression levels at the population level for several months. In this study, we manually selected single colonies to form stable cell lines. In the future, flow cytometry can be used to expedite this process. Of note, however, lentivirus has potential recombination issues[60], and the expression level of stable cell lines can degrade after a few freeze and thaw cycles or repeated passaging.

One potential issue in the use of FRET-based HTS assays are the artificial FRET changes due to either autofluorescence of the small molecule, or direct effects on the fluorophores (**Figure 14C**). This problem can be largely solved by using couterscreens on cell lines expressing Cerulean-Venus dimers. In summary, our FRET-based HTS assay provides an inexpensive venue with which to detect inhibitors of protein interactions in the cellular context, without the need to purify proteins.

Figures

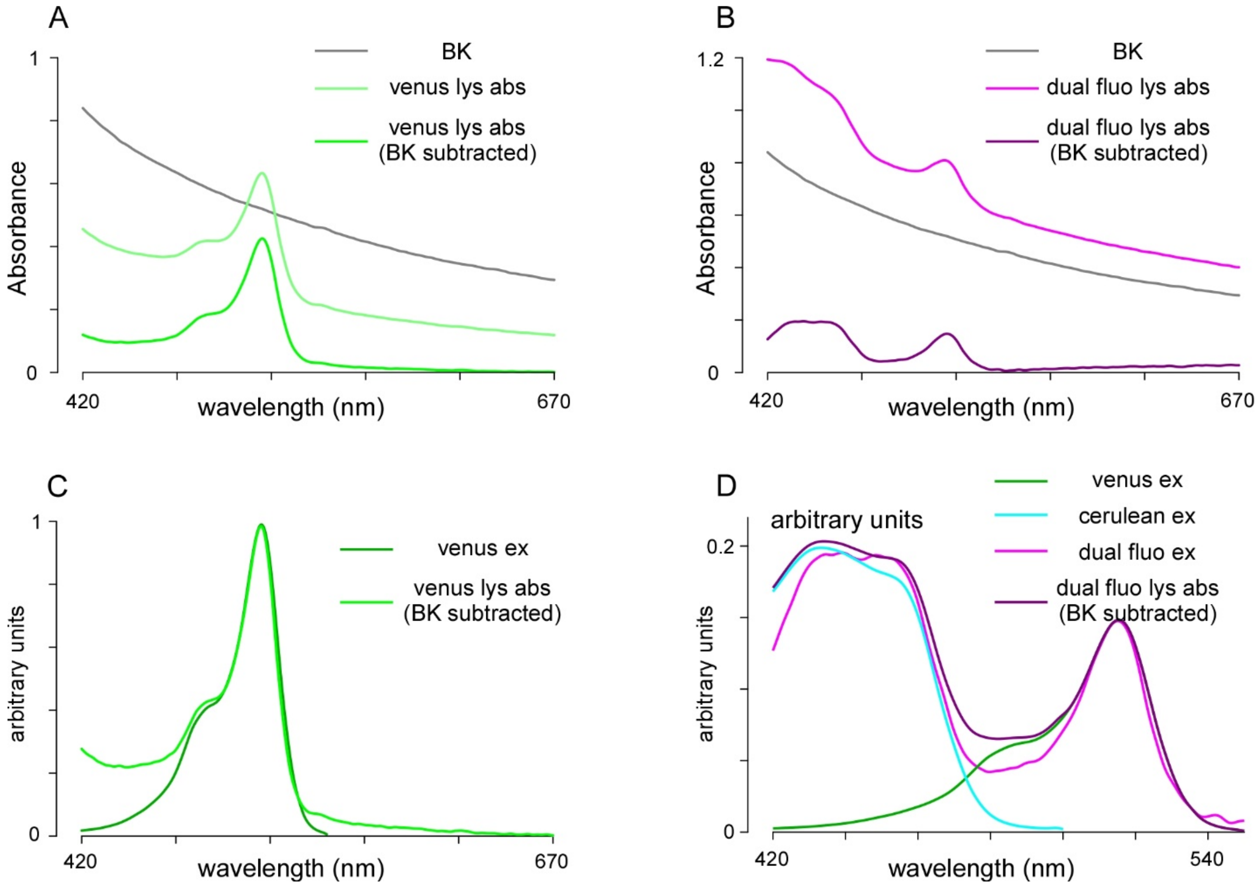
A
1
0
Absorbance
420
wavelength (nm)
670
BK
venus lys abs
venus lys abs (BK subtracted)
B
1.2
0
Absorbance
420
wavelength (nm)
670
BK
dual fluo lys abs
dual fluo lys abs (BK subtracted)
C
1
0
arbitrary units
420
wavelength (nm)
670
venus ex
venus lys abs (BK subtracted)
D
arbitrary units
0.2
0
arbitrary units
420
wavelength (nm)
540
venus ex
cerulean ex
dual fluo ex
dual fluo lys abs (BK subtracted)

Figure 8. **Using absorption spectrum to determine fluorescent protein concentration.** (**A**) Absorption spectrum of lysate from cells that do not express fluorescent proteins (background, gray trace) and cells expressing Venus-PreIQ$_3$-IQ-A$_{1.3}$ peptide (Venus lysate, light green trace). Subtracting the spectrum of background (after scaling by a constant value) from that of Venus lysate gave the spectrum shown in green. (**B**) Absorption spectrum of lysate from background (gray trace) and cells expressing Venus-PreIQ$_3$-IQ-A$_{1.3}$ peptide and Cerulean-ICDI$_{1.4}$ peptide (dual-fluorophores lysate, light purple trace). Subtracting background from dual-fluorophore lysate gave the spectrum shown in dark purple. (**C**) Overlay of absorption spectrum of Venus lysate (green trace, background subtracted, same as in **A**) with excitation spectrum of Venus (dark green trace). Both spectrum were scaled. (**D**) Overlay of absorption spectrum of dual-fluorophore lysate (dark purple, background subtracted, same as in B) with excitation spectrum of Venus (dark green trace), Cerulean (cyan trace) and the addition of the two (light purple trace). The excitation spectrum were scaled to match the peak of absorption spectrum.

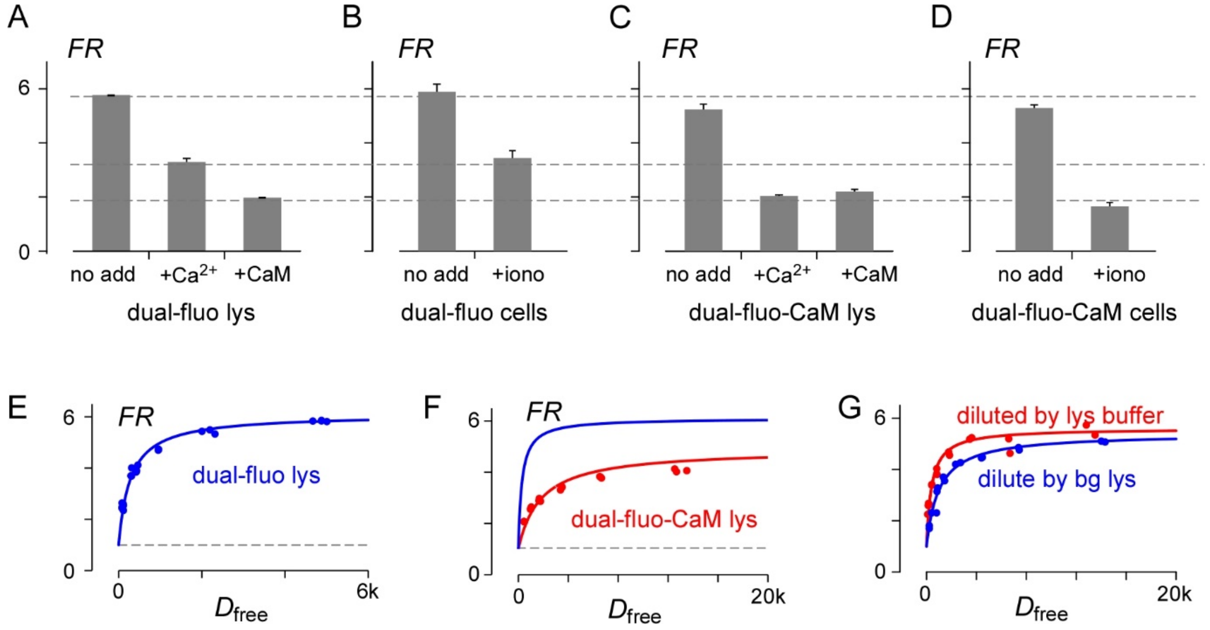
A
B
C
D
FR
6
0
no add
+Ca2+
+CaM
dual-fluo lys
no add
+iono
dual-fluo cells
no add
+Ca2+
+CaM
dual-fluo-CaM lys
no add
+iono
dual-fluo-CaM cells
E
FR
dual-fluo lys
6k
Dfree
F
FR
dual-fluo-CaM lys
20k
Dfree
G
diluted by lys buffer
dilute by bg lys
20k
Dfree

Figure 9. Using lysate FRET to determine binding affinity of IQ/ICDI interaction.

(**A**) Lysate of cells expressing Venus-PreIQ$_3$-IQ-A$_{1.3}$ peptide and Cerulean-ICDI$_{1.4}$ peptide (dual-fluorophore lysate) shows high FR (no add), reduced FR when Ca^{2+} is added (+Ca^{2+}) and further reduced FR when purified CaM protein added (+CaM). (**B**) Cells expressing Venus-PreIQ$_3$-IQ-A$_{1.3}$ peptide and Cerulean-ICDI$_{1.4}$ peptide (dual-fluorophore cells) shows high FR (no add) and reduced FR (+iono) when internal Ca^{2+} is elevated by adding ionomycin. (**C**) Lysate of cells expressing Venus-PreIQ$_3$-IQ-A$_{1.3}$ peptide and Cerulean-ICDI$_{1.4}$ peptide and overexpressing CaM (dual-fluorophore-CaM lysate) shows high FR (no add), largely reduced FR when Ca^{2+} is added (+Ca^{2+}) and no further reduced FR when purified CaM protein added (+CaM). (**D**) Cells expressing Venus-PreIQ$_3$-IQ-A$_{1.3}$ peptide and Cerulean-ICDI$_{1.4}$ peptide and overexpressing CaM (dual-fluorophore-CaM cells) shows high FR (no add) and largely reduced FR (+iono) when internal Ca^{2+} is elevated by adding ionomycin. (**E**) Two-hybrid FRET assay on dual-fluorophore lysate. Fluorescent lysate was diluted by lysate from background cells (background lysate) to obtain lower left points on the curve. (**F**) Two-hybrid FRET assay on dual-fluorophore-CaM lysate (red). Similar as **C**, fluorescent lysate was diluted by background lysate to obtain lower left points on the curve. The blue curve are the same curve in C**.** (**G**) Two-hybrid FRET assay on dual-fluorophore lysate. The lower left points on the curve were obtained by diluting the dual-fluorophore lysate with background lysate (blue) or lysis buffer (red). The blue trace is different from the blue trace in **E** and **F** is because this experiment was performed on a different day, but binding affinity measured using blue curve are very similar.

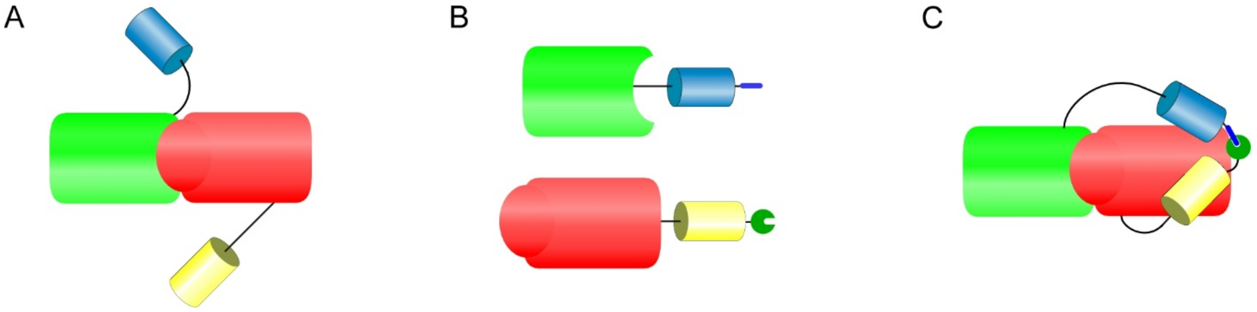

Figure 10. Cartoon of weak helper improving FRET.

(**A**) Fluorophores (blue and yellow barrels) are separated by the complex formed by interaction between the two peptides (red and green complementary shapes). Such configuration results in low FRET. (**B, C**) Weak helpers (dark green nicked circle and blue bar) were attached to fluorophores. These weak helpers are low affinity binding partners which only binds when the peptides of interest (read and green complementary shapes) binds and bring them close to each other. Binding of weak helpers (**C**) restrains the free movement of fluorophores and results in high FRET.

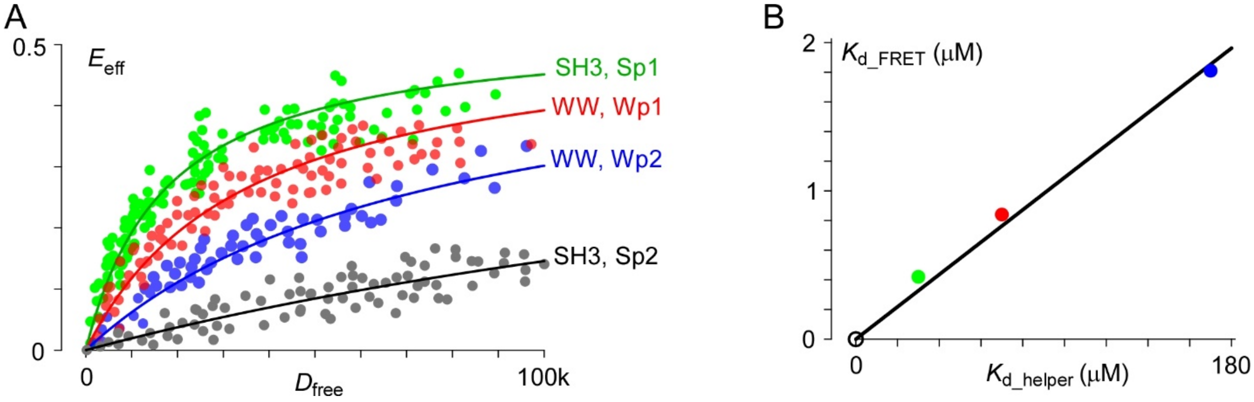

Figure 11. Divalent FRET binding assay of IQ and ICDI interaction using weak helpers.

(**A**) Interaction of IQ and ICDI peptides measured by divalent FRET two-hybrid binding assays utilizing weak helpers. The design of constructs can be represented by cartoon in Fig. **10B**, where the red shape is $IQ_{1.3}$ and the green shape is $ICDI_{1.4}$. Four pairs of weak helpers were tested, SH3 domain and its binding peptides Sp1 or Sp2, WW domain and its binding peptides Wp1 or Wp2. (**B**) Correlation between binding affinity measured by FRET two-hybrid assay and the affinity of weak helper pairs. Color scheme is the same as in **A**. The binding affinity of SH3/Sp1, WW/Wp1, WW/Wp2 were measured as 30, 50, 170 μM[51], but here 70 μM is used as binding affinity of WW/Wp1 instead of 50 μM as it fits better for both IQ/ICDI and A/ICDI experiments. The binding affinity measured by FRET two-hybrid assay employing SH3/Sp1, WW/Wp1, WW/Wp2 as weak helpers are 0.42, 0.84, 1.81μM. The binding affinity of SH3/Sp2 is not known but estimated as > 1000 μM[51], so its data is not included on this plot. The black line is a linear fit with the slope of 0.0109. Theoretically the fit should pass the zero point (open black circle).

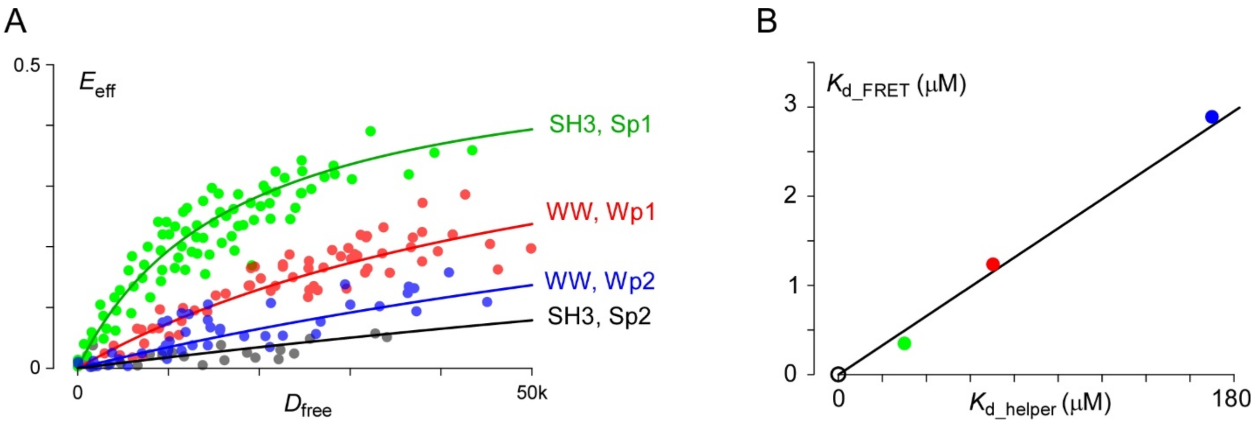

Figure 12. Divalent FRET binding assay of IQ and A interaction using weak helpers.

(**A**) Interaction of A and ICDI peptides measured by divalent FRET two-hybrid binding assays utilizing weak helpers. The design of constructs can be represented by cartoon in Fig. **10B**, where the red shape is $A_{1.3}$ and the green shape is $ICDI_{1.4}$. Four pairs of weak helpers were tested, SH3 domain and its binding peptides Sp1 or Sp2, WW domain and its binding peptides Wp1 or Wp2. (**B**) Correlation between binding affinity measured by FRET two-hybrid assay and the affinity of weak helper pairs. Color scheme is the same as in **A**. The binding affinity of SH3/Sp1, WW/Wp1, WW/Wp2 were measured as 30, 50, 170 μM[51], but here 70 μM is used as binding affinity of WW/Wp1 instead of 50 μM as it fits better for both IQ/ICDI and A/ICDI experiments. The binding affinity measured by FRET two-hybrid assay employing SH3/Sp1, WW/Wp1, WW/Wp2 as weak helpers are 0.35, 1.24, 2.89μM. The binding affinity of SH3/Sp2 is not known but estimated as > 1000 μM[51], so its data is not included on this plot. The black line is a linear fit with the slope of 0.017. Theoretically the fit should pass the zero point (open black circle).

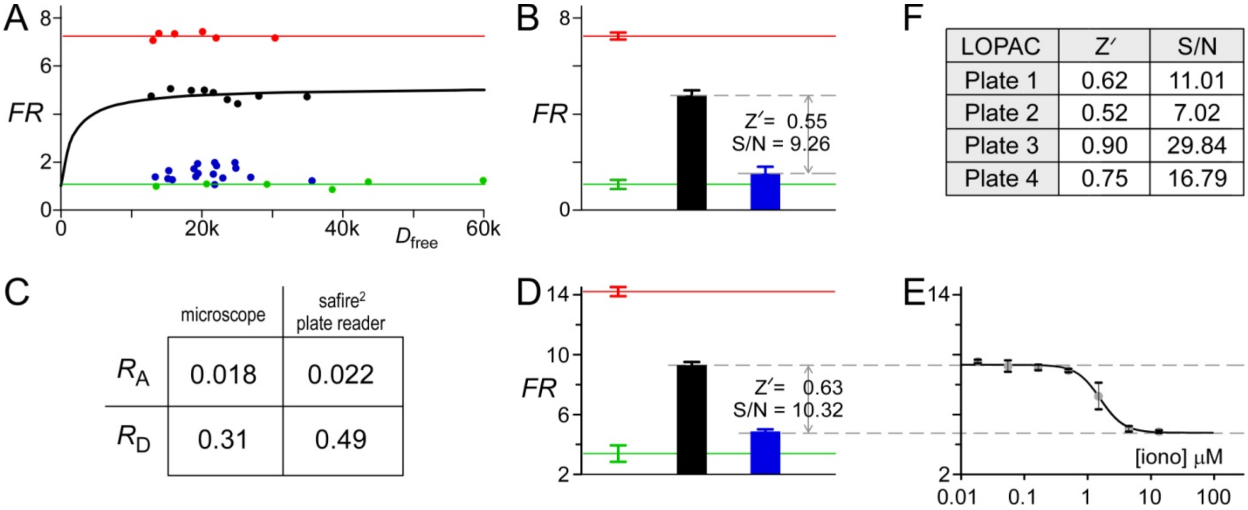

	microscope	safire^2 plate reader
R_A	0.018	0.022
R_D	0.31	0.49

LOPAC	Z′	S/N
Plate 1	0.62	11.01
Plate 2	0.52	7.02
Plate 3	0.90	29.84
Plate 4	0.75	16.79

Figure 13. Translating FRET binding assay from microscope-based to plate-reader format.

(**A**) Microscope-based assay of constructs expressed in stable cell lines. Each symbol corresponds to a single stable cell expressing constructs given by the following color code: red, Cerulean-Venus dimer; black, Venus-PreIQ$_3$-IQ-A$_{1.3}$ and Cerulean-ICDI$_{1.4}$; blue, Venus-PreIQ$_3$-IQ-A$_{1.3}$, Cerulean-ICDI$_{1.4}$, CaM in presence of ionomycin; green, Cerulean and Venus expressed as separate molecules. (**B**) Mean values of cells in **A**, along with z and S/N ratio. Same color code. (**C**) FRET conversion parameters on microscope and safire^2 plate reader. (**D**) Plate-reader results, each group averaged from 3 wells. Color code as in **B**. (**E**) Titration of ionomycin on ‘blue-type cells’ in **B**, measured on safire^2 plate reader. (**F**) Statistics for experiment in **D**, repeated in four additional plates, each averaging 3 wells.

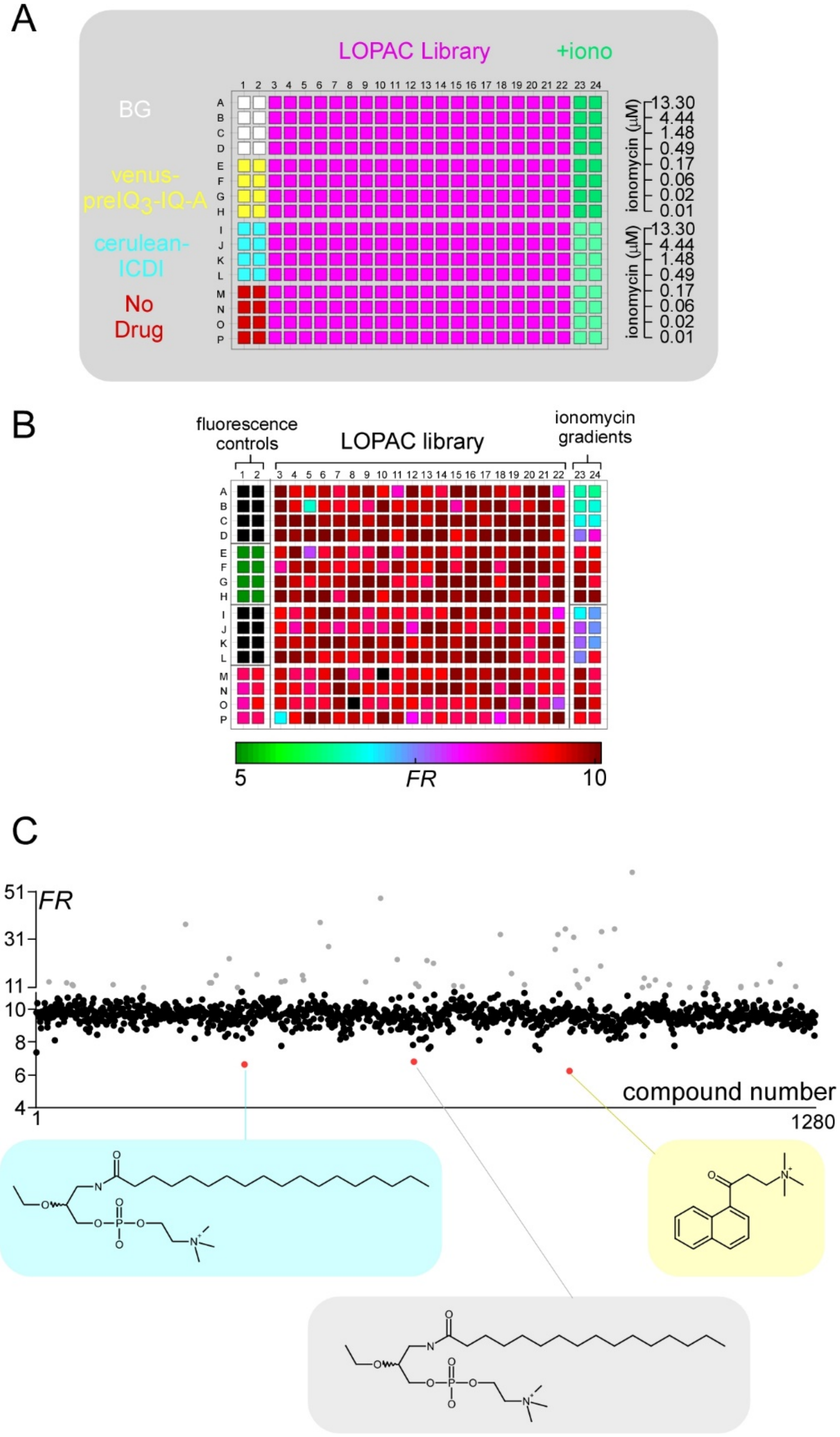
A
LOPAC Library
+iono
BG
venus-preIQ$_3$-IQ-A
cerulean-ICDI
No Drug
1 2 3 4 5 6 7 8 9 10 11 12 13 14 15 16 17 18 19 20 21 22 23 24
A B C D E F G H I J K L M N O P
ionomycin (μM)
13.30
4.44
1.48
0.49
0.17
0.06
0.02
0.01
B
fluorescence controls
LOPAC library
ionomycin gradients
5
FR
10
C
FR
51
31
11
10
8
6
4
1
1280
compound number
O
N
O
P
N+

Figure 14. Provisional 1280-compound LOPAC library screen.

(**A**) Results, single multi-well plate, in heatmap format (FRET metric *FR* color-coded as shown at bottom). Columns 3-22 show IQ/ICDI interactions subject to various compounds at 25 μM. olumns 1-2; A-D, background cells; E-H, cells with Venus; I-L, cells with Cerulean; CM-P, cells with ICDI/IQ and no drug. Columns 23-24: A-H, ICDI/IQ cells with ionomycin gradient (13, 4.4, 1.5, .5, .2, .06, .02, .01 μM, respectively; I-P, same as A-H minus CaM. (**B**) Linear graphical display of results for 1280-compound LOPAC screen. Histogram at right indicates tight distribution of most of the wells around a FRET readout value of ~10 (green dash line). Red dashed line shows mean – 3.5x standard deviations, which correspondence to threshold for marking 'hits,' as exemplified by 3 red symbols. Affiliated compound structures are shown below. Some compounds increased apparent FRET values, as shown by gray symbols. We believe these to reflect spurious compound fluorescence, rather than a genuine enhanced ICDI/IQ interaction. Note axis break and change of scale along *y*-axis.

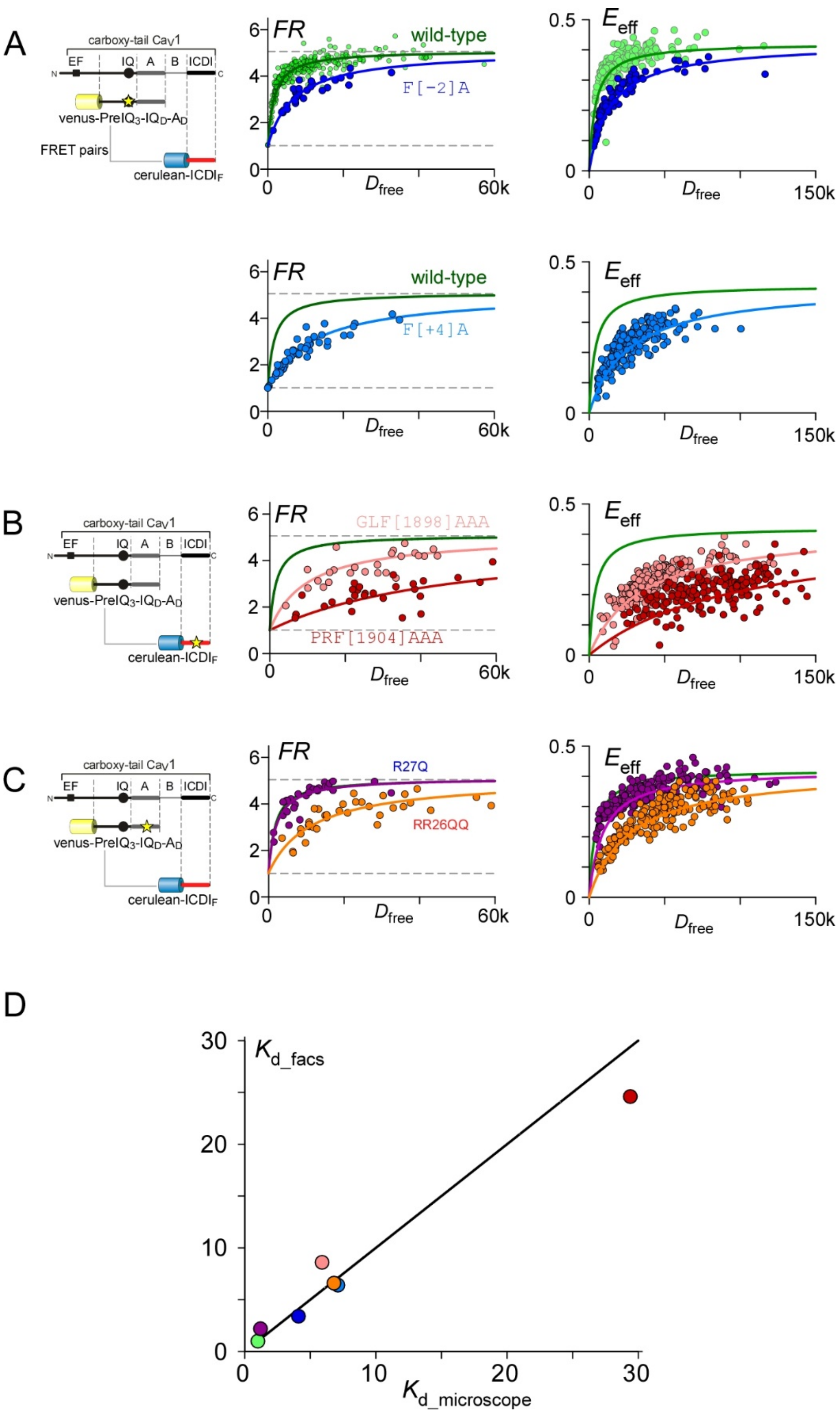
A
carboxy-tail CaV1
EF
IQ
A
B
ICDI
N
C
venus-PreIQ3-IQD-AD
FRET pairs
cerulean-ICDIF
FR
wild-type
F[-2]A
Dfree
0
60k
6
4
2
0
Eeff
0.5
0
150k
F[+4]A
B
GLF[1898]AAA
PRF[1904]AAA
C
R27Q
RR26QQ
D
Kd_facs
Kd_microscope
30
20
10
0

Figure 15. Comparison of 3-cube FRET binding assay on microscope and flow cytometer.

(**A, B, C**) FRET two-hybrid assays were performed for interaction between Venus-PreIQ$_3$-IQ-A$_{1.3}$ peptide and Cerulean-ICDI$_{1.4}$ peptide on microscope (middle column, **A, B, C**) and flow cytometer (right column, **A, B, C**). In addition to wide-type peptides, hotspot on IQ region (**A**), ICDI region (**B**) and A region (**C**), indicating by the start on the cartoons (left column, **A, B, C**), are tested. (**D**) Relationship of normalized dissociation constants measured on microscope ($K_{\mathrm{d\_microscope}}$) and those measured on flow cytometer ($K_{\mathrm{d\_facs}}$). The color scheme is the same of in **A, B, C**. Dissociation constant of wild-type peptides measured for each method was used for normalization (i.e., the green dot has both $K_{\mathrm{d\_microscope}}$ and $K_{\mathrm{d\_facs}}$ equals to 1).

Chapter 3

PKA modulation of $Ca_V1.4$ calcium channels

Introduction

Phosphorylation, as one of the most ubiquitous forms of post-translational modification, plays essential roles in biological functions[74]. Traditionally, phosphorylation sites were identified by phosphopeptide mapping and Edman degradation sequencing[75]. With the recent progress of mass spectroscopy based proteomics, numerous potential phosphorylation sites can now be identified[76,77]. However, establishing the biological relevance and underlying molecular pathway of these phosphorylation sites remains difficult[78], especially for large membrane proteins such as voltage gated ion channels. In particular, the regulation of L-type Ca^{2+} channels by PKA, though biologically crucial, has long remained mechanistically storied and complex[78-80]. While native cells feature full-bore PKA regulation of L-type Ca^{2+} channels, it has been difficult to dissect out the critical factors of this regulation among the vast array of native molecules[81]. On the other hand, *in vitro* biochemistry can sometimes identify sites that do not correlate with function[76]. The use of a recombinant system such as HEK293 cells has therefore become a valuable method for characterizing phosphorylation pathways and elucidating the functional relevance of potential phosphorylation sites[77,82]. Unfortunately, such a model system for studying the PKA modulation of L-type Ca^{2+} channels has remained challenging as even the strong PKA enhancement of cardiac Cav1.2 L-type Ca^{2+} channels cannot be fully reconstituted in heterologous systems[78,80,83].

Here, we adopt a different tactic and utilize ideas drawn from synthetic biology and live-cell biochemistry to engineer a form of PKA modulation of L-type channels. Our strategy is based on perturbing the calmodulation of L-type Ca^{2+} channels[84]. Calmodulin (CaM) is known to associate with the IQ domain of the channel carboxy terminus while in the Ca^{2+} free (apo) state[14,22]. The presence of apoCaM on the channel IQ significantly increases channel open probability (P_O) as compared to the channel in the absence of apoCaM[6] (**Figure 1A**). In addition, the presence of apoCaM enables Ca^{2+}/CaM dependent inactivation (CDI), whereby Ca^{2+} binding to the resident CaM results in a decrease in channel P_O[22]. This effect can readily be seen in whole cell experiments where channels bereft of CaM exhibit diminutive but sustained currents, while channels populated by CaM have significantly larger peak current amplitudes and robust CDI.

Several L-type channel splice variants exploit this calmodulation effect in order to tune the biophysical properties of channels expressed in different cell types[34,85,86]. In particular, long splice variants of Cav1.3 and 1.4 channels contain a CDI-inhibiting module (ICDI) within their distal carboxyl terminus (DCT) which competes with apoCaM for binding at the IQ domain[8,9]. By dislodging CaM, ICDI profoundly suppresses the channel open probability and eliminates CDI. We reasoned that a phosphorylation site in ICDI might weaken it's affinity for the IQ domain in a PKA-sensitive manner, allowing channels to rebind CaM and thus undergo an increase in current amplitude and CDI.

We therefore explored if such a PKA phosphorylation site might exist natively within the ICDI domain via a live-cell FRET two-hybrid assay in adult guinea pig ventricular myocytes (aGPVMs). Remarkably, we found that the IQ interaction with the wild-type ICDI of L-type Cav1.4 channels ($ICDI_{1.4}$) is sharply attenuated by PKA activation, whereas ICDI modules from other L-type channel isoforms (Cav1.2 and 1.3) showed no such modulation. Accordingly, we synthesized chimeric Cav1.3 channels fused to $\mathrm{ICDI}_{1.4}$, and endowed these channels with robust forskolin-dependent enhancement of open probability and CDI, observable in HEK293 cells. The modularity of this synthetic PKA regulation of L-type Ca^{2+} channels was further demonstrated by strong PKA regulation of Cav1.2 channels with $\mathrm{ICDI}_{1.4}$ co-expressed as a peptide. Finally, we demonstrated that PKA can modulate the current amplitude and CDI of wild-type Cav1.4 channels in HEK293 cells and identified S1883 as the phosphorylation site within Cav1.4 via mass spectroscopy and site directed mutagenesis. In all, PKA modulation of Cav1.4 Ca^{2+} channels, discovered through a synthetic live-cell biochemical approach, might be an important regulatory mechanism utilized by Cav1.4 channels, enabling precise tuning of Ca^{2+} influx in various physiological conditions.

Methods

Molecular biology. The Cav1.3 channel (in pcDNA6) was derived from the rat brain variant (AF307009.1)[20]. Cav1.2 (in pGW) is identical to rabbit NM001136522[21], and Cav1.4 (in pCDNA3) is the human clone corresponding to NM00718[6]. $\mathrm{Cav1.3}_{\mathrm{S/1.4DCT}}$ (in pcDNA6) was made by fusing with the DCT of Cav1.4 to the Cav1.3 channel backbone (truncated after the IQ domain), as previously described[8]. To generate the point mutation (S1883A) in the $\mathrm{Cav1.3}_{\mathrm{S/1.4DCT}}$ chimeric channel, the mutation was first introduced within the Cav1.4 distal carboxy tail peptide by QuickChange mutagenesis

(Agilent) before PCR amplification and insertion into the Cav1.3 channel backbone, using the same strategy as the wild-type Cav1.3$_{S/1.4DCT}$ chimeric channel. β_{2a}-Gly$_8$-CaM (in pcDNA3) was made as described before[42], and used in experiments for **Figure 27**; β_{2a}-Gly32-CaM was made by extending the number of glycine residues in the linker from 8 to 32, using similar strategies as described before[5], and used in experiments for **Figure 24**; β_{1b}-Gly32-CaM was made by swapping β_{2a} (M80545)[87] with β_{1b} (NM_017346.1)[88] via KpnI and NotI sites, and used in experiments for **Figure 25**.

FRET constructs were fluorescent-tagged (either Venus or Cerulean) using similar strategies as previously described[14]. Briefly, Venus and Cerulean fluorophores (a kind gift from Dr. Steven Vogel at NIH) were subcloned into pcDNA3 via unique *Kpn*I and *Not*I sites. The PCR-amplified channel peptides as described in Liu *et. al.*[8] were then cloned in via unique *Not*I and *Xba*I sites. The fluorescent-tagged peptides were PCR-amplified as a whole and cloned into pAdLox via *Kpn*I and *EcoR*I.

In order to make the Venus-PKAca-P2A-PKAr2b-Cerulean construct, Cerulean was PCR amplified and cloned into pcDNA3 via *Xba*I/*Apa*I, and then PKAr2b (Addgene: pDONR223-PRKAr2b) was PCR amplified (the P2A sequence, FQGPGATNFSLLKQAGDVEENPGPSLSK, was fused 5’ of PRAr2b by this PCR amplification) and cloned via *Not*I/*Xba*I. PKAca (Addgene: pDONR223-PRKACA) was first cloned into Venus-C1 (made by replacing EGFP by Venus in pEGFP-C1) as described[49]. The Venus-PKAca was then PCR amplified and cloned into pcDNA3 containing P2A-PKAr2b-Cerulean via *Kpn*I/*Not*I. The PKAca-P2A-PKAr2b (no fluorescent tag) was PCR amplified using Venus-PKAca-P2A-PKAr2b-Cerulean as a template and inserted into pcDNA3 via *Kpn*I and *Xba*I.

Adenovirus production. Adenoviral vectors were generated using the Cre-Lox recombination system as previously described[1]. Briefly, pAdLox plasmids encoding the FRET binding partners were co-transfected with $\Psi5$ vector into Cre8 cells, allowing expression and packaging of the viral particles. After three-rounds of expansion in Cre8 cells, a final viral amplification was done in HEK293 cells. The viral particles were collected and purified by a standard CsCl gradient protocol. The purified viral stock had a titer of at least 10^{12} particles/μl.

aGPVM culture and infection. Adult guinea pig ventricular myocytes (aGPVMs) were isolated as described[48,76] and plated on laminin-coated glass coverslips in M199 media containing 20% fetal bovine serum (FBS). After 1 hour, media was exchanged with 0% FBS M199 media and adenoviruses encoding FRET binding partners were added. 8 to 12 hours later, the myocytes were washed once with warmed PBS, and the media was replaced with fresh 0% FBS media. aGPVMs were imaged within 24 hours of isolation.

Transfection of HEK293 cells. For electrophysiology experiments, HEK293 cells were cultured on 10-cm plates, and channels were transiently transfected by a calcium phosphate protocol[22]. We applied 4-16 μg of plasmid DNA encoding the desired α_1 subunit, as well as 6-8 μg of β and 5-8 μg of rat $\alpha_2\delta$ (NM012919.2)[23] subunits along with 3 μg of SV40 T antigen. For forskolin incubation experiments, β_{2a} without a glycine linked CaM was used. In addition, 4 μg Venus-PKAca-P2A-PKAr2B-Cerulean and 1 μg

PKAr2b-Cerulean were co-transfected. For dynamic forskolin wash-on experiments, a β subunit (β_{2a} for Cav1.3 and 1.4; β_{1b} for Cav1.2) with glycine linked CaM was used. In addition, 4 μg Venus-PKAca-P2A-PKAr2b-Cerulean, 1 μg PKAr2b-Cerulean and 3 μg AKAP79 (M90359.1) were co-transfected. Generally, β_{2a} was chosen to minimize the confounding effects of VDI, thus maximizing the dynamic range of CDI. For Cav1.2 channels, β_{1b} was used in order to closely recapitulate the behavior of the native Cav1.2 channel expressed in cardiac cells. By decreasing the dynamic range of observable CDI, this perturbation also increased the stringency of the test and allowed for comparison with native PKA modulation of Cav1.2 channels (**Figure 26**).

For microscope-based FRET assays, HEK293 cells cultured on 3.5-cm culture dishes with integral No. 0 glass coverslip bottoms (In Vitro Scientific) were transiently transfected with polyethylenimine (PEI) reagent (Polysciences). For flow-cytometer-based FRET assays, HEK293T cells cultured on 6-well plates were transiently transfected with PEI. All of constructs were driven by a cytomegalovirus promoter. Experiments were performed 1-2 days following transfection.

Whole-cell electrophysiology recording. Whole-cell recordings were obtained at either room temperature or 30°C as described using a TC-10 heating & cooling temperature controller (Dagon Corporation) and Axopatch 200A amplifier (Axon Instruments). Electrodes were pulled from borosilicate glass capillaries (Word Precision Instruments), with 1-3 MΩ resistances, which were in turn compensated for series resistance by >60%. Currents were low-pass filtered at 2 kHz before digital acquisition at five times the frequency. A P/8 leak-subtraction protocol was used. The internal solution contained (in mM): $CsMeSO_3$, 114; CsCl, 5; MgATP, 4; HEPES (pH 7.4), 10; and BAPTA (1,2-bis(*o*-aminophenoxy)ethane- *N*,*N*,*N'*,*N'*-tetraacetic acid), 10; at 295 mOsm adjusted with $CsMeSO_3$. The bath solution was (in mM): TEA-$MeSO_3$, 102; HEPES (pH 7.4), 10; $CaCl_2$ or $BaCl_2$, 40; at 305 mOsm adjusted with TEA-$MeSO_3$.

Microscope-based FRET optical imaging. FRET two-hybrid experiments were performed on an inverted microscope as described[7,14]. The bath Tyrode's solution was (in mM): NaCl, 138; KCl, 4; $MgCl_2$, 1; HEPES (pH 7.4), 10; $CaCl_2$, 2; at 305mOsm adjusted with glucose. Background fluorescent signals were measured from cells without expression of the fluorophores, which was particularly important for experiments in aGPVMs due to higher autofluorescence. In Hek cells, concentration-dependent spurious FRET was subtracted from the raw data prior to binding-curve analysis[7,14]. Cerulean and Venus were used as the donor and acceptor fluorescent proteins instead of ECFP and EYFP, as their optical properties are better for this application. Acceptor-centric measurements of FRET were obtained with the 3^3-FRET algorithm[7,14], which expresses the effective FRET efficiency (E_{EFF}) and FRET ratio (FR) as:

$$E_{\mathrm{EFF}} = E \times A_{\mathrm{b}} = (FR - 1)[\varepsilon_{\mathrm{ven}}(440nm)/\varepsilon_{\mathrm{cer}}(440nm)]$$

where $E = k_{\mathrm{T}}/(k_{\mathrm{T}} + k_{\mathrm{D}})$ is the FRET efficiency of a donor-acceptor pair, A_{b} is the fraction of acceptor molecules bound by a donor. $\varepsilon_{\mathrm{ven}}(440nm)/\varepsilon_{\mathrm{cer}}(440nm)$ is the approximate molar extinction coefficients of Cerulean and Venus, which was measured as 0.08 on our setup.

Flow-cytometer-based FRET optical imaging. FRET two-hybrid experiments were performed on an Attune Acoustic Focusing Cytometer (Life Technologies) as described[49]. Cells were trypsinized and resuspended in Tyrode's solution before loading onto the flow cytometer. The previously described algorithm[7,14] was used to calculate acceptor-centric measures. In total, signals from 1,000-10,000 cells were recorded, however only 30-50 randomly selected cells were displayed in order to improve clarity of the figure.

Mass spectroscopy. Double Histidine (His_8) tagged Cerulean-$ICDI_{1.4}$ peptides were co-transfected with PKA holoenzyme in HEK293T cells. Cells were incubated in 50 µM forskolin in a 37°C incubator for 1 hour before collecting with a lysis buffer, containing (in mM): KCl, 20; K-gluconate, 120; $MgCl_2$, 2; EGTA, 0.2; HEPES (pH 7.4); Na_2-ATP; 2; DTT, 10; cAMP, 0.1. Protease inhibitor cocktail (Roche, complete, EGTA-free), phosphatase inhibitor cocktail 2 and 3 (Sigma-Aldrich) were added into the lysis buffer according to the standard protocol. His-tagged Cerulean-$ICDI_{1.4}$ peptides were purified by Ni-NTA agarose (QIAGEN) and verified by SDS-PAGE using mini-PROTEAN precast gel (Bio-Rad). The band containing the $ICDI_{1.4}$ peptide (**Figure 30A**) was cut from the gel then sent to the Johns Hopkins Mass Spectroscopy and Proteomics Facility, where the peptides were in-gel proteolyzed with trypsin and analyzed on nano-LC ESI/MS/MS Orbi-trap Velos in FTFT mode. Tandem MS2 mass spectra were processed by Proteome Discoverer (v1.4 Thermo Fisher Scientific) in three ways, using 3 Nodes: common, Xtract (spectra are extracted, charge state deconvoluted, and deisotoped using Xtract option), MS2 Processor. The tandem mass spectra were searched against the RefSeq2014 Human database filtered at a 1% FDR using PEAKS 7.0 (Bioinformatics Solutions Inc). Variable modifications by M oxidation, NQ deamidation, and STY phosphorylation were searched for with a precursor ion tolerance of 10 ppm and a fragment ion tolerance of 0.02 daltons.

Two peptides (peptide 1: GSADSLVEAVLISEGLGLFAR and peptide 2: LTLDEMDNAASDLLAQGTSSLYSDEESILSR) from $Ca_V1.4$ were identified, which covered 52% of the total 100 amino acids in $ICDI_{1.4}$ (**Figure 29**) and 11 of the 14 potential phosphorylation sites in this region. Three potential sites, T1872, S1874, and S1877, were not covered due to the limitation of trypsin, but they are not in the core region for IQ interaction[89]. Peptide 1 was identified nine times, among which it carried a phosphate group six times. The peaks from double and triple charged peptides detected in the first MS showed a molecular weight that was 79.97 daltons higher than that expected without a phosphate group, verifying phosphorylation. The data predicted that either S1883 or S1886 could be the site of phosphorylation. However the existence of b_4, b_4(-98) and y_{17} in the spectra in (**Figure 31A** and **Figure 30B**) strongly suggested that the phosphorylation site is S1883. In addition, pkaPS predictions and mutagenesis (**Figure 31D, E** and **Figure 29C, D**) strongly support that the PKA phosphorylation site is S1883. Peptide 2 was identified twelve times, and carried a phosphate group at S1942 in only one trial. This potential phosphorylation site, however, did not have any effect on the interaction between $IQ_{1.3}$ and $ICDI_{1.4}$ in our FRET binding assay (**Figure 29C, D**).

Results

The interaction between IQ and ICDI domains regulated by PKA in aGPVMs

The ICDI domain in certain L-type Ca^{2+} channels is known to bind to the IQ region of the channel, displacing CaM and reducing the CDI and P_O of the channel[6,8]. Given the functional importance of this IQ/ICDI binding, we sought to assess if this interaction might be modulated by PKA phosphorylation. To this end, we utilized a live-cell FRET two hybrid assay, pairing Venus-tagged IQ domains against Cerulean-tagged ICDI domains from various L-type Ca^{2+} channels. Although not required for CaM binding[40], the downstream A-region[8,90] was included within our IQ construct (IQ-A) as it contributes to the binding between the IQ and ICDI domains (Chapter 1)[89]. Cognizant that full-bore PKA signaling is best conserved within certain native rather than model cells[79,91], we performed the FRET assays in aGPVMs, which are renowned for their strong PKA signaling. The FRET pairs were transduced into aGPVMs via adenoviral vectors, allowing rapid and tunable expression within acute (one day) myocytes[48] (**Figure 16A, B**).

There are three L-type calcium channels of interest, Cav1.2, Cav1.3 and Cav1.4, and FRET binding curves were constructed for the mix and match of their IQ-A and ICDI peptides (**Figure 16C**). We began by pairing the IQ-A module from the Cav1.3 channel ($IQ\text{-}A_{1.3}$) with the ICDI domain from Cav1.4 ($ICDI_{1.4}$) as the functional consequence of this interaction has been demonstrated in previous studies[8] and Chapter 1. Indeed, FRET two-hybrid measurements in aGPVMs yielded a robust binding curve (**Figure 16C**, gray) indicating a clear interaction between these two channel domains with high affinity. As such, this model interaction was used to compare with other interactions. Interestingly, all three IQ-A peptides bind well with $ICDI_{1.4}$, and all three ICDI peptides has relatively high affinity to $IQ_{1.3}$. The rest of the mix and match pairs bind with lower affinity (**Figure 16C**).

Next, we tested whether PKA can regulation these interactions. Remarkably, the interaction between of $IQ\text{-}A_{1.3}$ and $ICDI_{1.4}$ is largely disrupted when PKA is activated by the addition of 0.5 μM isoproterenol (**Figure 17A**, red). Moreover, this PKA effect can be elicited as a dynamic response within an exemplar myocyte (**Figure 17B, C**). The application of 0.5 μM isoproterenol decreases the FRET ratio exponentially indicating a disruption in binding. Of note, the individual CFP and FRET signals have corresponding changes, while the YFP signal remains relatively stable, indicating a genuine FRET response rather than an artifact due to isoproterenol acting directly on the fluorophores. Importantly, the decrease in FRET ratio (FR) can be reversed either by washing off isoproterenol (**Figure 17A**) or by inhibiting PKA via addition of either the wide-spectrum kinase inhibitor staurosporine (**Figure 17B**) or the PKA inhibitor H89 (**Figure 17C**), demonstrating a PKA specific effect. Thus the binding of $IQ\text{-}A_{1.3}$ and $ICDI_{1.4}$ can be dynamically modulated by PKA phosphorylation in a reversible manner.

This disruption of binding by PKA demonstrates a likely phosphorylation site on one of these two channel segments; however the interaction probed thus far has been between the ICDI and IQ domains of different L-type Ca^{2+} channels which may be unlikely to interact in a physiological setting[92]. We therefore probed for similar modulation within the ICDI and IQ domains from the same L-type Ca^{2+} channel subtype.

Gratifyingly, a FRET two-hybrid assay revealed a strong interaction between the IQ-A$_{1.4}$ and ICDI$_{1.4}$ peptides (**Figure 18A**, gray), which was diminished by PKA activation (**Figure 18A**, red and **B**) and reversed by the PKA inhibitor H89 (**Figure 18B**). In contrast, when both IQ and ICDI domains were from either Cav1.2 or Cav1.3, activating PKA had no effect on the binding affinity between the two domains (**Figure 19**). Thus Cav1.4 channels may represent the relevant native context for this PKA modulation. Moreover, the PKA modulation of ICDI$_{1.4}$ with multiple L-type Ca^{2+} channel IQ-A regions (**Figure 18, 19**) points to the likelihood that the phosphorylation site responsible for this effect lies within the ICDI region of the Cav1.4 channel.

The interaction between IQ and ICDI domains regulated by PKA in HEK293

The discovery that the binding between L-type Ca^{2+} channel IQ domains and ICDI$_{1.4}$ can be attenuated by PKA activation in aGPVMs is compelling, however the functional implications of this modulation could best be probed in a heterologous expression system where full control of channel and interacting partners is possible[14]. Unfortunately, full replication of PKA modulation of L-type channels is not always straightforward in recombinant systems[83]. We therefore sought to reconstruct the PKA regulation of IQ binding with ICDI in HEK293 cells. As the IQ-A$_{1.3}$/ICDI$_{1.4}$ interaction is robustly modulated (**Figure 17**), we first attempted to replicate the PKA modulation of this interaction through the application of forskolin. However, the effect of forskolin on this binding interaction was minimal (**Figure 21A**). Reasoning that HEK293 cells may have decreased endogenous PKA signaling as compared to aGPVMs, we overexpressed the constitutively active catalytic subunit of PKA (PKAc) and found that the binding of

IQ-A$_{1.3}$ with ICDI$_{1.4}$ was indeed reduced (**Figure 20B**). Given this success, we probed the PKA effect on IQ/ICDI interactions within a single channel subtype. Consistent with the data from aGPVMs, the interaction between IQ-A$_{1.4}$ and ICDI$_{1.4}$ was modulated by PKA (**Figure 20C**), while the interaction between peptides derived from Cav1.2 or Cav1.3 were unaffected (**Figure 20D, E**). Thus we have established PKA specific modulation of the IQ/ICDI interaction within Cav1.4 Ca^{2+} channels, as well as across Cav1.3 and 1.2 channels, within a heterologous system.

Utilizing this expression system, the functional consequence of this PKA modulation could now be assessed. Given the ability of ICDI to compete with CaM for the channel IQ region, we tested whether disruption of IQ/ICDI binding might affect channel CDI. We utilized the chimeric Cav1.3$_{S/1.4DCT}$ channel[6,8] (Cav1.3 with the DCT replaced by that of Cav1.4) as introduction of ICDI$_{1.4}$ in this channel is known to ablate the CDI of wild-type Cav1.3[8] as seen by the minimal difference in the decay of Ca^{2+} (red) versus Ba^{2+} (black) current (**Figure 20F**). However, if PKAc is now overexpressed in these cells, CDI is restored, as demonstrated by the stronger decay in the Ca^{2+} (red) current as compared to the Ba^{2+} (black) current (**Figure 20G**). Population data plotting the ratio of current remaining after 100 ms (r_{100}) demonstrates a hallmark U-shaped dependence on voltage, further corroborating a full restoration of CDI in the chimeric channel due to PKA activity. This restoration of CDI is indicative of a shift in the binding of the IQ region from ICDI$_{1.4}$ back to CaM in the phosphorylated state. Thus, PKA regulation of the IQ/ICDI interaction is capable of significantly altering the inactivation of L-type Ca^{2+} channels.

Creating a robust and controllable PKA system in HEK293 cells

While the dramatic effect on CDI is compelling, such constitutive activation of PKA could produce multiple long-term effects including alterations in gene expression[93]. Consequently, dynamic modulation of PKA activity is necessary to fully test the effect of PKA induced ICDI phosphorylation. Although PKA regulation of the $IQ_{1.3}$/$ICDI_{1.4}$ interaction was easily observed in aGPVMs (**Figure 17**), the same regulation was absent in HEK293 cells (**Figure 21**), which implies that endogenous PKA may not be sufficient in these cells for our experiments. It may therefore be necessary to overexpress PKA in order to achieve a functional model system.

As a tightly regulated and highly sensitive system, the regulatory subunits of PKA usually slightly outnumber the catalytic subunits at endogenous expression levels, so that most cells has minimal PKA activity at baseline (**Figure 22B**). The delicately balanced expression of regulatory and catalytic subunits in native systems cannot be easily achieved by standard heterologous expression, as co-transfection of both subunits results in mixed basal PKA activity. Indeed, when we co-expressed both subunits of PKA with the $Cav1.3_{S/1.4DCT}$ chimeric channels, we observed variable CDI (data not shown). To mimic the endogenous expression of native systems and guarantee low basal PKA activity, the overexpressed regulatory subunits have to slightly outnumber the overexpressed catalytic subunit. To achieve this, we linked the catalytic and regulatory subunits by a viral-based 2A sequence from porcine tescho virus (P2A) optimized and characterized in a previous study[94]. The P2A sequence causes a self-hydrolysis reaction at the translation level, resulting in complete dissociation and close to 1:1 stoichiometry of the linked subunits. A small amount of extra regulatory subunit (1 μg per 4 μg holoenzyme) was co-expressed with this P2A construct in order to ensure that PKA activity remained low at basal levels in every cell.

To test PKA holoenzyme in indeed overexpressed without increasing basal PKA activity, we used the FRET-based PKA activity sensor AKAR4[95], because it is a very sensitive PKA sensor that can detect endogenous PKA activity in HEK293 cells (**Figure 22A**). We first expressed AKAR4 in HEK293 cells, and measured the FRET efficiency (E_{eff}) of each cell by flow cytometer. At this endogenous PKA expression level, most cells exhibited low PKA activity, as illustrated by the low E_{eff} of AKAR4, while a small percentage of cells showed high basal PKA activity (**Figure 22B**). When PKA holoenzyme was also expressed as described above, every cell had minimal basal PKA activity, indicated by the low E_{eff} of AKAR4 (**Figure 22C**). In addition, when the cAMP level was elevated by adding 50μM forskolin, PKA activity was saturated in all cells, indicated by the high E_{eff} of AKAR4 (**Figure 22D**).

With the overexpression of PKA holoenzyme, the addition of 50 μM forskolin was now sufficient to rapidly decrease the FRET interaction between IQ-$A_{1.3}$ and $ICDI_{1.4}$ peptides within HEK293 cells (**Figure 21B**). Thus the PKA holoenzyme was overexpressed this way in the subsequent experiments in HEK293 cells.

Controllable PKA regulation of chimeric L-type channels in HEK293 cells

Having achieved robust forskolin-dependent PKA modulation of binding between L-type channel fragments in HEK293 cells, we next sought to test the effect of this modulation on channel function. We again utilized the well-studied chimeric

$\mathrm{Ca_V1.3_{S/1.4DCT}}$ channel, co-expressed with the PKA holoenzyme, as our model system. In order to minimize the perturbation of the cells, they were incubated with 50 μM forskolin for 30 minutes prior to whole-cell patch clamp recording. Indeed, forskolin incubation at room temperature restored a small but significant amount of CDI as compared to without forskolin (**Figure 22A, B**). However, the level of restoration is much less comparing to constitutive PKAc overexpression (**Figure 20G**), which indicates CDI restoration might takes longer than 30 minutes. We know that disruption of binding between $\mathrm{IQ\text{-}A_{1.3}}$ and $\mathrm{ICDI_{1.4}}$ peptides responds to PKA activation (**Figure 21C**) within a few minutes, then why CDI restoration of the chimeric channel develops much slower? On one hand, the effective local concentration of IQ domain near ICDI is higher in the holochannel configuration comparing to in the peptide form, as the two domains link together in the channel. Accordingly, it is harder for PKAc to approach and phosphorylate ICDI domain. On the other hand, slow CaM recruitment to the channel after disruption of the binding between IQ and ICDI interaction might also contribute to the slow response time. This hypothesis is supported by the slow time course observed when CaM was recruited to the same channel via rapamycin[6]. To speed up CDI restoration, we increased incubation temperature, and indeed observed larger amount of CDI restoration after incubation in forskolin at 30°C or 37°C for 30 minutes (**Figure 21D, E**). While the extent of CDI varied somewhat from cell to cell, a significant right shift in the cumulative distribution of r_{100} demonstrates a clear effect of forskolin on CDI (**Figure 21**). This sharp temperature dependence of phosphorylation kinetics explains the importance of body temperature at molecular level: slightly reduced temperature can largely inhibit biological reactions in a complex system, even though the interaction and phosphorylation reaction themselves are not expected to be very sensitive to small temperature fluctuation.

The fact that PKA activation can restore channel CDI confirmed that PKA regulation of interaction between IQ and ICDI domains has direct impact to channel function. However, based on our hypothesis, phosphorylation of ICDI by PKA should also increase the channel P_O. To observe the concurrent increase in P_O and CDI, we added 50μM forskolin while recording whole-cell Ca^{2+} currents at a bath temperature of 30°C. To avoid the loss of either PKA or CaM from the cytosol due to dialysis, we co-expressed AKAP79 to anchor PKA to the membrane, and tethered CaM to the β_2a subunit of the channel (**Figure 24A**). A 20 mV depolarizing step was applied for 150 ms every 30 seconds, allowing resolution of the current amplitude and CDI over the time course of forskolin wash-on (**Figure 24B**). The addition of forskolin caused a steady increase in peak current amplitude (green), reaching a level several fold larger than the pre-forskolin current. At the same time, the steady state current remaining after 100 ms was remarkably stable (gray), resulting in an increase in CDI. This outcome is consistent with a previous study whereby CaM was enriched near the $Ca_V1.3_{S/1.4DCT}$ channel via rapamycin-induced dimerization[6], further substantiating the hypothesis that PKA activation results in increased CaM binding to the channel IQ due to a reduction in the affinity of $IQ_{1.3}$ with $ICDI_{1.4}$.

$ICDI_{1.4}$ can act as a modular phospho-switch for $Ca_V1.2$

Beyond $Ca_V1.3$, $ICDI_{1.4}$ was also able to bind to $IQ\text{-}A_{1.2}$ in a PKA sensitive manner (**Figure 19C**). We wondered whether this $ICDI_{1.4}$ module could serve as a synthetic phospho-switch for Cav1.2 Ca^{2+} channels, able to be plugged into a system simply by co-expression as a cytosolic peptide. Such synthetic modulation of the Cav1.2 channel may be of particular interest as these channels are known to undergo a large increase in current amplitude in response to PKA activation in myocytes, however this effect is exceedingly difficult to replicate in recombinant systems[83]. We therefore sought to utilize $ICDI_{1.4}$ to generate PKA modulation of Cav1.2 channels in HEK293 cells. In order to maintain the properties of cardiac Cav1.2 channels as much as possible in our recombinant system, we co-expressed $ICDI_{1.4}$ as a peptide along with the full-length cardiac Cav1.2 channel, and utilized the β_{1b} Ca^{2+} channel subunit which more closely recapitulates the inactivation profile found in native cardiac myocytes[91] (**Figure 25A**). As before, CaM was linked to the beta subunit, and AKAP was co-expressed so as to reduce dialysis of the key elements. Under these conditions, application of 50 μM forskolin largely increased the peak amplitude (**Figure 25B**), similar to the native PKA up-regulation of cardiac Cav1.2 channels (**Figure 26**). In addition, an increase in CDI was seen even in the presence of significant voltage dependent inactivation due to the use of the β_{1b} subunit[96]. Thus, the effect of $ICDI_{1.4}$ on channel regulation demonstrated in the chimeric $Cav1.3_{S/1.4DCT}$ channel appears to be generalizable to other L-type Ca^{2+} channels. Moreover, $ICDI_{1.4}$ need not be covalently attached to the channel, but rather is capable of acting as a diffusible CDI/P_O switch, which can be turned off by PKA phosphorylation.

PKA activation regulates full-length $Ca_V1.4$ channels

It is now clear that $ICDI_{1.4}$ can serve as a synthetic phospho-switch for Cav1.2 and Cav1.3 channels. However, a native function for this module has yet to be demonstrated. Given that the FRET interaction of $\mathrm{ICDI}_{1.4}$ with $\mathrm{IQ\text{-}A}_{1.4}$ is dramatically reduced by PKA activation (**Figure 18** and **Figure 20c**), our data predicts that native $\mathrm{Ca_V}1.4$ channels are likely modulated by PKA. To elucidate this effect, we co-expressed full-length, wild-type $\mathrm{Ca_V}1.4$ along with PKA (**Figure 27A**) as previously done for the chimeric channel (**Figure 23A**). Indeed, these channels exhibited no CDI at baseline, however following a 60-minute incubation with forskolin, considerable CDI was elicited (**Figure 27B**). In addition, co-expression of wild-type $\mathrm{Ca_V}1.4$ with β_{2a}-CaM, AKAP and PKA allowed for resolution of a dynamic response to PKA (**Figure 27C**). In response to the addition of 50 μM forskolin, both the peak current amplitude and CDI increased significantly (**Figure 27D**). Thus wild-type $\mathrm{Ca_V}1.4$ channels employ a mechanism for CDI and P_O modulation whereby $\mathrm{ICDI}_{1.4}$ binds to the IQ region at baseline, and is displaced by CaM following the phosphorylation of $\mathrm{ICDI}_{1.4}$ by PKA. With CaM residing on the IQ region of the channel, the channel P_O is increased and CDI is enabled[6].

Lack of ICDI mediated PKA regulation of $\mathrm{Ca_V}1.3$ and $\mathrm{Ca_V}1.2$

The ICDI domain of $\mathrm{Ca_V}1.4$ exhibits significant sequence homology to the ICDI domain of other L-type $\mathrm{Ca^{2+}}$ channels (**Figure 6**). In fact, the ability of ICDI to compete with CaM for binding to the IQ domain of the channel has been demonstrated for both $\mathrm{Ca_V}1.3$ and $\mathrm{Ca_V}1.2$ channels. However, we utilized the FRET two-hybrid binding assay to probe for interactions between the IQ and ICDI regions of $\mathrm{Ca_V}1.3$ and 1.2 channels and demonstrated that they are not regulated by PKA activation in either aGPVMs (**Figure 19C, D, G, H**) or HEK293 cells (**Figure 20D, E**). Thus, we expected full-length CaV1.2 and 1.3 channels could not be regulated by PKA activation. Indeed, even with the enhanced PKA expression system used for Cav1.4 channels (**Figure 27C**), forskolin failed to induce a change in CDI or current amplitude of Cav1.3 channels in HEK 293 cells (**Figure 28A**, **B**). Similarly for Cav1.2 channels, no modulation of CDI or current amplitude can be seen in the heterologous expression system (**Figure 28C**, **D**). Thus despite the sequence similarity of IQ and ICDI domains across Cav1.2, 1.3 and 1.4, the PKA regulation is unique in Cav1.4.

Identification of the PKA phosphorylation site within Ca$_V$1.4

Thus far we have demonstrated that elevated PKA activity correlates with increased peak current amplitude and CDI of L-type Ca^{2+} channels in the presence of ICDI$_{1.4}$. We hypothesized that this effect is due to direct phosphorylation of ICDI$_{1.4}$, however an indirect effect due to phosphorylation of an unknown ICDI interacting element could produce a similar result. As a first step towards identifying the site, we utilized the bioinformatics tool pkaPS[97] to predict potential PKA phosphorylation sites within ICDI$_{1.4}$. From this prediction algorithm, S1883 appeared to be the most likely site (**Figure 29A**).

To confirm this result, we employed mass spectroscopy to identify phosphorylation sites within ICDI$_{1.4}$. In order to induce phosphorylation, a histidine-tagged ICDI$_{1.4}$ peptide was co-expressed with the PKA holoenzyme in HEK293 cells and subjected to one hour of forskolin treatment. The result of mass spectroscopy on this peptide revealed that S1883 is indeed phosphorylated (**Figure 31A** and **Figure 30**), however an additional phosphorylation site at S1886 could not be ruled out (see Methods).

Having established S1883 as a potential PKA phosphorylation site, we sought to determine whether this site is responsible for the functional modulation of the channel. To determine if the site is required for the PKA modulation of binding between L-type channel IQ regions and $ICDI_{1.4}$, we utilized a novel flow-cytometer based high-throughput platform for live-cell FRET two-hybrid binding assay[49]. As seen by traditional FRET two-hybrid binding (**Figure 20B**), overexpression of PKAc reduced the binding affinity of Venus-tagged $IQ\text{-}A_{1.3}$ and Cerulean-tagged $ICDI_{1.4}$ peptides (**Figure 31B, C**). However, when S1883 within $ICDI_{1.4}$ was mutated to alanine, the PKA modulation of the interaction was abolished (**Figure 31D**). In contrast, if S1886 was mutated to alanine, PKA regulation was preserved (**Figure 31E**). Finally, we probed the functional effect of the S1883A mutation via whole cell patch clamp recording. The $Cav1.3_{S/1.4DCT}$ chimeric channel was utilized for these experiments as it expresses well and exhibits robust and consistent PKA modulation. Mutation of S1883 to alanine had no effect on channel properties in the absence of PKA (**Figure 31F**), however overexpression of PKAc failed to alter CDI (**Figure 31G**), confirming that S1883 is a novel and functional PKA phosphorylation site within the Cav1.4 ICDI domain.

Discussion

PKA phosphorylation of $ICDI_{1.4}$ has significant, previously unreported, effects on wild-type Cav1.4 channels. Such novel PKA regulation may have important physiological consequences. Cav1.4 is the main L-type Ca^{2+} channel in the retina[92]. While the difficulty in obtaining electrophysiological recordings from photoreceptors makes detailed study of their PKA modulation challenging, the creation of a robust PKA system in HEK293 cells has enabled new mechanistic insight. We now know that PKA phosphorylation of ICDI$_{1.4}$ disrupts its IQ binding, allowing CaM to bind the IQ region, thus increasing channel P_O and CDI. Such a mechanism may well be at play in the retina. Ca^{2+} currents within photoreceptors exhibit a modest amount of CDI, which has been attributed to a mixture of Cav1.4 channel splice variants[86,98]. Here, we have demonstrated that even the long splice variant, containing ICDI$_{1.4}$, is capable of supporting CDI under elevated PKA activation and likely contributes to the CDI seen in these cells. Moreover, ICDI$_{1.4}$ is highly expressed in retina and PKA activity retina is robustly regulated by dopamine[99]. As the dopamine fluctuations in the retina with circadian rhythmicity, they exhibit oscillations with periods lasting for many hours[100,101] rationalizing the relatively slow kinetics of Cav1.4 regulation by PKA (**Figure 27D**). Thus, PKA regulation of Cav1.4 could modulate visual sensitivity during the day-night cycle. In fact, channelopathic mutations in Cav1.4 which cause premature truncation before the ICDI domain, result in congenital stationary night blindness[9,13], demonstrating the importance of this module in low light adaptation.

Beyond Cav1.4 channels, ICDI$_{1.4}$ was able to endow chimeric Cav1.3 and 1.2 channels with robust PKA modulation, demonstrating a generalizable mechanism for regulation of L-type channel CDI and P_O. Moreover, ICDI$_{1.4}$ was also able to act as a synthetic phospho-switch when co-expressed as a separate peptide with Cav1.2 channels. This synthetic PKA modulation of channel opening and CDI could be a valuable tool to study the physiological role of CDI and P_O, as this small peptide could be easily transduced into native cells. Moreover, co-expression of this peptide at basal PKA levels mimics the properties of certain long Ca^{2+} channel splice variants[6], while elevation of PKA activity reverts the phenotype of these channels to that of a short splice variant. As such, this tool could aid in understanding the functional effects of alterations in splice variant expression in different cell types.

Such a synthetic phospho-switch may have added value beyond that of a novel tool for regulating L-type Ca^{2+} channels. It may shed light on the mechanism underlying native PKA regulation of L-type Ca^{2+} channels. In particular, the regulation of cardiac Cav1.2 channels by PKA is a critical feature of the fight-or-flight response, but the full mechanistic pathway underlying this regulation remains under debate[24,43]. While PKA activation readily increases Cav1.2 current by several fold in adult cardiomyocytes, such large PKA upregulation is not often observed in heterologous systems such as HEK293 cells[83], even in the presence of exogenous PKA holoenzymes (**Figure 28D**). It appears, then, that there must be a critical element in myocytes which is lacking in recombinant systems[24,91]. Given the ability of $ICDI_{1.4}$ to modulate Cav1.2 channel P_O in a phosphorylation dependent manner, we wonder if the missing element in myocytes may employ a similar strategy. Thus, searching for proteins capable of binding channel IQ domains may prove a useful approach.

To ensure the presence of all key elements of the PKA pathway within our binding assay, we implemented quantitative live-cell FRET two-hybrid binding in acutely isolated aGPVMs. This system enabled us to probe the PKA modulation of $IQ/ICDI_{1.4}$ interactions, a phenomenon which was not initially observable in HEK293 cells (**Figure**

21A). This failure of forskolin to modulate the IQ/ICDI$_{1.4}$ interactions in HEK293 cells at baseline points to an important limitation of these cells. While these cells have proven quite useful for studying many types of PKA modulation including HERG[50], K$_V$1.1[52] and nicotinic receptors[45], they appear less ideal for studying the modulation of L-type Ca^{2+} channels. It therefore seems likely that these phosphorylation targets have different thresholds for PKA modulation, and model systems in which PKA is sufficient for one application may not be suitable for all target proteins.

Overall, we have demonstrated that the repertoire of PKA regulation of L-type Ca^{2+} channels extends to Ca$_V$1.4 channels. The identification of the phosphorylation site within the Ca$_V$1.4 ICDI domain fits well with a mechanism in which PKA mediated phosphorylation alters the binding affinity between the IQ and ICDI domains of Ca$_V$1.4, thus tuning the extent of CDI and channel P_O via competitive displacement of CaM. Given the distribution of Ca$_V$1.4 channels, this modulation might play an important role in the visual system and in tuning the circadian rhythm, and may represent a general mechanism by which various L-type channels could be modulated by currently unidentified competitors of CaM.

Figures

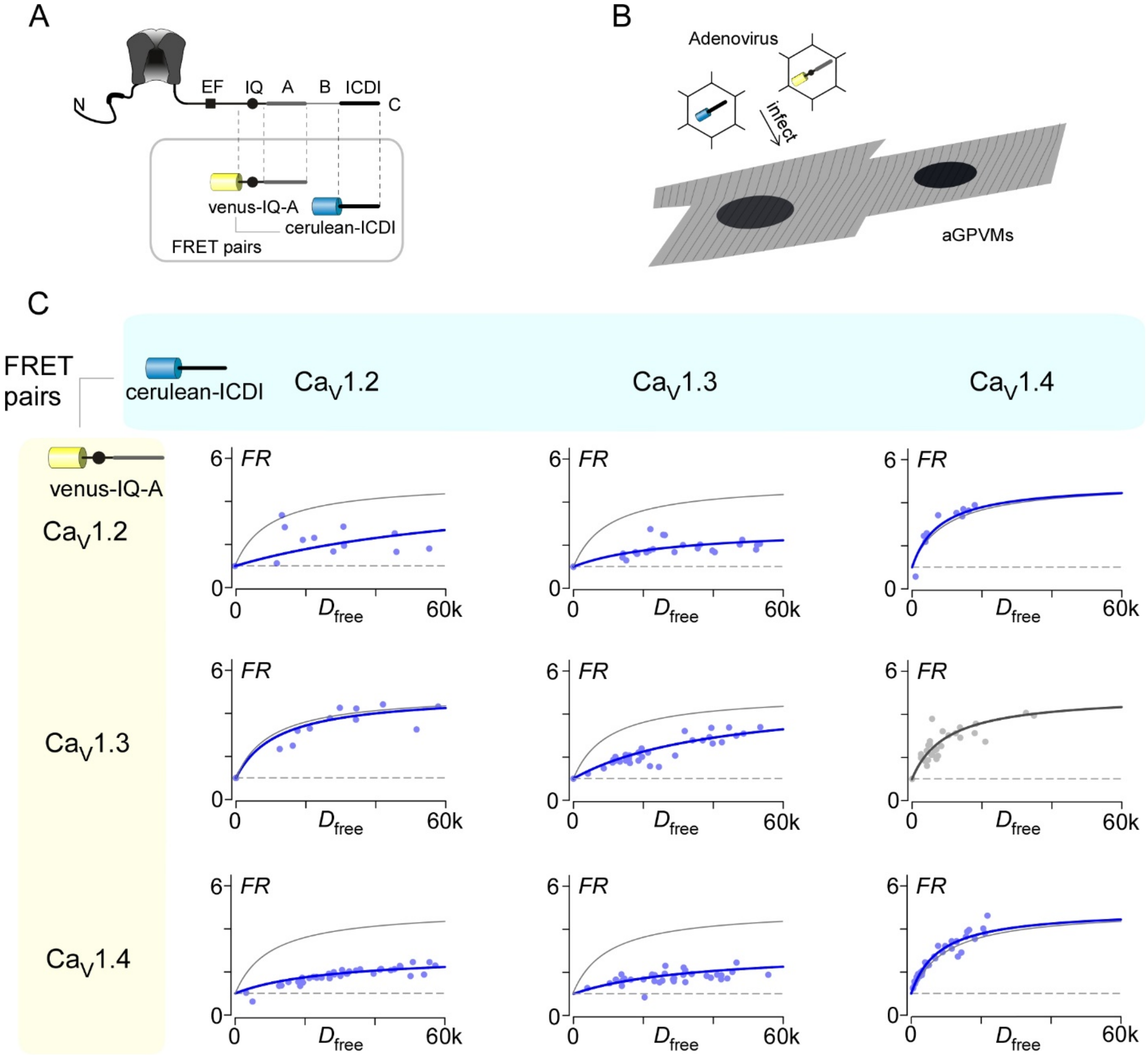
A
N
EF
IQ
A
B
ICDI
C
venus-IQ-A
cerulean-ICDI
FRET pairs
B
Adenovirus
infect
aGPVMs
C
FRET pairs
cerulean-ICDI
$Ca_V1.2$
$Ca_V1.3$
$Ca_V1.4$
venus-IQ-A
$Ca_V1.2$
$Ca_V1.3$
$Ca_V1.4$
6
FR
0
0
D_{free}
60k

Figure 16. FRET two-hybrid assays of IQ-A/ICDI interactions in aGPVMs.

(**A**) FRET partners are Venus- IQ-A peptide and Cerulean-ICDI peptides from L-type calcium channels. (**B**) Adenovirus incorporating FRET binding partners were used to infect aGPVMs. (**C**) The IQ-A peptides and ICDI peptides from Cav1.2, Cav1.3 and Cav1.4 were mixed and matched to generate nine binding pairs. Binding curves were constructed for each of the nine binding paris by FRET two-hybrid in aGPVMs. Each filled circle represents recording from a single cell. The binding curve of Venus-IQ-A from Cav1.3 and Cerulean-ICDI from Cav1.4 (gray) were replicated in all other plots.

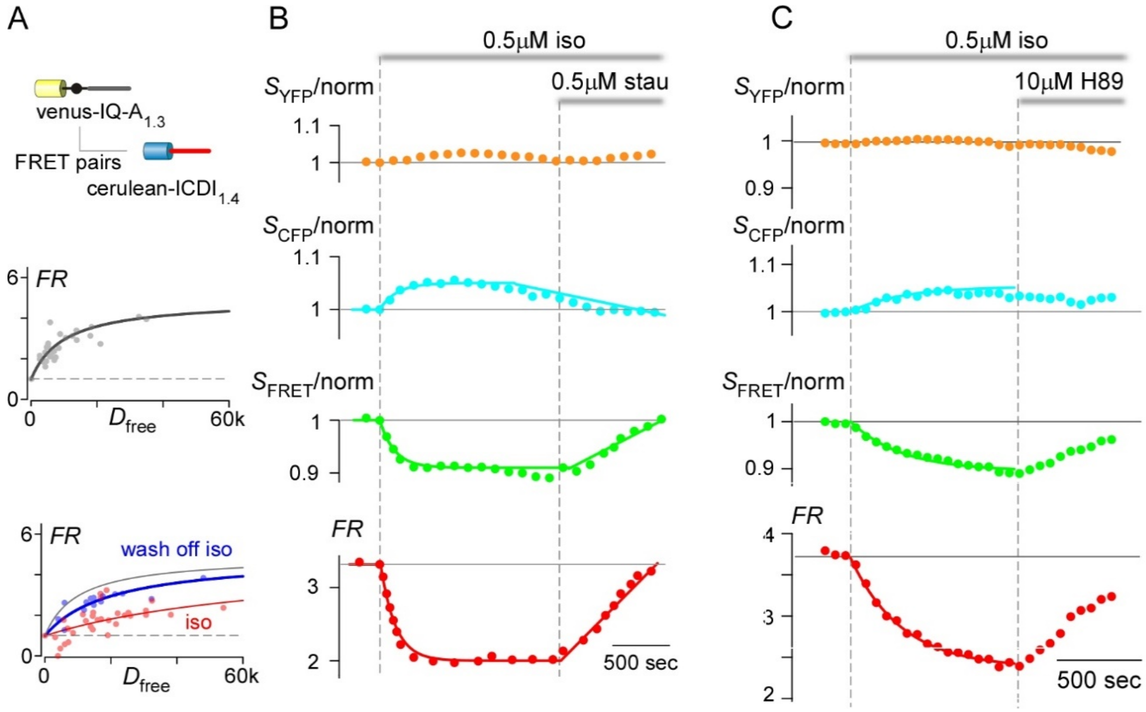
A
venus-IQ-$A_{1.3}$
FRET pairs
cerulean-$ICDI_{1.4}$
6
FR
0
0
D_{free}
60k
6
FR
wash off iso
iso
0
0
D_{free}
60k
B
0.5μM iso
0.5μM stau
S_{YFP}/norm
1.1
1
S_{CFP}/norm
1.1
1
S_{FRET}/norm
1
0.9
FR
3
2
500 sec
C
0.5μM iso
10μM H89
S_{YFP}/norm
1
0.9
S_{CFP}/norm
1.1
1
S_{FRET}/norm
1
0.9
FR
4
3
2
500 sec

Figure 17. PKA regulation of $IQ_{1.3}$ and $ICDI_{1.4}$ interactions in aGPMVs.

(**A**) FRET binding curve for Venus-IQ-$A_{1.3}$ paired with Cerulean-$ICDI_{1.4}$ (gray). 0.5 μM isoproterenol (red) decreases the relative binding affinity. Each point indicates a single cell. The control binding curve is replicated as the gray curve in the lower panel here and throughout. *FR*, FRET ratio; D_{free}, relative concentration of unbound Cerulean-tagged $ICDI_{1.4}$. (**B**) Kinetics of normalized fluorescent signals from YFP channel (S_{YFP}), CFP channel (S_{CFP}), FRET channel (S_{FRET}) and calculated *FR* from an exemplar aGPVM expressing Venus-IQ-$A_{1.3}$ and Cerulean-$ICDI_{1.4}$, with 0.5 μM isoproterenol and 0.5 μM staurosporine added as indicated. Fluorescent signals were normalized to baseline here and throughout. (**C**) Kinetics of normalized fluorescent signals and *FR* from an exemplar aGPVM expressing Venus-IQ-$A_{1.3}$ and Cerulean-$ICDI_{1.4}$, with 0.5 μM isoproterenol and 10 μM H89 added as indicated. For this data set, a movement artifact was noted in the raw YFP signal and was divided out of the final data set.

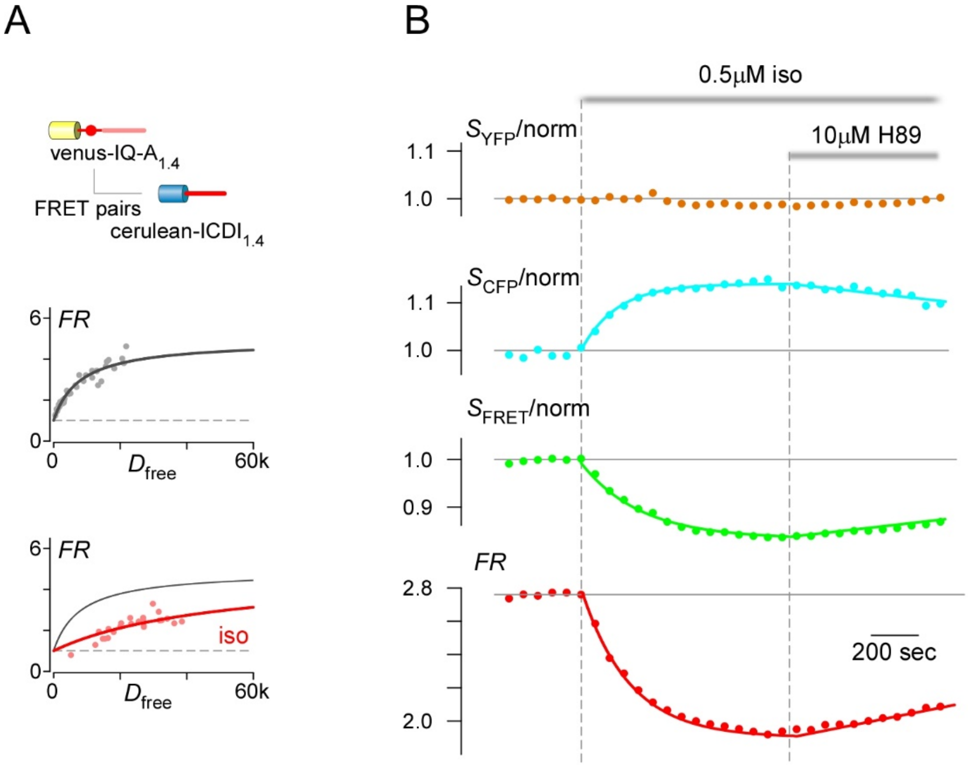

Figure 18. PKA regulation of $IQ_{1.4}$ and $ICDI_{1.4}$ interactions in aGPMVs.

(**A**) FRET binding curve for Venus-IQ-$A_{1.4}$ paired with Cerulean-$ICDI_{1.4}$ (gray). 0.5 μM isoproterenol (red) decreases the relative binding affinity. (**B**) Kinetics of normalized fluorescent signals from YFP channel (S_{YFP}), CFP channel (S_{CFP}), FRET channel (S_{FRET}) and calculated *FR* from an exemplar aGPVM expressing Venus-IQ-$A_{1.4}$ and Cerulean-$ICDI_{1.4}$, with 0.5 μM Isoproterenol and 10 μM H89 added as indicated. Fluorescent signals were normalized to baseline here and throughout.

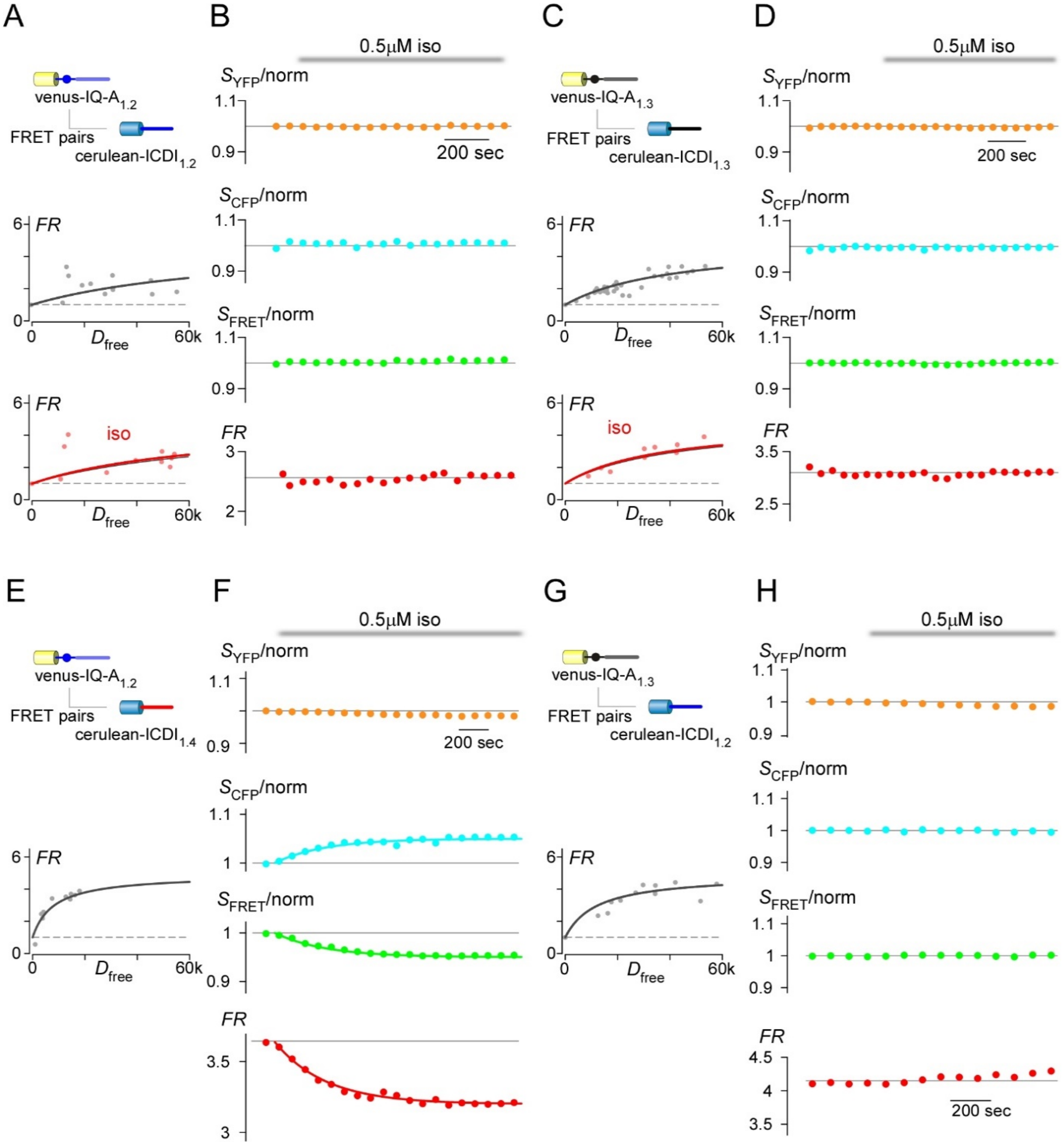
A
B
C
D
0.5μM iso
venus-IQ-A1.2
FRET pairs
cerulean-ICDI1.2
venus-IQ-A1.3
cerulean-ICDI1.3
SYFP/norm
SCFP/norm
SFRET/norm
FR
iso
Dfree
0
60k
6
1.1
0.9
3
2
3.5
2.5
200 sec
E
F
G
H
venus-IQ-A1.2
cerulean-ICDI1.4
venus-IQ-A1.3
cerulean-ICDI1.2
1
4.5
4

Figure 19. PKA regulation of other IQ and ICDI interactions in aGPMVs.

(**A**) FRET binding assays between Venus-IQ-A$_{1.2}$ and Cerulean-ICDI$_{1.2}$ peptides, without (gray) or with (red) application of isoproterenol (iso). The gray curve in the middle panel is replicated in the lower panel, overlapping the red curve. (**B**) Kinetics of normalized fluorescent signals from the YFP channel (S_{YFP}), CFP channel (S_{CFP}), FRET channel (S_{FRET}) and calculated FRET ratio (FR) from an exemplar aGPVM expressing Venus-IQ-A$_{1.2}$ and Cerulean-ICDI$_{1.2}$. Isoproterenol was applied as indicated, without any effect. Fluorescent signals were normalized to baseline. (**C**) FRET binding assays between Venus-IQ-A$_{1.3}$ and Cerulean-ICDI$_{1.3}$ peptides, without (gray) or with (red) isoproterenol. (**D**) Lack of response to isoproterenol by an exemplar aGPVM expressing Venus-IQ-A$_{1.3}$ and Cerulean-ICDI$_{1.3}$ peptides. (**E**) FRET binding curve indicating robust interaction between Venus-IQ-A$_{1.2}$ and Cerulean-ICDI$_{1.4}$ peptides. (**F**) Isoproterenol causes a significant decrease in FR within an exemplar aGPVM expressing Venus-IQ-A$_{1.2}$ and Cerulean-ICDI$_{1.4}$ peptides. (**G**) FRET binding assay between Venus-IQ-A$_{1.3}$ and Cerulean-ICDI$_{1.2}$ peptides. (**H**) Lack of response to isoproterenol in an exemplar aGPVM expressing Venus-IQ-A$_{1.3}$ and Cerulean-ICDI$_{1.2}$ peptides.

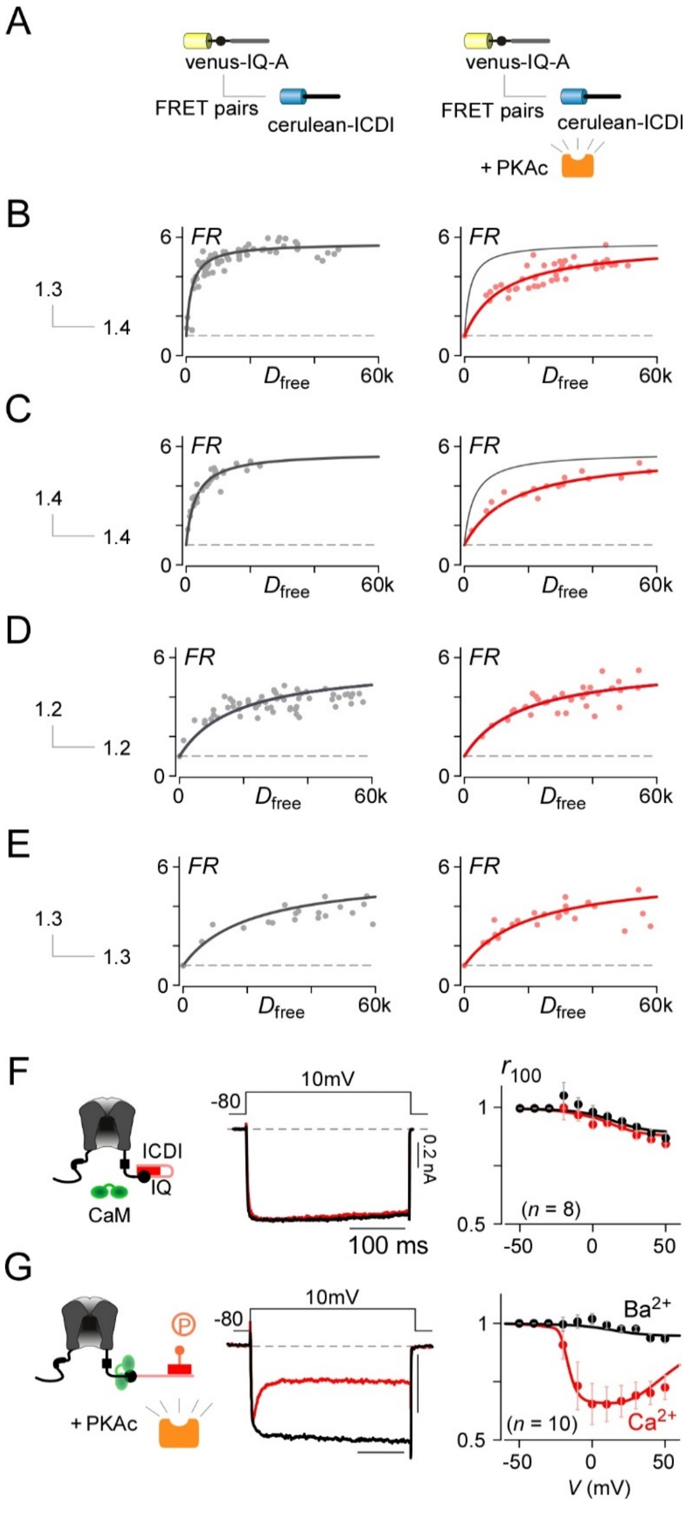
A
venus-IQ-A
FRET pairs
cerulean-ICDI
venus-IQ-A
FRET pairs
cerulean-ICDI
+ PKAc
B
1.3
1.4
FR
6
0
D_{free}
60k
C
1.4
1.4
D
1.2
1.2
E
1.3
1.3
F
ICDI
IQ
CaM
-80
10mV
0.2 nA
100 ms
r_{100}
1
0.5
(n = 8)
-50
0
50
G
+ PKAc
-80
10mV
Ba2+
Ca2+
(n = 10)
V (mV)

Figure 20. The catalytic subunit of PKA regulates IQ binding to $ICDI_{1.4}$ in HEK293 cells.

(**A**) FRET binding assays (**B**-**E**) between Venus-IQ-A and Cerulean-ICDI demonstrating the effect of PKAc overexpression. (**B, C**) PKAc reduces the binding between IQ-$A_{1.3}$ and $ICDI_{1.4}$ (**B**) and between IQ-$A_{1.4}$ and $ICDI_{1.4}$ (**C**). (**D, E**) PKAc does not change binding between IQ-$A_{1.2}$ and $ICDI_{1.2}$ (**D**) or IQ-$A_{1.3}$ and $ICDI_{1.3}$ (**E**). (**F**) Cartoon of the chimeric channel $Ca_V1.3_{S/1.4DCT}$ made by attaching the DCT of $Ca_V1.4$ (including ICDI, red) to a truncated $Ca_V1.3$ (left). Exemplar of whole-cell current (middle) illustrates a lack of CDI, as seen by the minimal difference in decay of Ca^{2+} (red) versus Ba^{2+} (black) current. Vertical scale bar pertains to Ca^{2+} current; Ba^{2+} current scaled downwards ~3× to facilitate comparison of decay kinetics, here and throughout. Population data (right) confirmations minimal CDI of this chimera. The fraction of peak current remaining after 100-ms (r_{100}) is plotted versus step voltage (V), for Ba^{2+} (black) and Ca^{2+} (red) currents (mean ± SEM). (**G**) Overexpression of PKAc (left) restored CDI of this chimeric channel, showing a strong decay of Ca^{2+} current (red) compared to Ba^{2+} current (black). The classic U-shaped voltage dependence of CDI is seen in the population data (right).

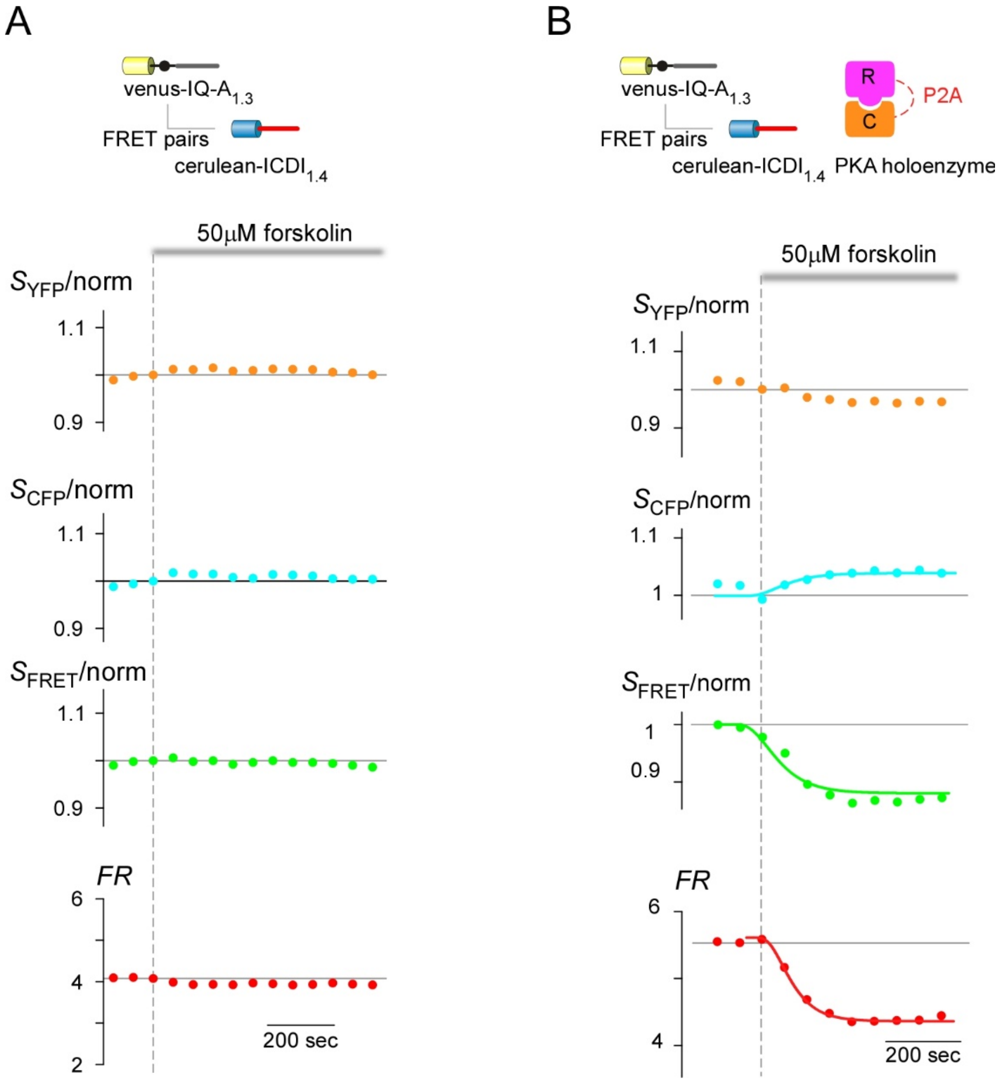

Figure 21. Forskolin regulation of the interaction of $IQ_{1.3}$ and $ICDI_{1.4}$ in HEK293. (**A**) Time course of normalized fluorescent signals from YFP channel (S_{YFP}), CFP channel (S_{CFP}), FRET channel (S_{FRET}) and calculated FRET ratio (*FR*) from an exemplar HEK293 cell expressing Venus-IQ-$A_{1.3}$ and Cerulean-$ICDI_{1.4}$ peptides. (**B**) Time course of normalized fluorescent signals and calculated *FR* from an exemplar HEK293 cells expressing Venus-IQ-$A_{1.3}$, Cerulean-$ICDI_{1.4}$ peptides, and PKA holoenzyme.

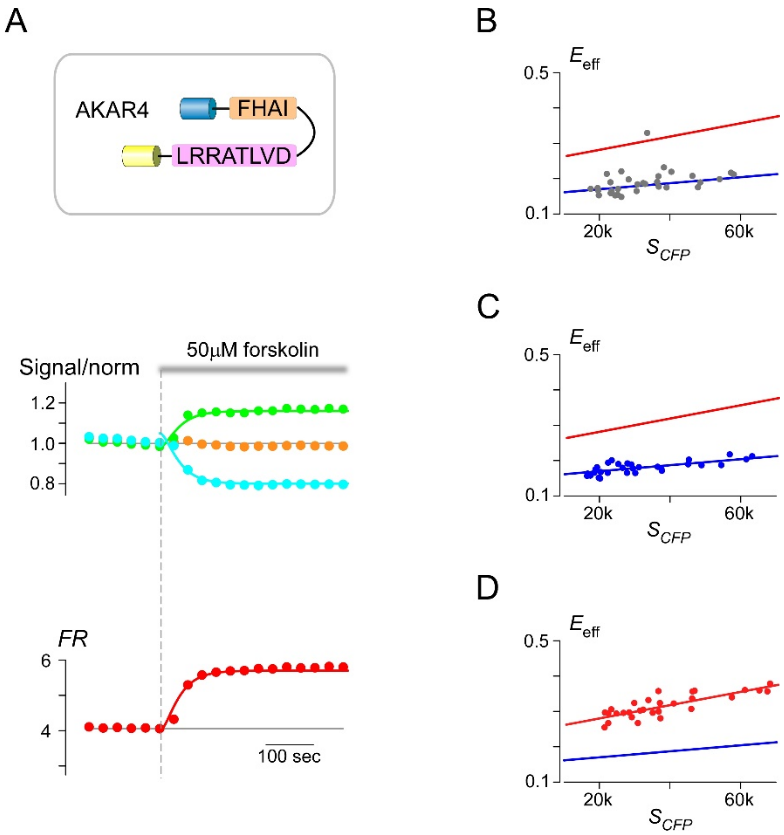

Figure 22. Co-expressing PKA holoenzyme ensures robust and controllable PKA activity.

(**A**) An exemplar recording demonstrating the kinetics of the AKAR response in HEK 293 cells. YFP signal: yellow; CFP signal: cyan; FRET signal: green; FR: red. (**B**) FRET efficiency (E_{eff}) measured for HEK293 cells expressing the PKA sensor AKAR4[4]. Each point indicates a single cell. The blue line represents low PKA activity, and the red line indicates high PKA activity. (**C**) E_{eff} measured for HEK293 cells expressing AKAR4 and PKA holoenzyme, without forskolin treatment. (**D**) E_{eff} measured for fosrkolin treated HEK293 cells expressing AKAR4 and PKA holoenzyme, recorded after incubation in 50μM forskolin for 10 minutes.

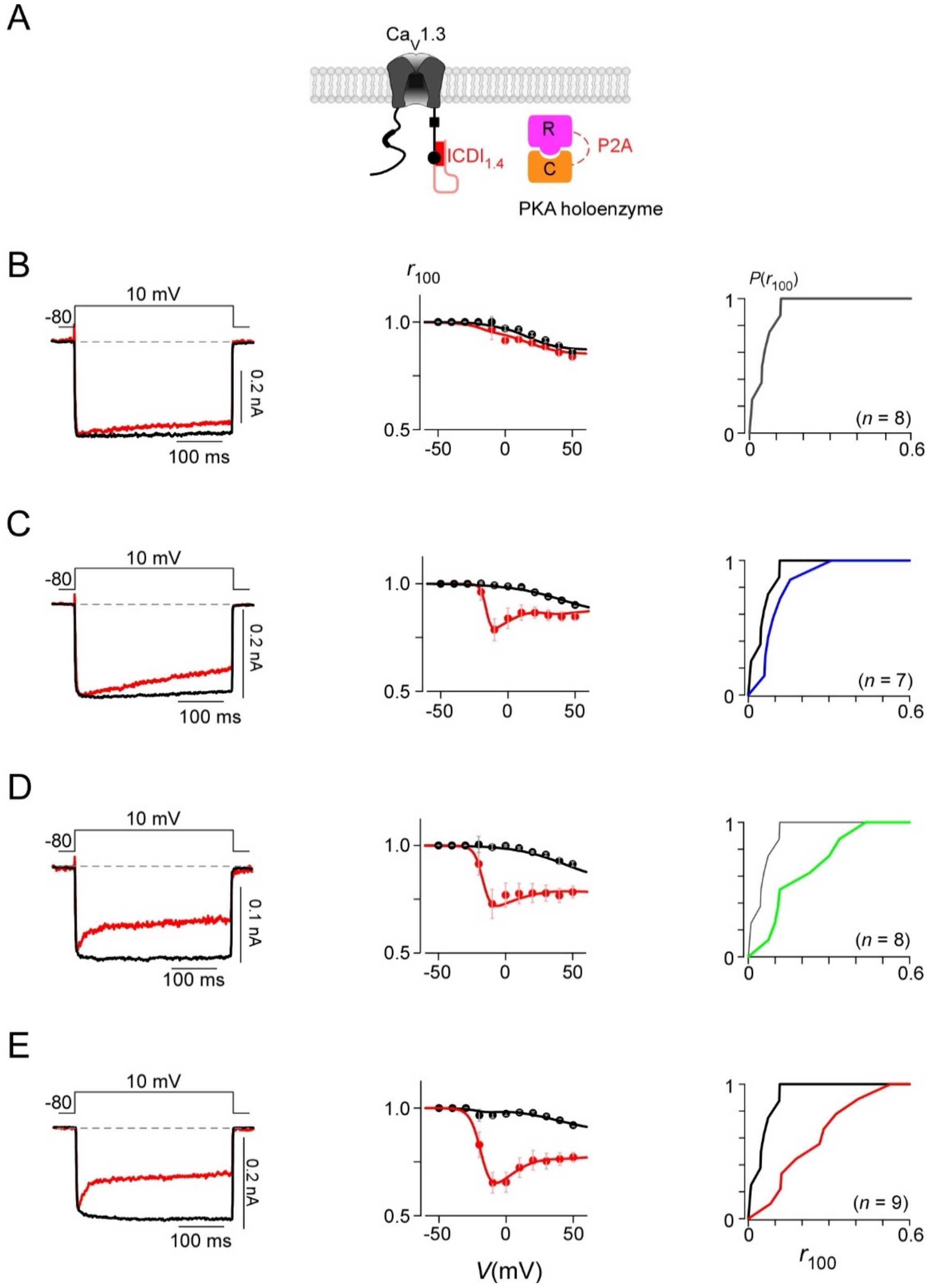
A
Ca$_V$1.3
ICDI$_{1.4}$
R
C
P2A
PKA holoenzyme
B
10 mV
-80
0.2 nA
100 ms
r_{100}
1.0
0.5
-50
0
50
$P(r_{100})$
1
0
0.6
(n = 8)
C
10 mV
-80
0.2 nA
100 ms
(n = 7)
D
10 mV
-80
0.1 nA
100 ms
(n = 8)
E
10 mV
-80
0.2 nA
100 ms
(n = 9)
V(mV)
r_{100}

Figure 23. Temperature dependence of PKA modulation of Ca$_V$1.3$_{S/1.4DCT}$

(**A**) Schematic of HEK293 cells co-expressing Ca$_V$1.3$_{S/1.4DCT}$ channels, PKA holoenzyme (catalytic subunit, C and regulatory subunit, R, linked by a P2A sequence at the DNA level). (**B**) Minimal CDI at basal PKA levels. (Left) Exemplar of whole-cell current illustrates a lack of CDI, as seen by the minimal difference in decay of Ca^{2+} (red) versus Ba^{2+} (black) currents. Vertical scale bar pertains to Ca^{2+} current; Ba^{2+} current scaled downwards ~3× to facilitate comparison of decay kinetics, here and throughout. (Middle) Population data confirmations minimal CDI. The fraction of peak current remaining after 100-ms (r_{100}) is plotted versus step voltage (V), for Ba^{2+} (black) and Ca^{2+} (red) currents (mean ± SEM). (right) The tight cumulative distribution of r_{100} across all cells also indicates minimal CDI. (**C**) CDI emerges after incubation in 50 μM forskolin at 23°C for 30 minutes. (**D**) Incubation with 50 μM forskolin for 30 min at 30°C increases the extent of CDI. (**E**) Incubation with 50 μM forskolin for 30 min at 37°C further increases the extent of CDI.

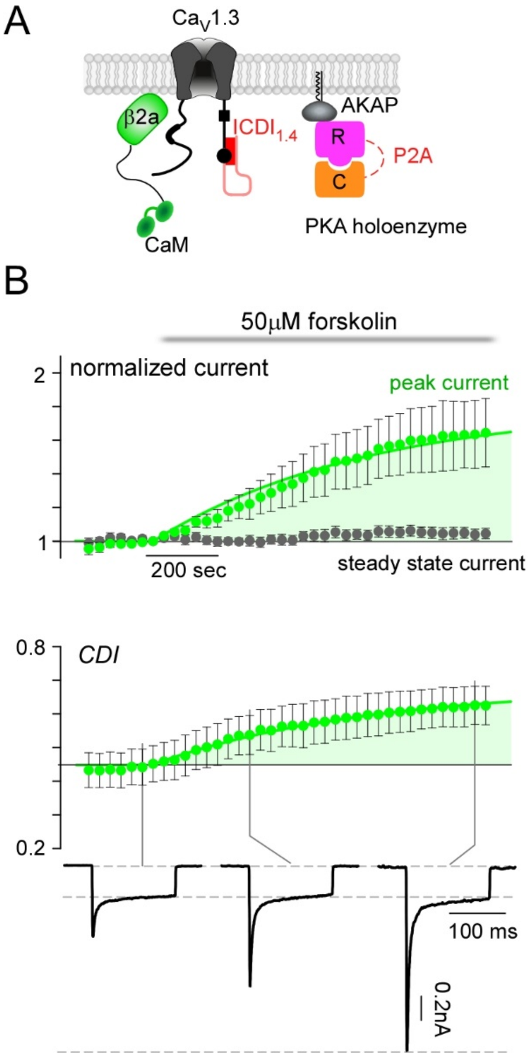
A
CaV1.3
β2a
CaM
ICDI1.4
AKAP
R
C
P2A
PKA holoenzyme
B
50μM forskolin
normalized current
2
1
peak current
200 sec
steady state current
0.8
CDI
0.2
100 ms
0.2nA

Figure 24. Dynamic PKA regulation of chimeric Ca$_V$1.3$_{S/1.4DCT}$ channels in HEK293 cells.

(**A**) Schematic of HEK293 cells co-expressing chimeric Cav1.3$_{S/1.4DCT}$ and PKA holoenzyme (catalytic subunit, C and regulatory subunit, R, linked by a P2A sequence at the DNA level), AKAP79 and β_{2a} tethered CaM which allowed longer whole cell patching without loss of PKA or CaM. (**B**) Time course of normalized peak current (green) and steady state current (gray) in response to the addition of 50 μM forskolin, evoked every 30 seconds by depolarizations to 20 mV (top). The corresponding increase in CDI (middle) from whole-cell Ca^{2+} currents. Currents were normalized to baseline. CDI was measured as 1 - r_{100}. All error bars indicate +/- SEM (n = 6 cells). Corresponding current waveforms are displayed below.

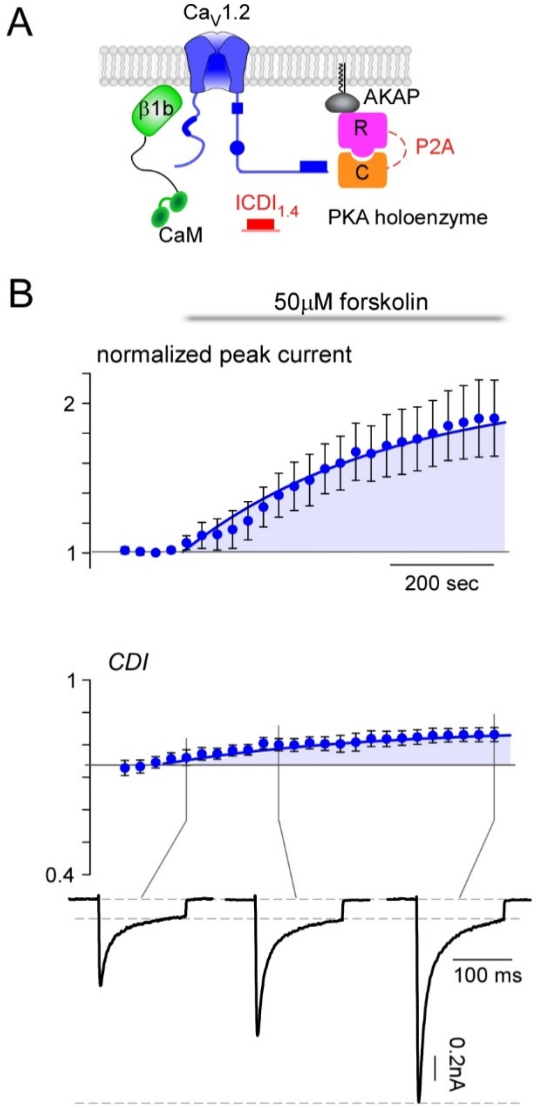
A
Ca$_V$1.2
AKAP
β1b
R
P2A
C
ICDI$_{1.4}$
CaM
PKA holoenzyme
B
50μM forskolin
normalized peak current
2
1
200 sec
CDI
1
0.4
100 ms
0.2nA

Figure 25. Synthetic PKA regulation of $Ca_V1.2$ in HEK293 cells.

(**A**) Schematic of full-length $Ca_V1.2$ channel, PKA honoenzyme (R and C) and $ICDI_{1.4}$ peptide, along with β_{1b} tethered CaM and AKAP79. (**B**) Time course of the normalized peak current (top) and CDI (middle), from whole-cell Ca^{2+} currents, evoked every 30 seconds by depolarizations to 20 mV. Currents were normalized to baseline. CDI measured as 1 - r_{100}. All error bars indicate +/- SEM (n = 6 cells). Corresponding current waveforms are displayed below.

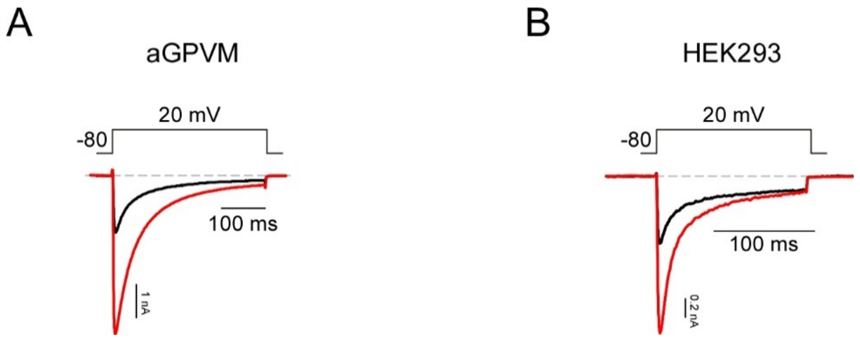

Figure 26. Comparison of the native and synthetic regulation of Ca$_V$1.2.

(**A**) Ca^{2+} current elicited by step depolarization from -80mV to 20mV from an adult guinea pig ventricular myocyte (aGPVM), before (black) and after (red) application of 0.5 µM isoproterenol. (**B**) Ca^{2+} current from a HEK293 cell expressing Ca$_V$1.2, ICDI$_{1.4}$ peptide and PKA holoenzyme (**Figure 25A**), elicited by step depolarization from -80mV to 20mV, before (black) and after (red) application of 50 µM forskolin.

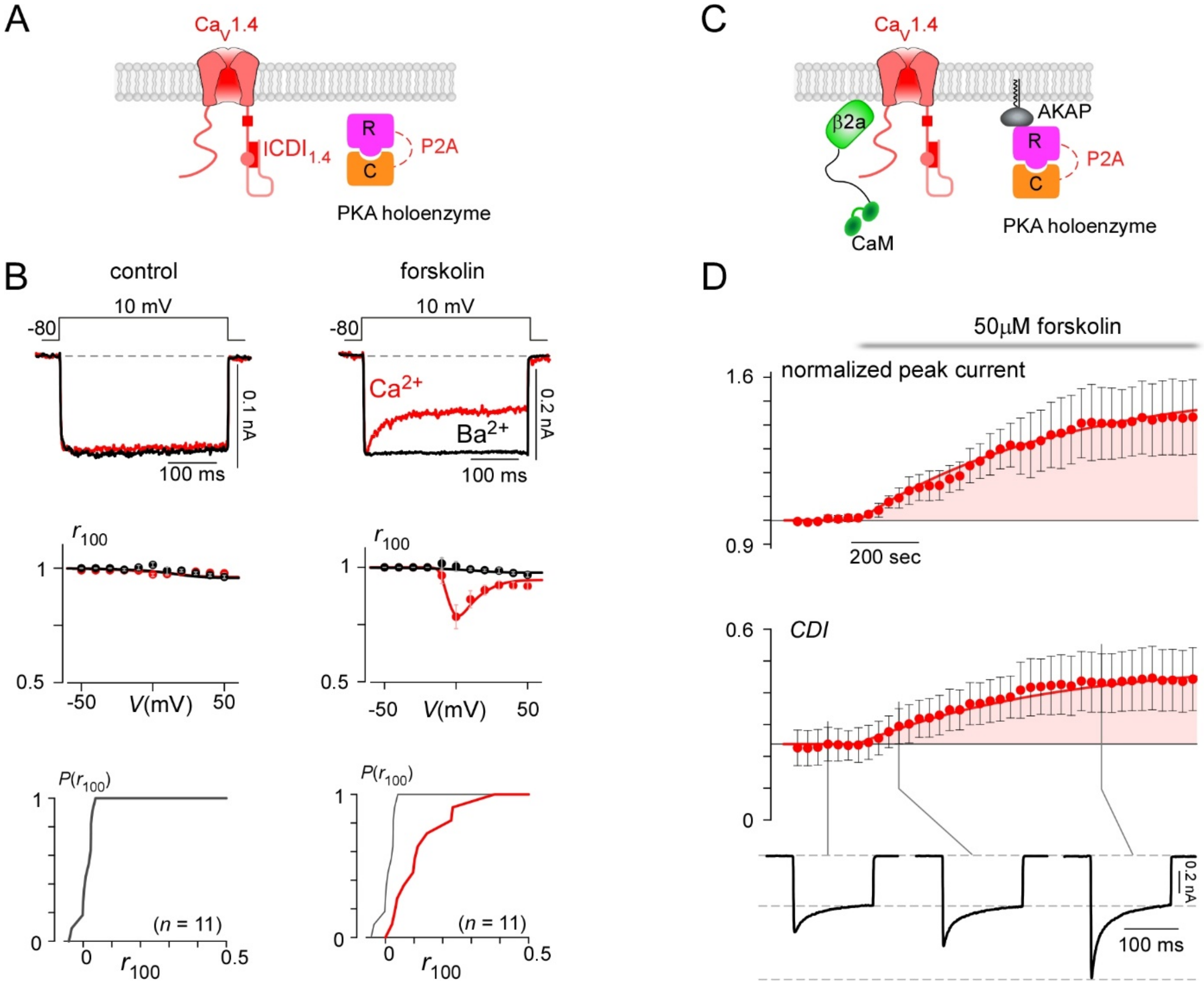
A
CaV1.4
ICDI1.4
R
C
P2A
PKA holoenzyme
B
control
forskolin
-80
10 mV
Ca2+
Ba2+
0.1 nA
0.2 nA
100 ms
r100
1
0.5
-50
V(mV)
50
P(r100)
0
(n = 11)
C
β2a
CaM
AKAP
D
50μM forskolin
normalized peak current
1.6
0.9
200 sec
CDI
0.6
0

Figure 27. PKA regulation of full-length wild-type Ca$_V$1.4 channels in HEK293 cells. (**A**) Schematic of wild-type Ca$_V$1.4 channels with PKA holoenzyme. (**B**) No CDI at baseline (left), however incubation in 50 μM forskolin induces clear CDI (right). Format as in **Figure 23B, D**. (**C**) Schematic of Ca$_V$1.4 and PKA holoenzyme, AKAP79 and β_{2a} tethered CaM. (**D**) Time courses for normalized peak current (top) and CDI (middle) from whole-cell Ca^{2+} currents in response to 50 μM forskolin. Currents are evoked every 30 seconds by 20 mV depolarizations. Currents were normalized to baseline and CDI was measured as 1 - r_{100}. Error bars indicated +/- SEM (n = 4 cells). Corresponding current waveforms displayed below.

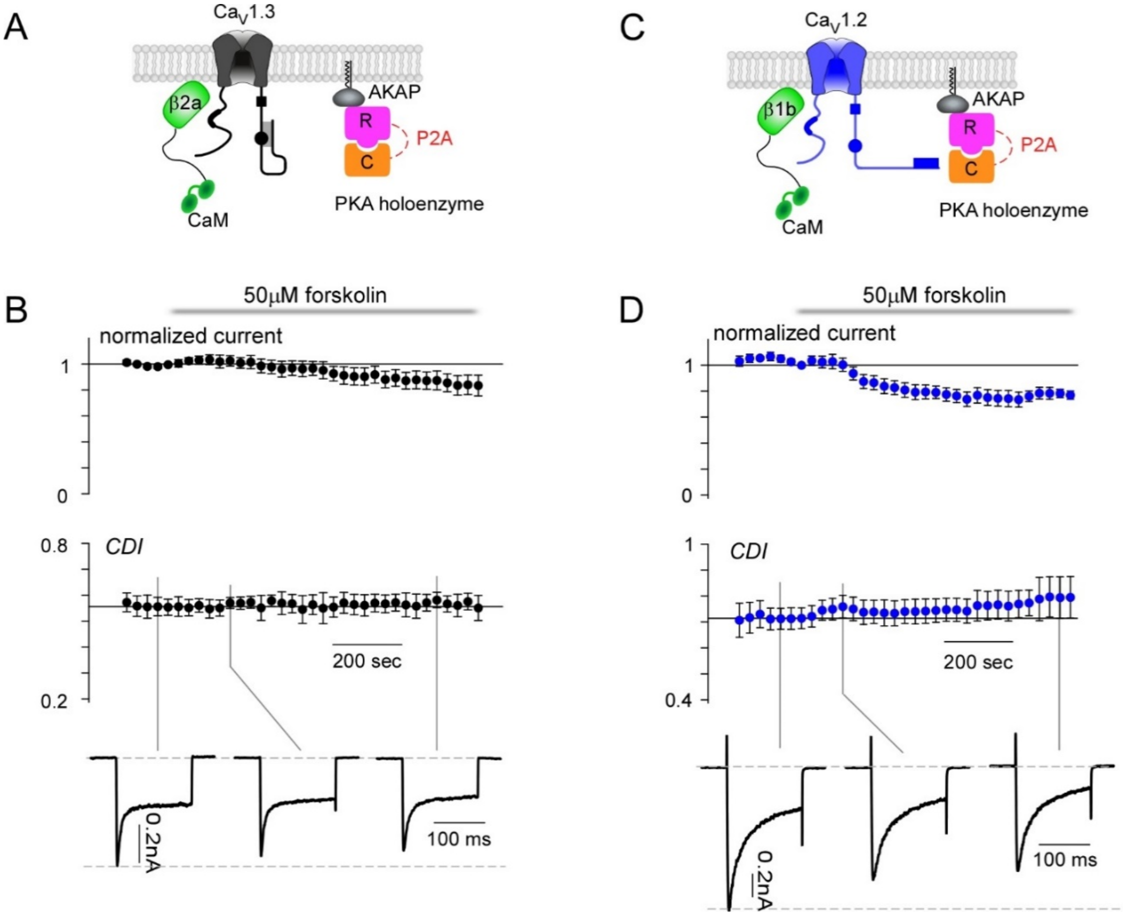
A
$\mathrm{Ca_V}1.3$
β2a
CaM
AKAP
R
C
P2A
PKA holoenzyme
B
50μM forskolin
normalized current
1
0
CDI
0.8
0.2
200 sec
0.2nA
100 ms
C
$\mathrm{Ca_V}1.2$
β1b
CaM
AKAP
R
C
P2A
PKA holoenzyme
D
50μM forskolin
normalized current
1
0
CDI
1
0.4
200 sec
0.2nA
100 ms

Figure 28. PKA does not regulate the IQ and ICDI interaction in Ca$_V$1.3 and Ca$_V$1.2.

(**A**) Schematic of co-expression of Ca$_V$1.3 with PKA holoenzyme, AKAP79 and β_{2a} tethered CaM which allowed longer whole cell patching without loss of PKA or CaM. (**B**) Time course of normalized peak current (top) and CDI (bottom) in response to the addition of 50 μM forskolin (*n* = 5 cells). Corresponding current waveforms are displayed below. (**C**) Schematic of co-expression of Ca$_V$1.2 with PKA holoenzyme, AKAP79 and β_{1b} tethered CaM which allowed longer whole cell patching without loss of PKA or CaM. (**D**) Time course of normalized peak current (top) and CDI (bottom) in response to the addition of 50 μM forskolin (*n* = 4 cells). Corresponding current waveforms are displayed below.

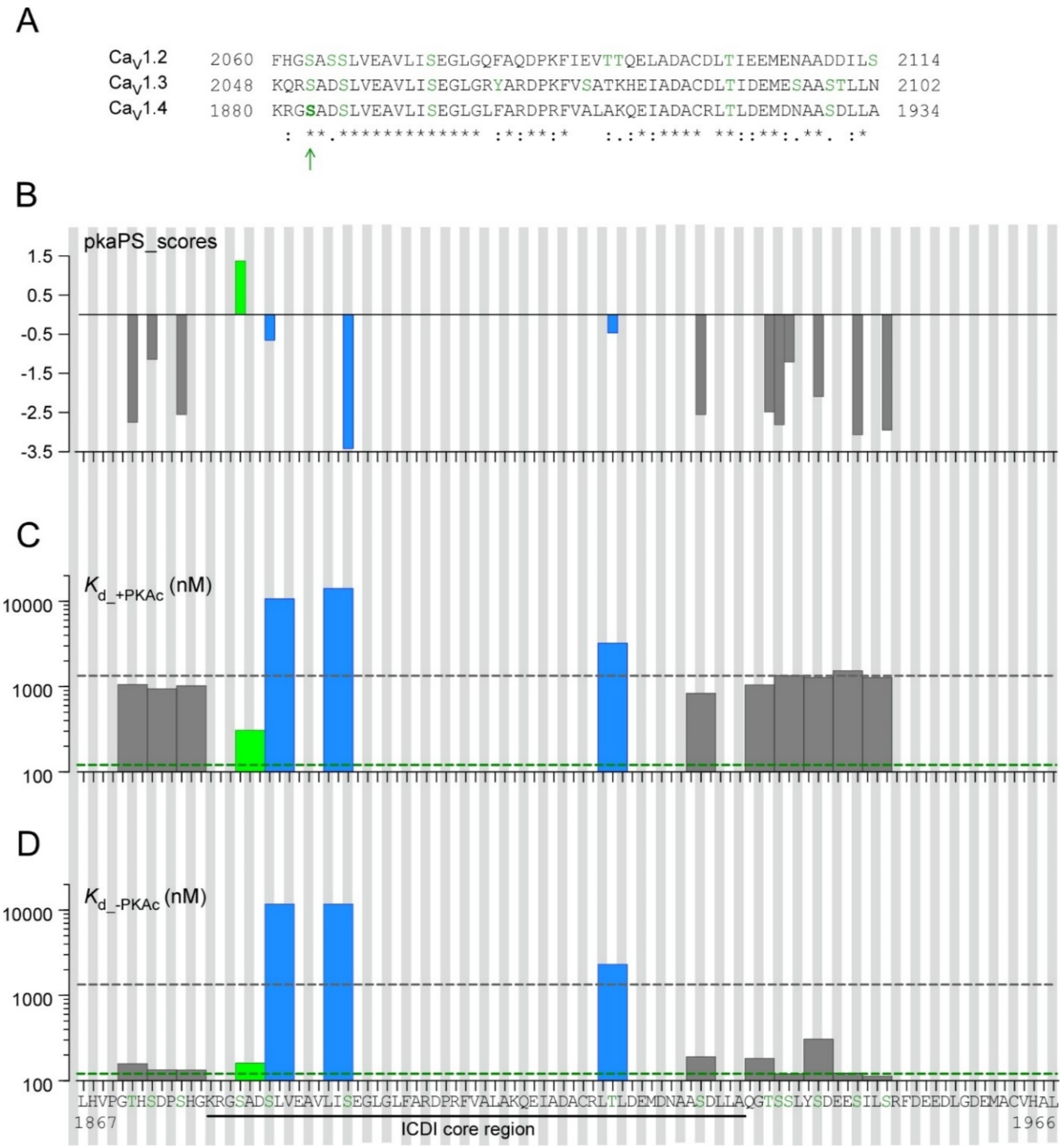
A
CaV1.2 2060 FHGSASSLVEAVLISEGLGQFAQDPKFIEVTTQELADACDLTIEEMENAADDILS 2114
CaV1.3 2048 KQRSADSLVEAVLISEGLGRYARDPKFVSATKHEIADACDLTIDEMESAASTLLN 2102
CaV1.4 1880 KRGSADSLVEAVLISEGLGLFARDPRFVALAKQEIADACRLTLDEMDNAASDLLA 1934
: **.************* :*:**:* :.:*:**** **::**:.**. :*
↑
B
pkaPS_scores
1.5
0.5
-0.5
-1.5
-2.5
-3.5
C
K d_+PKAc (nM)
10000
1000
100
D
K d_-PKAc (nM)
10000
1000
100
LHVPGTHSDPSHGKRGSADSLVEAVLISEGLGLFARDPRFVALAKQEIADACRLTLDEMDNAASDLLAQGTSSLYSDEESILSRFDEEDLGDEMACVHAL
1867
1966
ICDI core region

Figure 29. Identifying the PKA phosphorylation site on Ca$_V$1.4.

(**A**) Sequence alignment of the core region of ICDI modules (identified by alanine scanning in previous studies[89]) from Ca$_V$1.2, 1.3 and 1.4, with consensus symbols labelled underneath. Potential phosphorylation sites (STY) were colored green. The arrow indicates S1883. (**B**) pkaPS scores of potential phosphorylation sites in ICDI$_{1.4}$. The corresponding sequence is displayed at the bottom on the x-axis in panel **D**, S1883 (green) has the highest score. (**C**) Dissociation constants ($K_{\mathrm{d_+PKAc}}$) measured by FRET two-hybrid assays between Venus-IQ-A$_{1.3}$ peptide and cereulan-ICDI$_{1.4}$ peptides in the presence of overexpressed PKAc (**Figure 31B**, right). Every three contiguous residues within ICDI$_{1.4}$ (corresponding to the bottom sequence in **D**) were systematically substituted by alanines[89]. The green dashed line marks the dissociation constant between Venus-IQ-A$_{1.3}$ peptide and wild-type cereulan-ICDI$_{1.4}$ peptides without overexpressing PKAc. The gray dashed line marks the dissociation constant between Venus-IQ-A$_{1.3}$ and wild-type cereulan-ICDI$_{1.4}$ peptides with overexpression of PKAc. With SAD1883AAA mutations (green), overexpressing PKAc fails to increase the dissociation constant of the two peptides (compare to **D**, green bar) indicating that S1883 is likely the PKA phosphorylation site. (**D**) Dissociation constants ($K_{\mathrm{d\_-PKAc}}$) measured by FRET two-hybrid assays between Venus-IQ-A$_{1.3}$ and cereulan-ICDI$_{1.4}$ peptides without overexpressed PKAc (**Figure 31B**, left). The green and gray dashed lines are the same as in **C**. The corresponding ICDI$_{1.4}$ sequence is labeled under the x-axis. The core region[89] for IQ interaction is marked by the bar below the sequence. Mutations in three constructs (blue bars) reduced the dissociation constants of IQ/ICDI interaction even at basal PKA levels.

A

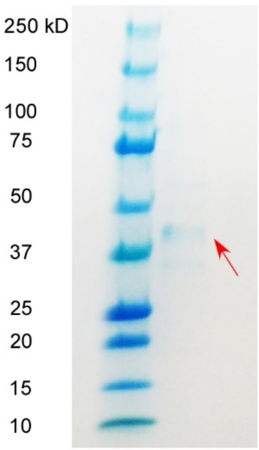

B

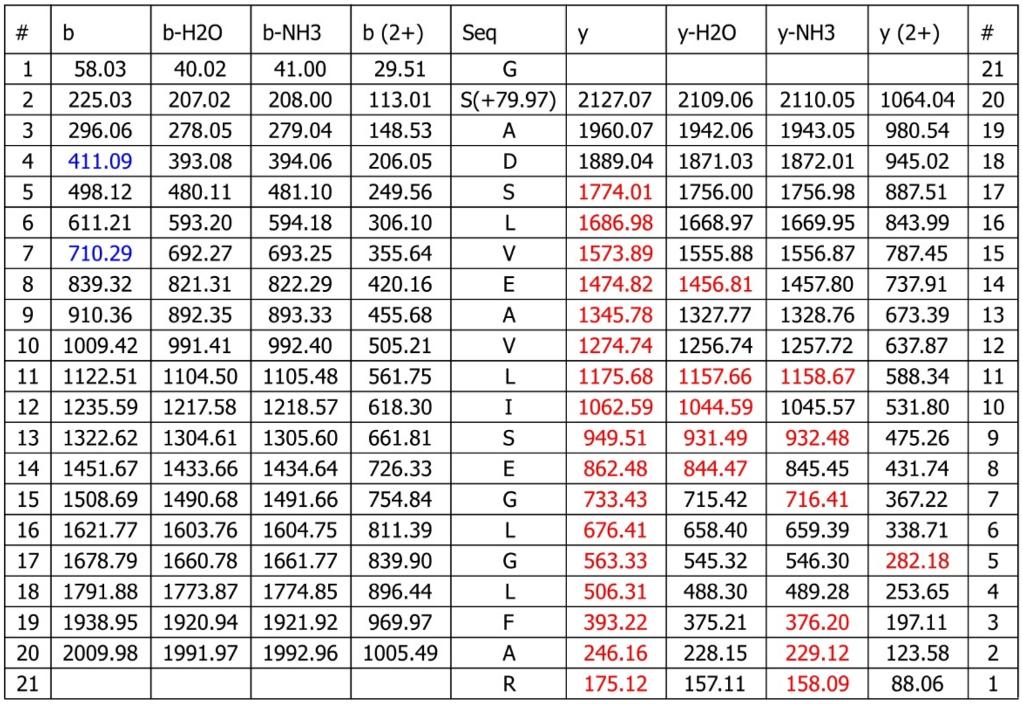

#	b	b-H2O	b-NH3	b (2+)	Seq	y	y-H2O	y-NH3	y (2+)	#
1	58.03	40.02	41.00	29.51	G					21
2	225.03	207.02	208.00	113.01	S(+79.97)	2127.07	2109.06	2110.05	1064.04	20
3	296.06	278.05	279.04	148.53	A	1960.07	1942.06	1943.05	980.54	19
4	411.09	393.08	394.06	206.05	D	1889.04	1871.03	1872.01	945.02	18
5	498.12	480.11	481.10	249.56	S	1774.01	1756.00	1756.98	887.51	17
6	611.21	593.20	594.18	306.10	L	1686.98	1668.97	1669.95	843.99	16
7	710.29	692.27	693.25	355.64	V	1573.89	1555.88	1556.87	787.45	15
8	839.32	821.31	822.29	420.16	E	1474.82	1456.81	1457.80	737.91	14
9	910.36	892.35	893.33	455.68	A	1345.78	1327.77	1328.76	673.39	13
10	1009.42	991.41	992.40	505.21	V	1274.74	1256.74	1257.72	637.87	12
11	1122.51	1104.50	1105.48	561.75	L	1175.68	1157.66	1158.67	588.34	11
12	1235.59	1217.58	1218.57	618.30	I	1062.59	1044.59	1045.57	531.80	10
13	1322.62	1304.61	1305.60	661.81	S	949.51	931.49	932.48	475.26	9
14	1451.67	1433.66	1434.64	726.33	E	862.48	844.47	845.45	431.74	8
15	1508.69	1490.68	1491.66	754.84	G	733.43	715.42	716.41	367.22	7
16	1621.77	1603.76	1604.75	811.39	L	676.41	658.40	659.39	338.71	6
17	1678.79	1660.78	1661.77	839.90	G	563.33	545.32	546.30	282.18	5
18	1791.88	1773.87	1774.85	896.44	L	506.31	488.30	489.28	253.65	4
19	1938.95	1920.94	1921.92	969.97	F	393.22	375.21	376.20	197.11	3
20	2009.98	1991.97	1992.96	1005.49	A	246.16	228.15	229.12	123.58	2
21					R	175.12	157.11	158.09	88.06	1

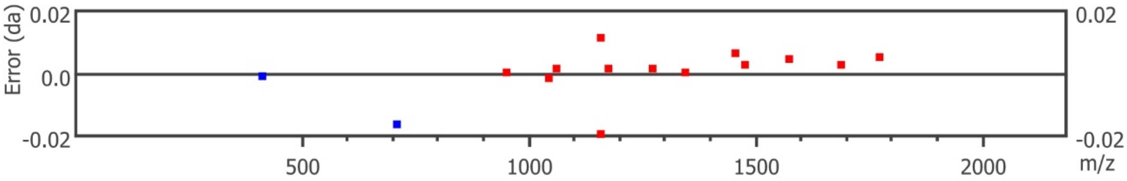

Figure 30. Additional information for mass spectroscopy experiments.

(**A**) Coomassie blue stained SDS-PAGE gel loaded with purified double-histidine-labeled Cerulean-ICDI$_{1.4}$ peptides (expected molecular weight: 40.8kD). The red arrow indicates the band analyzed by mass spectroscopy. (**B**) Ion table and error map of the spectra in **Figure 31A**.

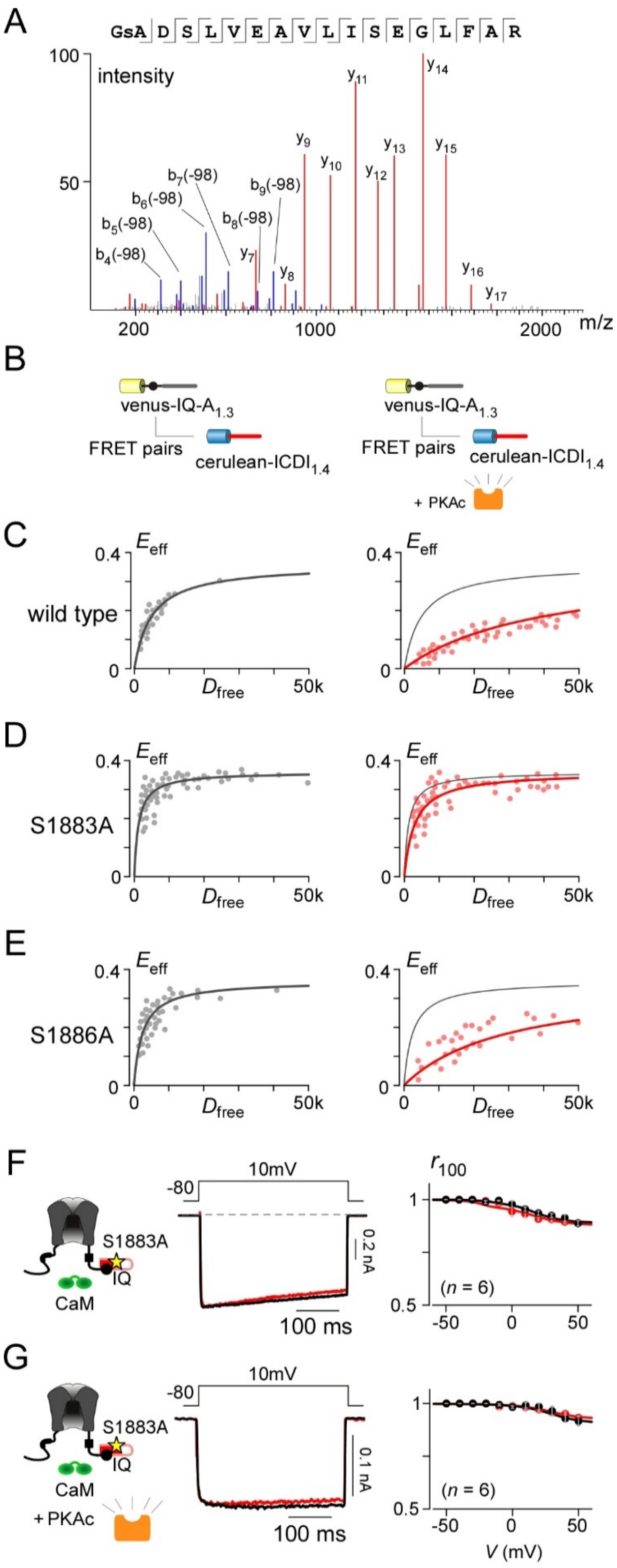A
GsA D S L V E A V L I S E G L F A R
100
intensity
50
y11
y14
y9
y10
y12
y13
y15
b7(-98)
b6(-98)
b9(-98)
b5(-98)
b8(-98)
b4(-98)
y7
y8
y16
y17
200
1000
2000
m/z
B
venus-IQ-A1.3
FRET pairs
cerulean-ICDI1.4
venus-IQ-A1.3
FRET pairs
cerulean-ICDI1.4
+ PKAc
C
Eeff
0.4
wild type
0
0
Dfree
50k
D
S1883A
E
S1886A
F
S1883A
IQ
CaM
-80
10mV
0.2 nA
100 ms
r100
1
0.5
(n = 6)
-50
0
50
G
S1883A
IQ
CaM
+ PKAc
-80
10mV
0.1 nA
100 ms
1
0.5
(n = 6)
-50
0
50
V (mV)

Figure 31. Identification of the PKA phosphorylation site within ICDI$_{1.4}$.

(**A**) The mass spectra of an ICDI$_{1.4}$ peptide, showing phosphorylation at S1883. (**B**) High-throughput FRET binding assays (**C**-**E**) between Venus-IQ-A$_{1.3}$ and Cerulean-ICDI$_{1.4}$ demonstrating the modulation of binding due to PKAc overexpression. (**C**) Overexpression of PKAc reduced binding between IQ-A$_{1.3}$ and wild-type ICDI$_{1.4}$. (**D**) Overexpression of PKAc did not affect binding between IQ-A$_{1.3}$ and ICDI$_{1.4}$ harboring a S1883A mutation. (**E**) Overexpression of PKAc reduced binding between IQ-A$_{1.3}$ and ICDI$_{1.4}$ harboring a S1886A mutation. (**F**) Similar to wild-type Cav1.3$_{S/1.4DCT}$ channels (**Figure 20F**), Cav1.3$_{S/1.4DCT}$ channels containing the S1883A mutation had minimal CDI. (**G**) Unlike wild-type Cav1.3$_{S/1.4DCT}$ (**Figure 20G**), Cav1.3$_{S/1.4DCT}$ channels with the S1883A mutation did not exhibit increased CDI with overexpression of PKAc.

Reference

1. Alseikhan, B.A., DeMaria, C.D., Colecraft, H.M. & Yue, D.T. Engineered calmodulins reveal the unexpected eminence of Ca2+ channel inactivation in controlling heart excitation. *Proc Natl Acad Sci U S A* **99**, 17185-90 (2002).
2. Greer, P.L. & Greenberg, M.E. From synapse to nucleus: calcium-dependent gene transcription in the control of synapse development and function. *Neuron* **59**, 846-60 (2008).
3. Xu, J. & Wu, L.G. The decrease in the presynaptic calcium current is a major cause of short-term depression at a calyx-type synapse. *Neuron* **46**, 633-45 (2005).
4. Ben-Johny, M. et al. Conservation of Ca2+/calmodulin regulation across Na and Ca2+ channels. *Cell* **157**, 1657-70 (2014).
5. Mori, M.X., Erickson, M.G. & Yue, D.T. Functional stoichiometry and local enrichment of calmodulin interacting with Ca2+ channels. *Science* **304**, 432-5 (2004).
6. Adams, P.J., Ben-Johny, M., Dick, I.E., Inoue, T. & Yue, D.T. Apocalmodulin itself promotes ion channel opening and Ca(2+) regulation. *Cell* **159**, 608-22 (2014).
7. Erickson, M.G., Liang, H., Mori, M.X. & Yue, D.T. FRET two-hybrid mapping reveals function and location of L-type Ca2+ channel CaM preassociation. *Neuron* **39**, 97-107 (2003).
8. Liu, X., Yang, P.S., Yang, W. & Yue, D.T. Enzyme-inhibitor-like tuning of Ca(2+) channel connectivity with calmodulin. *Nature* **463**, 968-72 (2010).
9. Singh, A. et al. C-terminal modulator controls Ca^{2+}-dependent gating of Cav1.4 L-type Ca^{2+} channels. *Nat Neurosci* **9**, 1108-16 (2006).
10. Haeseleer, F., Williams, B. & Lee, A. Characterization of C-terminal splice variants of Cav1.4 Ca2+ channels in human retina. *J Biol Chem* (2016).
11. Yang, P.S. et al. Switching of Ca^{2+}-dependent inactivation of Cav1.3 channels by calcium binding proteins of auditory hair cells. *J. Neurosci.* **26**, 10677-89 (2006).
12. Kollmar, R., Fak, J., Montgomery, L.G. & Hudspeth, A.J. Hair cell-specific splicing of mRNA for the alpha1D subunit of voltage-gated Ca2+ channels in the chicken's cochlea. *Proc Natl Acad Sci U S A* **94**, 14889-93 (1997).
13. Strom, T.M. et al. An L-type calcium-channel gene mutated in incomplete X-linked congenital stationary night blindness. *Nat Genet* **19**, 260-3 (1998).
14. Erickson, M.G., Alseikhan, B.A., Peterson, B.Z. & Yue, D.T. Preassociation of calmodulin with voltage-gated Ca(2+) channels revealed by FRET in single living cells. *Neuron* **31**, 973-85 (2001).
15. Dunlap, K. Calcium channels are models of self-control. *J Gen Physiol* **129**, 379-83 (2007).
16. Limpitikul, W.B. et al. Calmodulin mutations associated with long QT syndrome prevent inactivation of cardiac L-type Ca(2+) currents and promote proarrhythmic behavior in ventricular myocytes. *J Mol Cell Cardiol* **74**, 115-24 (2014).

17. Evans, R.M. & Zamponi, G.W. Presynaptic Ca2+ channels--integration centers for neuronal signaling pathways. *Trends Neurosci* **29**, 617-24 (2006).
18. Bradley, P., Misura, K.M. & Baker, D. Toward high-resolution de novo structure prediction for small proteins. *Science* **309**, 1868-71 (2005).
19. Schneidman-Duhovny, D., Inbar, Y., Nussinov, R. & Wolfson, H.J. PatchDock and SymmDock: servers for rigid and symmetric docking. *Nucleic Acids Res* **33**, W363-W367 (2005).
20. Xu, W. & Lipscombe, D. Neuronal Ca(V)1.3alpha(1) L-type channels activate at relatively hyperpolarized membrane potentials and are incompletely inhibited by dihydropyridines. *J Neurosci* **21**, 5944-51 (2001).
21. Wei, X.Y. et al. Heterologous Regulation of the Cardiac Ca2+ Channel-Alpha-1 Subunit by Skeletal-Muscle Beta-Subunit and Gamma-Subunits - Implications for the Structure of Cardiac L-Type Ca2+ Channels. *J Biol Chem* **266**, 21943-21947 (1991).
22. Peterson, B.Z., DeMaria, C.D., Adelman, J.P. & Yue, D.T. Calmodulin is the Ca^{2+} sensor for Ca2+ -dependent inactivation of L- type calcium channels. *Neuron* **22**, 549-58 (1999).
23. Tomlinson, W.J. et al. Functional properties of a neuronal class C L-type calcium channel. *Neuropharmacology* **32**, 1117-1126 (1993).
24. Rizzo, M.A., Springer, G.H., Granada, B. & Piston, D.W. An improved cyan fluorescent protein variant useful for FRET. *Nat Biotechnol* **22**, 445-9 (2004).
25. Nagai, T. et al. A variant of yellow fluorescent protein with fast and efficient maturation for cell-biological applications. *Nat Biotechnol* **20**, 87-90 (2002).
26. Kim, D.E., Chivian, D. & Baker, D. Protein structure prediction and analysis using the Robetta server. *Nucleic Acids Res* **32**, W526-31 (2004).
27. Bazzazi, H., Ben Johny, M., Adams, P.J., Soong, T.W. & Yue, D.T. Continuously tunable Ca(2+) regulation of RNA-edited CaV1.3 channels. *Cell Rep* **5**, 367-77 (2013).
28. Hulme, J.T., Yarov-Yarovoy, V., Lin, T.W., Scheuer, T. & Catterall, W.A. Autoinhibitory control of the CaV1.2 channel by its proteolytically processed distal C-terminal domain. *J Physiol* **576**, 87-102 (2006).
29. Fuller, M.D., Emrick, M.A., Sadilek, M., Scheuer, T. & Catterall, W.A. Molecular Mechanism of Calcium Channel Regulation in the Fight-or-Flight Response. *Sci Signal* **3**, ra70-ra70 (2010).
30. Gomez-Ospina, N., Tsuruta, F., Barreto-Chang, O., Hu, L. & Dolmetsch, R. The C terminus of the L-type voltage-gated calcium channel Ca(V)1.2 encodes a transcription factor. *Cell* **127**, 591-606 (2006).
31. Schroder, E., Byse, M. & Satin, J. L-Type Calcium Channel C Terminus Autoregulates Transcription. *Circ Res* **104**, 1373-U238 (2009).
32. Liang, H. et al. Unified mechanisms of Ca^{2+} regulation across the Ca^{2+} channel family. *Neuron* **39**, 951-60 (2003).
33. Hulme, J.T. et al. Sites of proteolytic processing and noncovalent association of the distal C-terminal domain of CaV1.1 channels in skeletal muscle. *Proc Natl Acad Sci U S A* **102**, 5274-5279 (2005).

34. Bock, G. et al. Functional Properties of a Newly Identified C-terminal Splice Variant of Cav1.3 L-type Ca2+ Channels. *J Biol Chem* **286**, 42736-48 (2011).
35. Mori, M.X., Vander Kooi, C.W., Leahy, D.J. & Yue, D.T. Crystal structure of the CaV2 IQ domain in complex with Ca2+/calmodulin: high-resolution mechanistic implications for channel regulation by Ca2+. *Structure* **16**, 607-20 (2008).
36. Kim, E.Y. et al. Structures of CaV2 Ca2+/CaM-IQ domain complexes reveal binding modes that underlie calcium-dependent inactivation and facilitation. *Structure* **16**, 1455-67 (2008).
37. Chaudhuri, D. et al. Alternative splicing as a molecular switch for Ca2+/calmodulin-dependent facilitation of P/Q-type Ca2+ channels. *J Neurosci* **24**, 6334-42 (2004).
38. Striessnig, J., Bolz, H.J. & Koschak, A. Channelopathies in Cav1.1, Cav1.3, and Cav1.4 voltage-gated L-type Ca2+ channels. *Pflugers Arch* **460**, 361-74 (2010).
39. Johny, M.B., Yang, P.S. & Yue, D.T. Molecular Events Beyond apoCAM Preassociation in the CAM Regulation of Cav1.3 Channels. *Biophys J* **100**, 529a-529a (2011).
40. Ben Johny, M., Yang, P.S., Bazzazi, H. & Yue, D.T. Dynamic switching of calmodulin interactions underlies Ca2+ regulation of CaV1.3 channels. *Nat Commun* **4**, 1717 (2013).
41. Dick, I.E. et al. A modular switch for spatial Ca^{2+} selectivity in the calmodulin regulation of Cav channels. *Nature* **451**, 830-834 (2008).
42. Yang, P.S., Johny, M.B. & Yue, D.T. Allostery in Ca(2)(+) channel modulation by calcium-binding proteins. *Nat Chem Biol* **10**, 231-8 (2014).
43. Ben Johny, M., Yue, D.N. & Yue, D.T. A Novel FRET-Based Assay Reveals 1:1 Stoichiometry of Apocalmodulin Binding Across Voltage-Gated Ca and Na Ion Channels (abstr.). *Biophys J* **102**, 125a-126a (2012).
44. Aoki, K., Kamioka, Y. & Matsuda, M. Fluorescence resonance energy transfer imaging of cell signaling from in vitro to in vivo: basis of biosensor construction, live imaging, and image processing. *Dev Growth Differ* **55**, 515-22 (2013).
45. Nagai, T., Yamada, S., Tominaga, T., Ichikawa, M. & Miyawaki, A. Expanded dynamic range of fluorescent indicators for Ca(2+) by circularly permuted yellow fluorescent proteins. *Proc Natl Acad Sci U S A* **101**, 10554-9 (2004).
46. Tadross, M.R., Park, S.A., Veeramani, B. & Yue, D.T. Robust approaches to quantitative ratiometric FRET imaging of CFP/YFP fluorophores under confocal microscopy. *J Microsc* **233**, 192-204 (2009).
47. Sekar, R.B. et al. Lentiviral vector-mediated expression of GFP or Kir2.1 alters the electrophysiology of neonatal rat ventricular myocytes without inducing cytotoxicity. *Am J Physiol Heart Circ Physiol* **293**, H2757-70 (2007).
48. Joshi-Mukherjee, R. et al. Structural and functional plasticity in long-term cultures of adult ventricular myocytes. *J Mol Cell Cardiol* **65**, 76-87 (2013).
49. Lee, S.R., Sang, L. & Yue, D.T. Uncovering Aberrant Mutant PKA Function with Flow Cytometric FRET. *Cell Rep* **14**, 3019-29 (2016).

50. Findeisen, F., Rumpf, C.H. & Minor, D.L., Jr. Apo states of calmodulin and CaBP1 control CaV1 voltage-gated calcium channel function through direct competition for the IQ domain. *J Mol Biol* **425**, 3217-34 (2013).
51. Grunberg, R. et al. Engineering of weak helper interactions for high-efficiency FRET probes. *Nat Methods* **10**, 1021-7 (2013).
52. Pham, E., Chiang, J., Li, I., Shum, W. & Truong, K. A computational tool for designing FRET protein biosensors by rigid-body sampling of their conformational space. *Structure* **15**, 515-23 (2007).
53. Tsien, R.W. Calcium channels in excitable cell membranes. *Annu Rev Physiol* **45**, 341-358 (1983).
54. Kang, S. et al. CaV1.3-selective L-type calcium channel antagonists as potential new therapeutics for Parkinson's disease. *Nat Commun* **3**, 1146 (2012).
55. Ortner, N.J. et al. Pyrimidine-2,4,6-triones are a new class of voltage-gated L-type Ca2+ channel activators. *Nat Commun* **5**, 3897 (2014).
56. Huang, H. et al. Modest CaV1.342-selective inhibition by compound 8 is beta-subunit dependent. *Nat Commun* **5**, 4481 (2014).
57. Chan, C.S. et al. 'Rejuvenation' protects neurons in mouse models of Parkinson's disease. *Nature* **447**, 1081-6 (2007).
58. Kafri, T., van Praag, H., Gage, F.H. & Verma, I.M. Lentiviral vectors: regulated gene expression. *Mol Ther* **1**, 516-21 (2000).
59. Erickson, M.G., Moon, D.L. & Yue, D.T. DsRed as a potential FRET partner with CFP and GFP. *Biophys. J.* **85**, 599-611 (2003).
60. Dijon, M., Torne-Celer, C., Moreau, T., Tonnelle, C. & Chabannon, C. Expression and recombination of the EGFP and EYFP genes in lentiviral vectors carrying two heterologous promoters. *Cytotherapy* **7**, 417-26 (2005).
61. Pollard, T.D. A guide to simple and informative binding assays. *Mol Biol Cell* **21**, 4061-7 (2010).
62. Yamamoto, M., Okumura, S., Schwencke, C., Sadoshima, J. & Ishikawa, Y. High efficiency gene transfer by multiple transfection protocol. *Histochem J* **31**, 241-3 (1999).
63. Bruckner, A., Polge, C., Lentze, N., Auerbach, D. & Schlattner, U. Yeast two-hybrid, a powerful tool for systems biology. *Int J Mol Sci* **10**, 2763-88 (2009).
64. Vos, Q., Klasen, E.A. & Haaijman, J.J. The effect of divalent and univalent binding on antibody titration curves in solid-phase ELISA. *J Immunol Methods* **103**, 47-54 (1987).
65. Larsson, A. Divalent binding of monoclonal antibody to a cell surface antigen. Modelling of equilibrium data. *Mol Immunol* **26**, 735-9 (1989).
66. Reynolds, J.A. Interaction of divalent antibody with cell surface antigens. *Biochemistry* **18**, 264-9 (1979).
67. Arkin, M.R. & Wells, J.A. Small-molecule inhibitors of protein-protein interactions: progressing towards the dream. *Nat Rev Drug Discov* **3**, 301-17 (2004).
68. Arkin, M.R., Tang, Y. & Wells, J.A. Small-molecule inhibitors of protein-protein interactions: progressing toward the reality. *Chem Biol* **21**, 1102-14 (2014).

69. Arkin, M.R., Glicksman, M.A., Fu, H., Havel, J.J. & Du, Y. Inhibition of Protein-Protein Interactions: Non-Cellular Assay Formats. in *Assay Guidance Manual* (eds. Sittampalam, G.S. et al.) (Bethesda (MD), 2004).
70. An, W.F. & Tolliday, N.J. Introduction: cell-based assays for high-throughput screening. *Methods Mol Biol* **486**, 1-12 (2009).
71. Chen, Q. et al. A yeast two-hybrid technology-based system for the discovery of PPARgamma agonist and antagonist. *Anal Biochem* **335**, 253-9 (2004).
72. Poe, J.A., Vollmer, L., Vogt, A. & Smithgall, T.E. Development and validation of a high-content bimolecular fluorescence complementation assay for small-molecule inhibitors of HIV-1 Nef dimerization. *J Biomol Screen* **19**, 556-65 (2014).
73. Song, Y., Madahar, V. & Liao, J. Development of FRET assay into quantitative and high-throughput screening technology platforms for protein-protein interactions. *Ann Biomed Eng* **39**, 1224-34 (2011).
74. Nishi, H., Hashimoto, K. & Panchenko, A.R. Phosphorylation in protein-protein binding: effect on stability and function. *Structure* **19**, 1807-15 (2011).
75. DeJongh, K.S. et al. Specific phosphorylation of a site in the full-length form of the alpha 1 subunit of the cardiac L-type calcium channel by adenosine 3',5'-cyclic monophosphate-dependent protein kinase. *Biochemistry* **35**, 10392-10402 (1996).
76. Lemke, T. et al. Unchanged beta-adrenergic stimulation of cardiac L-type calcium channels in Ca v 1.2 phosphorylation site S1928A mutant mice. *J Biol Chem* **283**, 34738-44 (2008).
77. Wang, P., Wu, Y.L., Zhou, T.H., Sun, Y. & Pei, G. Identification of alternative splicing variants of the beta subunit of human Ca(2+)/calmodulin-dependent protein kinase II with different activities. *FEBS Lett* **475**, 107-10 (2000).
78. Hofmann, F., Flockerzi, V., Kahl, S. & Wegener, J.W. L-type CaV1.2 calcium channels: from in vitro findings to in vivo function. *Physiol Rev* **94**, 303-26 (2014).
79. Anderson, M.E. Why has it taken so long to learn what we still don't know? *Circ Res* **113**, 840-2 (2013).
80. Weiss, S., Oz, S., Benmocha, A. & Dascal, N. Regulation of cardiac L-type Ca(2)(+) channel CaV1.2 via the beta-adrenergic-cAMP-protein kinase A pathway: old dogmas, advances, and new uncertainties. *Circ Res* **113**, 617-31 (2013).
81. Subramanyam, P. et al. Manipulating L-type calcium channels in cardiomyocytes using split-intein protein transsplicing. *Proc Natl Acad Sci U S A* **110**, 15461-6 (2013).
82. Chen, X. et al. PKC-dependent Phosphorylation of the H1 Histamine Receptor Modulates TRPC6 Activity. *Cells* **3**, 247-57 (2014).
83. Miriyala, J., Nguyen, T., Yue, D.T. & Colecraft, H.M. Role of CaVbeta subunits, and lack of functional reserve, in protein kinase A modulation of cardiac CaV1.2 channels. *Circ Res* **102**, e54-64 (2008).

84. Ben-Johny, M. et al. Towards a unified theory of calmodulin regulation (calmodulation) of voltage-gated calcium and sodium channels. *Curr Mol Pharmacol* **8**, 188-205 (2015).
85. Tan, B.Z. et al. Functional characterization of alternative splicing in the C terminus of L-type CaV1.3 channels. *J Biol Chem* **286**, 42725-35 (2011).
86. Tan, G.M., Yu, D., Wang, J. & Soong, T.W. Alternative Splicing at C-terminus of CaV1.4 Calcium Channel Modulates Calcium-Dependent Inactivation, Activation Potential and Current Density. *J Biol Chem* (2012).
87. Perez-Reyes, E. et al. Cloning and expression of a cardiac/brain beta subunit of the L- type calcium channel. *J.Biol.Chem.* **267**, 1792-1797 (1992).
88. Pragnell, M., Sakamoto, J., Jay, S.D. & Campbell, K.P. Cloning and tissue-specific expression of the brain calcium channel beta-subunit. *FEBS Lett* **291**, 253-8 (1991).
89. Sang, L., Bazzazi, H., Johny, M.B. & Yue, D.T. Resolving the Grip of the Distal Carboxy Tail on the Proximal Calmodulatory Region of CaV Channels. *Biophys J* **102**, 126a-126a (2012).
90. Wahl-Schott, C. et al. Switching off calcium-dependent inactivation in L-type calcium channels by an autoinhibitory domain. *Proc Natl Acad Sci U S A* **103**, 15657-62 (2006).
91. Colecraft, H.M. et al. Novel functional properties of Ca(2+) channel beta subunits revealed by their expression in adult rat heart cells. *J Physiol* **541**, 435-52 (2002).
92. McRory, J.E. et al. The CACNA1F gene encodes an L-type calcium channel with unique biophysical properties and tissue distribution. *J Neurosci* **24**, 1707-18 (2004).
93. Kandel, E.R. The molecular biology of memory: cAMP, PKA, CRE, CREB-1, CREB-2, and CPEB. *Mol Brain* **5**, 14 (2012).
94. Bazzazi, H. et al. Novel fluorescence resonance energy transfer-based reporter reveals differential calcineurin activation in neonatal and adult cardiomyocytes. *J Physiol* (2015).
95. Depry, C., Allen, M.D. & Zhang, J. Visualization of PKA activity in plasma membrane microdomains. *Mol Biosyst* **7**, 52-8 (2011).
96. Tadross, M.R., Ben Johny, M. & Yue, D.T. Molecular endpoints of Ca2+/calmodulin- and voltage-dependent inactivation of Ca(v)1.3 channels. *J Gen Physiol* **135**, 197-215 (2010).
97. Neuberger, G., Schneider, G. & Eisenhaber, F. pkaPS: prediction of protein kinase A phosphorylation sites with the simplified kinase-substrate binding model. *Biol Direct* **2**, 1 (2007).
98. von Gersdorff, H. & Matthews, G. Calcium-dependent inactivation of calcium current in synaptic terminals of retinal bipolar neurons. *J Neurosci* **16**, 115-22 (1996).
99. Witkovsky, P. Dopamine and retinal function. *Doc Ophthalmol* **108**, 17-40 (2004).
100. Manglapus, M.K., Iuvone, P.M., Underwood, H., Pierce, M.E. & Barlow, R.B. Dopamine mediates circadian rhythms of rod-cone dominance in the Japanese quail retina. *J Neurosci* **19**, 4132-41 (1999).

101. Ribelayga, C., Wang, Y. & Mangel, S.C. Dopamine mediates circadian clock regulation of rod and cone input to fish retinal horizontal cells. *J Physiol* **544**, 801-16 (2002).

Curriculum Vitae

Lingjie Sang 5/31/2016

Education

The Johns Hopkins University, Baltimore, MD

Ph.D. in Biomedical Engineering May 2016 (Expected)

(Advisor: David T. Yue, M.D., Ph.D.)

M.S.E. in Computer Science May 2016

Peking University, Beijing, China

B.E. in Mechanical Engineering July 2008

(Advisor: Huaiqiu Zhu, Ph.D.)

B.S. in Biology July 2008

Journal Publications

Sang, L., Dick, I.E., Yue, D.T. (2016) Protein kinase A modulation of Cav1.4 calcium channels. *Nat Commun,* In press.

Lee, S. R., **Sang, L.**, & Yue, D. T. (2016) Uncovering Aberrant Mutant PKA Function with Flow Cytometric FRET. *Cell Rep, 14*(12), 3019-3029.

Ben-Johny, M., Dick, I.E., **Sang, L.**, Limpitikul, W.B., Kang, P.W., Niu, J., Banerjee, R., Yang, W., Babich, J.S., Issa, J.B., Lee, S.R., Namkung, H., *et al.* (2015) Towards a Unified Theory of Calmodulin Regulation (Calmodulation) of Voltage-Gated Calcium and Sodium Channels. *Current molecular pharmacology*. 8, 188-205.

Dick, I.E., Limpitikul, W.B., Niu, J., Banerjee, R., Issa, J.B., Ben-Johny, M., Adams, P.J., Kang, P.W., Lee, S.R., **Sang, L.**, *et al*. (2015) A rendezvous with the queen of ion channels: Three decades of ion channel research by David T. Yue and his Calcium Signals Laboratory. *Channels.*1-13.

Bazzazi, H., **Sang, L.**, Dick, I.E., Joshi-Mukherjee, R., Yang, W., Yue, D.T. (2015) Novel FRET-based reporter reveals differential calcineurin activation in neonatal and adult cardiomyocytes. *J Physiol*. 593(17), 3865-84.

Sun, Z., **Sang, L.**, Ju, L., Zhu, H. (2008) A new method for splice site prediction based on the sequence patterns of splicing signals and regulatory elements. *Chinese Sci. Bull*., 53(21): 3331-3340.

Conference Presentations

Sang, L., Dick, I.E., Yue, D.T. (2015) Live cell biochemistry implicates Protein Kinase A modulation of L-type Cav1.4 channels (abstract). *Biophysical Journal* 108 (2), 366a-367a

Lee, S.R., **Sang, L.**, Yue, D.T. (2014) High throughput live-cell FRET binding assay by flow cytometry (abstract). *Biophysical Journal* 106 (2), 245a

Bazzazi, H., **Sang, L.**, Yue, D.T. (2013) FRET-Based Genetically Encoded Sensor of Calcineurin Activation (abstract). *Biophysical Journal* 104 (2), 530a

Sang, L., Bazzazi, H., Ben-Johny, M., Yue, D.T. (2012) Resolving the grip of the distal carboxy tail on the proximal calmodulatory region of Cav channels (abstract). *Biophysical Journa*l 102 (3), 126a

Honors and Awards

2007 China national petroleum scholarship

2006 Mechanics climbing scholarship

2006 Outstanding academic performance award

Experience and leadership

Android app developer and team leader (2015)

Member of Biophysical Society (2011-2015)

Teaching assistant & guest lecturer, *Ion Channels of Excitable Membranes* (2013)

Vice president, Graduate Student Association at Johns Hopkins (2011-2012)

Judger, Graduate Student Association Travel Award (2011-2012)

Board member, Hopkins Biotech Network (2011-2012)

CFA level 2 candidate (2011-present)

Organizer, Graduate Student Association Poster Session (2011)

BME representative, Graduate Student Association at Johns Hopkins (2010-2011)

Teaching assistant, *Systems Bioengineering I* (2010)

Organizer, Johns Hopkins SOM Chinese Student Journal Club (2008-2010)